Nuclear Charge Radius of the Halo Nucleus Lithium-11

Dissertation zur Erlangung des Grades
"Doktor
der Naturwissenschaften"

am Fachbereich Physik, Mathematik und Informatik
der Johannes Gutenberg-Universität
in Mainz

Rodolfo Marcelo Sánchez Alarcón
geboren in La Paz, Bolivien
Mainz, den 2006

Zusammenfassung

Kernladungsradien kurzlebiger Isotope können nur durch die Messung der Isotopieverschiebung kernmodellunabhängig bestimmt werden. Dazu wurde an der Gesellschaft für Schwerionenforschung (GSI), Darmstadt eine neuartige Technik entwickelt. Diese kombiniert Zweiphotonen-Spektroskopie des $2s\,^2S_{1/2} \rightarrow 3s\,^2S_{1/2}$-Übergangs mit Resonanz-Ionization und einem Nachweis durch Quadrupol-Massenspektrometrie. Auf diese Weise wird sowohl für eine Bestimmung der Kernladungsradien die notwendige Genauigkeit von 5×10^{-5} als auch eine Effizienz von 10^{-4} erreicht. Im Rahmen dieser Arbeit ist es mit der Methode gelungen am TRIUMF Institut (Vancouver) erstmals die Isotopieverschiebung des Isotops ^{11}Li zu messen. Darüberhinaus konnte die Genauigkeit für die anderen Lithiumisotope gegenüber früheren Messungen an der GSI um etwa einen Faktor vier verbessert werden. Die Resultate wurden mit den neuesten Berechnungen des Masseneffekts in Drei-Elektronen-Systemen kombiniert, um die mittleren quadratischen Ladungsradien aller Lithium-Isotope, insbesondere des Zwei-Neutronen-Halokerns ^{11}Li, zu bestimmen. Die erhaltenen Radien nehmen von ^{6}Li bis ^{9}Li kontinuierlich ab, während der Radius von ^{9}Li zu ^{11}Li stark ansteigt. Dies wird mit verschiedenen Kernmodellen verglichen, von denen ein Multicluster-Modell die beste Übereinstimmung zeigt. In diesem Modell wird der Anstieg des Kernladungsradius zwischen ^{9}Li und ^{11}Li hauptsächlich durch intrinsische Anregungen des ^{9}Li-Rumpfes verursacht, während die Korrelation der Halo Neutronen nur eine untergeordnete Rolle spielt.

Abstract

Nuclear charge radii of short-lived isotopes can be probed in a nuclear-model independent way via isotope shift measurements. For this purpose a novel technique was developed at GSI Darmstadt. It combines two-photon laser spectroscopy in the $2s\,^2S_{1/2} \rightarrow 3s\,^2S_{1/2}$ electronic transition of lithium, resonance ionization, and detection via quadrupole mass spectrometry. In this way an accuracy of 5×10^{-5} which is necessary for the extraction of nuclear charge radii, and an overall detection efficiency of 10^{-4} is reached. This allowed an isotope shift measurement of ^{11}Li for the first time at the TRIUMF facility in Vancouver. Additionally, uncertainties in the isotope shift for all other lithium isotopes were reduced by about a factor of four compared to previous measurements at GSI. Results were combined with recent theoretical mass shift calculations in three-electron systems and root-mean-square nuclear charge radii of all lithium isotopes, particulary of the two-neutron halo nucleus ^{11}Li, were determined. Obtained charge radii decrease continuously from ^{6}Li to ^{9}Li, while a strong increase between ^{9}Li and ^{11}Li is observed. This is compared to predictions of various nuclear models and it is found that a multicluster model gives the best overall agreement. Within this model, the increase in charge radius between ^{9}Li and ^{11}Li is to a large extend caused by intrinsic excitation of the ^{9}Li-like core while the neutron-halo correlation contributes only to a small extend.

Contents

List of Figures

List of Tables

1 Introduction

In 1966, the nucleus ^{11}Li was observed for the first time and its nuclear decay modes were studied [Pos66]. When first radioactive beam facilities were starting to operate in the 1980's, nuclear matter radii of light short-lived nuclei were investigated by means of nuclear interaction cross section measurements. Extracted matter radii for lithium isotopes from such measurements are shown in Fig. 1.1. It was surprising that the measured interaction cross sections for these isotopes colliding with ordinary nuclear targets displayed a very large increase for ^{11}Li [Tan85]. An interpretation of the structure of this nucleus was made shortly after in terms of a "neutron halo", which in this case is a "dineutron" weakly bound in an s state to the ^{9}Li-like core [Han87]. A fundamental concept in the halo picture is the tunneling into a classically forbidden range. The halo neutrons in ^{11}Li spend more than 50% of their time outside the range of the strong interaction. The large radius of ^{11}Li was explained by the weak binding energy between ^{9}Li and the two neutrons of only approximately 300 keV[1] compared to typical binding energies of 5 MeV/nucleon in stable nuclei [Aud03].

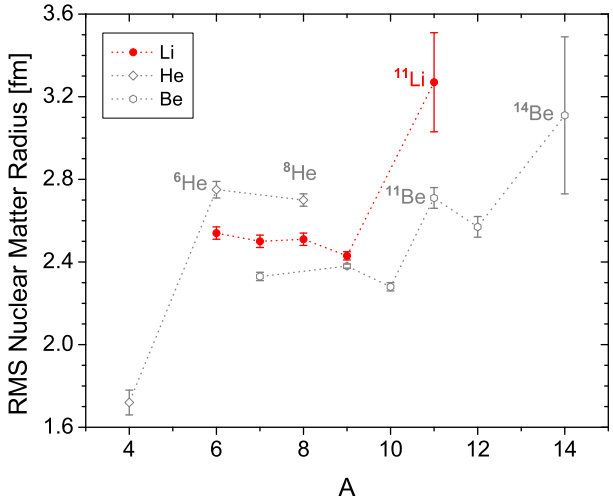

Figure 1.1. Root-mean-square (rms) nuclear matter radii of lithium, helium, and beryllium isotopes as obtained by Tanihata *et al.* [Tan85, Tan88]. ^{11}Li, ^{6,8}He, and ^{11,14}Be have a much larger radius than their other respective isotopes.

[1] A new value of 375 keV for the two-neutron separation energy of ^{11}Li has been measured recently [Bac05].

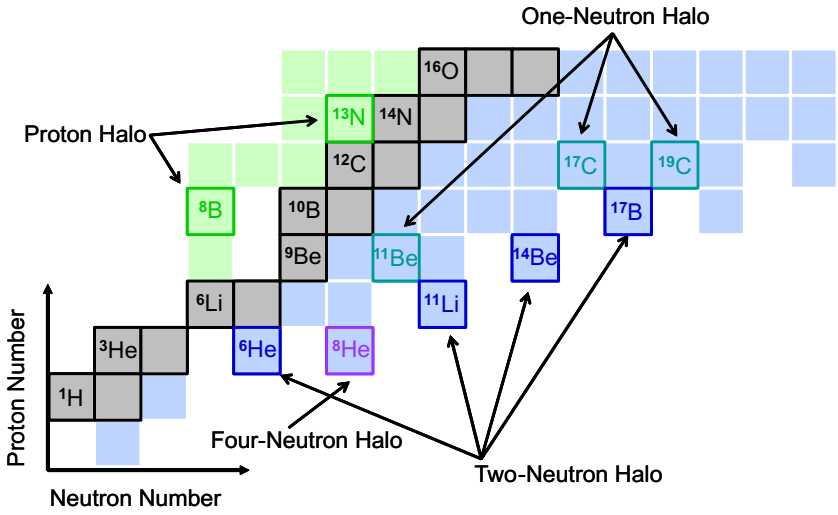

Figure 1.2. Neutron-halo nuclei. There are also evidences of proton-halo nuclei.

Similar large matter radii were found for ^{6,8}He [Tan85] and ^{11,14}Be [Tan88], as shown in Fig. 1.1. This discovery triggered a multitude of experimental investigations on these halo nuclei. Other light nuclei, which were also later found in such configurations, are indicated in Fig. 1.2.

So far ^{11}Li is the best studied halo nucleus. A narrow momentum distribution was measured for ^{9}Li fragments from breakup of ^{11}Li on a light target [Kob88]. The width, about an order of magnitude smaller than the Fermi momentum of 300 MeV/c found for ordinary fragmentation reactions, is consistent with the dineutron model, in which the large radius is reflected in a narrow relative momentum distribution, because of the uncertainty principle. In these measurements, a narrow momentum distribution is not observed for fragments other than ^{9}Li and the halo neutrons, *i.e.*, if more than two neutrons or even protons are removed. A fact that is strongly supporting the picture of a halo formed by only two neutrons.

It has been an important question from the very beginning, whether the ^{9}Li core is decoupled from the halo in the sense that it is not modified from the free ^{9}Li. Such a modification could be observed via a change in the nuclear charge distribution between ^{9}Li and ^{11}Li. However, nuclear reaction studies use strong interactions and thus no direct information concerning the charge distribution or proton distribution inside the nucleus is available. Blank *et al.* [Bla92] measured the charge-changing cross section of lithium isotopes. The derived cross sections do not change from ^{7}Li to ^{11}Li. This indicates that the proton distribution changes only slightly from ^{7}Li to ^{11}Li, but the results are nuclear-model dependent.

The electric quadrupole moment of a nucleus provides also information on the matter distribution. It is proportional to $\langle r^2 \rangle$ and thus has a sensitivity to the size of the charge

distribution as well as to the deformation. The quadrupole moments were determined for all lithium isotopes using collinear laser spectroscopy in combination with β-NMR [Arn94]. The results for ^{9}Li and ^{11}Li agreed within their uncertainties, giving no indication for a modified core.

Nuclear charge radii can be probed in a model-independent way via measurements of the optical isotope shift [Ott87]. In fact, this technique has been applied successfully in medium and high Z stable and unstable nuclei, but light nuclei represent a big challenge for this method. The reason is that the field shift, which provides information about the nuclear charge distribution, is ten-thousand times smaller than the mass shift, which is proportional to the relative change in nuclear mass between two isotopes. The lightest short-lived isotopes investigated until 2003 was the Ne chain [Gei02]. Indeed, this was also the first attempt to see an effect of a proton halo for ^{17}Ne but the experiment did not give a conclusive indication for such a halo.

To proceed to lighter elements, a new method had to be developed that combines atomic theory calculations and high-resolution isotope shift measurement.

Recently, accurate atomic calculations of the mass shift [Yan00, Dra05], reached an accuracy of one part in 10^5 for two- and three-electron systems. Thus, they provided the possibility to extract the field shift information as a difference between experimental isotope shifts and theoretical mass shift calculations with laser-spectroscopic accuracy.

To apply this approach was the goal of the Two-Photon Lithium Spectroscopy (ToPLiS) collaboration. Therefore, within the last years, a novel laser and mass spectroscopy technique was developed at GSI, Darmstadt, to measure the isotope shift in the $2s\,^2S_{1/2} \rightarrow 3s\,^2S_{1/2}$ two-photon transition of lithium [Sch00, Noe03]. First experiments were carried out successfully at the online mass separator at GSI in 2003 and the nuclear charge radii of the unstable isotopes ^{8}Li and ^{9}Li were measured [Ewa04, Ewa05].

Via a ^{4}He$-^{6}$He isotope shift measurement on the $2s\,^3S_1 \rightarrow 3p\,^3P_2$ transition, performed on individual He atoms confined and cooled in a magneto-optical trap, the nuclear charge radius of ^{6}He was determined at Argonne National Laboratory (ANL) in 2004 [Wan04].

The results of these experiments are able to clearly discriminate between different nuclear models [Dra05] and demonstrate the relevance of this approach and the challenge for the ToPLiS collaboration was now to measure the nuclear charge radius of ^{11}Li. To do so, the experimental apparatus was moved to TRIUMF, Vancouver BC, Canada, where the highest ^{11}Li radioactive beam intensities at a few ten keV kinetic energy are provided at the ISAC facility.

In this work, the measurement of the root-mean-square nuclear charge radius of ^{11}Li is described and the results are analyzed and compared with predictions of nuclear models.

The next chapter summarizes relevant properties of the lithium isotopes and briefly discusses some theoretical background on nuclear and atomic theory. The techniques that were used and combined to measure the isotope shift in lithium are described in Chapter 3 while Chapter 4 is dedicated to the experimental apparatus and the changes that had to be performed in order to adapt it to the beamline at ISAC. Chapter 5 presents the data and results. The conclusions are discussed in Chapter 6 and an outlook on further experiments is given.

2 Theory

2.1 Properties of Lithium Isotopes

Due to their favorable atomic structure as alkalis, the lithium isotopes attracted much interest already in the 1970's for high precision measurements of the hyperfine structure, to yield magnetic dipole and quadrupole moments. After the discovery of the neutron halo in the 1980's, the respective properties were also measured for ^{8,9,11}Li in an outstanding series of experiments at ISOLDE. A compilation of the results is given in Table 2.1. Concerning the halo structure of ^{11}Li, the most remarkable result is the small difference between ^{9}Li and ^{11}Li. The magnetic moments are close to the Schmidt value and are less than 10 % different, while the quadrupole moments agree within their uncertainties. This shows that a large deformation cannot be the reason for the large matter radius.

2.1.1 Two-Neutron Separation Energy and Mass of Lithium-11

Nuclear masses are essential for the understanding of nuclear structure as well as for accurate calculations of the isotope shift in the atomic spectra. Masses of the stable lithium isotopes and ^{8,9}Li are known with a precision on the order of a few keV, corresponding to a relative accuracy of 10^{-7}. This is sufficient for isotope shift calculations presented in Section 2.3. However, for ^{11}Li the mass was determined only from reaction Q values, but not by precise radio-frequency measurements, *e.g.*, in a Penning trap until recently. The

Table 2.1. Nuclear spin I, half-life $T_{1/2}$, nuclear mass M, nuclear magnetic moment μ_I, nuclear electric quadrupole moment Q, ground state hyperfine structure splitting HFS, root-mean-square nuclear mass-radius $\bar{r}_m$ and root-mean-square nuclear charge radius $\bar{r}_c$ $\left(\bar{r} = \langle r^2\rangle^{1/2}\right)$ of the lithium isotopes. $\bar{r}_c$ was measured by elastic electron scattering.

Isotope	I	$T_{1/2}$ [ms]	M[u]	$\mu_I[\mu_N]$	Q [e fm^2]	HFS [MHz]	$\bar{r}_m$[fm]	$\bar{r}_c$[fm]
^{6}Li	1	∞	6.01512280(2)	0.8220473(6)	-0.083(8)	228.2052590(30)$^{\diamond}$	2.45(7)†	2.55(4)
^{7}Li	3/2	∞	7.01600455(9)	3.2564625(4)	-4.06(8)	803.5040866(10)$^{\diamond}$	2.50(3)‡	2.39(3)
^{8}Li	2	838(6)	8.02248736(10)	1.65340(2)	3.27(6)	382.543(7)§	2.45(6)†	-
^{9}Li	3/2	178.3(4)	9.026790(2)	3.4391(6)	-2.74(1)	856(16)$^{\flat}$	2.43(7)†	-
^{11}Li	3/2	8.59(14)	11.043716(6)	3.668(3)	-3.1(5)	920(39)$^{\flat}$	3.62(19)†	-
References		[Aud97]	[Aud03]	[Sto05]	[Sto05]	$^{\diamond}$[Bec74], §[Neu73] $^{\flat}$[Arn87]	†[Ege02] ‡[Tan85]	[Jag74]

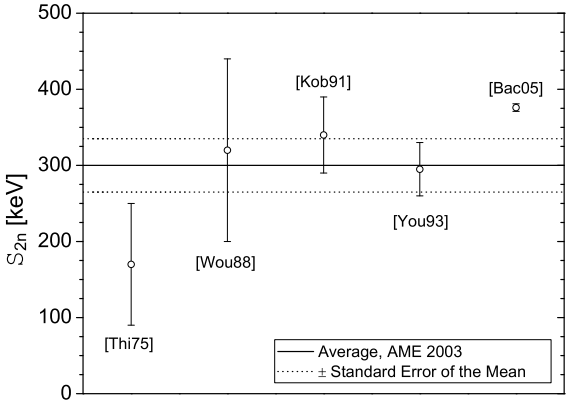

Figure 2.1. Different measurements of the ^{11}Li two-neutron separation energy.

mass of ^{11}Li, M_{11}, and the two-neutron separation energy, S_{2n}, are related via,

$$M_{11} = M_9 + 2m_n - \frac{S_{2n}}{931494.013 \text{ keV u}^{-1}} , \tag{2.1}$$

where, M_9 is the mass of ^{9}Li and m_n is the mass of the neutron. Figure 2.1 shows the two-neutron separation energy obtained from various measurements and the average value of 300 keV from the Atomic Mass Evaluation 2003 [Aud03]. This value has been recently remeasured by mass spectrometry and improved in precision with the MISTRAL experiment at CERN [Bac05]. The value obtained was S_{2n}=376(5) keV corresponding to a ^{11}Li nuclear mass of M_{11} = 11.043716(76) u, which is included in Fig. 2.1 and is considerably larger than the previously accepted value. Another independent high-accuracy measurement of this property is therefore highly desirable.

2.1.2 Decay Modes

The chain of lithium isotopes consists of the natural isotopes ^{6,7}Li and the radioactive isotopes ^{8,9,11}Li. The short-lived ones are usually produced on-line by an ISOL technique as described in Section 3.1. Their decay modes are important concerning the detection procedure for the different isotopes and are shown schematically in Table 2.2. ^{8}Li has a half-life of 838 ms and decays via β^- emission, followed by the disintegration of ^{8}Be into two α particles. The 178 ms isotope ^{9}Li has two β^- decay modes, one produces an excited state ^{9}Be*, which then decays into two α particles and a neutron, while the other mode leads directly to the ground state of the stable isotope ^{9}Be. The decay of ^{11}Li , which has a half-life of 8.3 ms, is more diverse. β^- emission ends in different states of ^{11}Be. Excited states lead to direct particle emission while the ground state populated in about 8 % of all ^{11}Li decays, has a β^- lifetime of $\sim$13.6 s.

Table 2.2. Simplified representation of the decay chains for the radioactive lithium isotopes.

Isotope	Radioactive Decay			Probability of the decay [%]
^{8}Li	$\longrightarrow$ $^{8}\mathrm{Be} + \beta^-$	$\longrightarrow$	$\alpha + \alpha$	100
^{9}Li	$\longrightarrow$ $^{9}\mathrm{Be}^* + \beta^-$	$\longrightarrow$	$\alpha + \alpha + \mathrm{n}$	49.5
	$^{9}\mathrm{Be} + \beta^-$			50.5
^{11}Li	$\longrightarrow$ $^{11}\mathrm{Be} + \beta^-$	$\longrightarrow$	$^{10}\mathrm{Be} + \mathrm{n}$	85
			$^{11}\mathrm{B} + \beta^-$	8
			$^{9}\mathrm{Be} + \mathrm{n} + \mathrm{n}$	4
			$\alpha + \alpha + \mathrm{n} + \mathrm{n} + \mathrm{n}$	2
			$^{6}\mathrm{He} + \alpha + \mathrm{n}$	1

2.2 Nuclear Physics

2.2.1 Nuclear Models of Lithium Isotopes

A theoretical description of the fascinating halo phenomenon is not easy to accomplish. The problem is that detailed treatment of the halo structure requires substantial consideration of the various correlations among the core and the halo nucleons as well as the possibility of intrinsic core excitations. A general problem for theoretical models of halo nuclei is the non-uniform density, the long-range behavior of the halo, and the correlations between the halo nucleons and the core. The diffuseness and long-range tail cannot be easily described in a harmonic-oscillator shell-model approach because the wave functions fall off rather quickly at the nuclear surface. Early models therefore described ^{11}Li as a three-body system of a ^{9}Li core and two additional neutrons. This picture is certainly over-simplified and is not conclusive concerning structural details of the nucleus because the interaction between the ^{9}Li core and the neutrons is not sufficiently well known and therefore phenomenological potentials must be used. In reality three-body interactions may play an important role and polarization of the ^{9}Li core will probably occur to some extend. Even in the $(\alpha+2\mathrm{n})$-system, ^{6}He, theory predicts that the structure of the α-core is slightly changed by the halo neutrons [Pie01] and the nuclear charge radius increases by about 4 %. Therefore, a much stronger modification may occur in the case of the "softer" ^{9}Li core.

A nuclear model based on the theory of quantum chromodynamics (QCD), the theory of quarks as fundamental particles of the baryons and their interactions, would be the *grale* of nuclear physics. However, performing QCD calculations in the non-perturbative regime at low and medium energies is still much too complicated and effective theories using

meson-nucleon degrees of freedom are used instead. Here, the forces between nucleons are mediated through the exchange of virtual mesons of which the lightest are the pions with mass $m_\pi \approx 140$ MeV. From the Heisenberg uncertainty principle

$$\Delta t \; \Delta E \geq \hbar, \tag{2.2}$$

where t is the time and E the energy, the range of the nuclear force can thus be estimated to be

$$r \approx c \; \Delta t \approx \frac{\hbar c}{m_\pi c^2} = \frac{197 \text{ MeV fm}}{140 \text{ MeV}} = 1.4 \text{ fm} \; . \tag{2.3}$$

The potential between two nucleons based on the exchange of mesons was already proposed by Hideki Yukawa in 1935:

$$V(r) = g \frac{e^{-mrc/\hbar}}{r} \tag{2.4}$$

with a coupling constant g, mass of the meson m and the distance between the nucleons r. A more detailed description of the one-pion exchange potential (OPEP) must also include spin and isospin effects[1]:

$$V_{\text{OPEP}} = \frac{f^2}{4\pi} \frac{m_\pi}{3} (\tau_1 \; \tau_2) \Bigg\{ \sigma_1 \sigma_2 + [3(\boldsymbol{\sigma}_1 \cdot \hat{e}_r)(\boldsymbol{\sigma}_2 \cdot \hat{e}_r) - \boldsymbol{\sigma}_1 \cdot \boldsymbol{\sigma}_2] \left[1 + \frac{3}{m_\pi r} + \frac{3}{(m_\pi r)^2} \right] \Bigg\} \frac{e^{-m_\pi r}}{m_\pi r} \; , \tag{2.5}$$

where f^2 is the coupling constant. This potential includes spin (σ) and isospin (τ) dependent contributions, which leads to a non-central spin-dependent tensor force and the breaking of chiral symmetry. Additionally, a repulsive force caused by the Pauli exclusion principle at short distances, exchange of heavier mesons and additional contributions produced by the higher order effects like two-body exchange at intermediate distances, must be considered. Parameters of these potentials are usually determined by fitting them to the world-data of nucleon-nucleon scattering.

Various two-nucleon (NN) potentials have been developed during the last decades *e.g.*, the Argonne v_{18} (AV18) potential [Wir95], the CD-Bonn [Mac96], and the Nijmegen [Sto94] potentials. A detailed discussion can be found in Carlson and Schiavilla [Car98].

Calculation of light nuclei with these NN potentials leads to the observation that most nuclei are underbound. This can be explained by the fact that nucleons are composite systems and not point-like particles. Mutual interaction leads to polarization

[1] Vectors are indicated by bold symbols.

effects that can be treated by including first excited states of the nucleons as shown in Fig. 2.2: a pion, exchange between two nucleons, is scattered by a third nucleon via the p-wave Δ resonance (with mass, $m_\Delta = 1232$ MeV/c^2, and spin $I = 3/2$). This attractive interaction provides more binding energy in nuclei. Parameters of these three-nucleon (NNN) potentials are usually constrained by the ground-state energies of the lightest nuclei. Here, a cancellation between the positive kinetic energy and the negative nucleon-nucleon potential results in a relatively strong contribution of the three-nucleon forces to the nuclear binding energies.

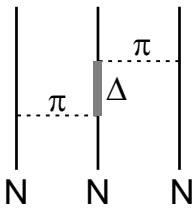

Figure 2.2. Nucleon polarization effect in two-pion exchange.

As in the two-nucleon case, a variety of theoretical NNN potentials exists, including the Urbana [Pud95], Illinois [Pie01] and Tucson-Melbourne [Coo01] potentials. Particulary the neutron-rich nuclei are of great importance for fitting their parameters because first calculations showed the importance of isospin-dependent forces [Pie01].

Once these potentials are created, they can be used to calculate wave function and eigenenergies of the nuclei numerically. Several approaches for such calculations exist and some of them, which predicted charge radii for the unstable lithium isotopes, will be briefly discussed. The charge radii measurements presented in this thesis provide an important test of these models.

2.2.2 Greens-Function Monte-Carlo Model

The Greens-Function Monte-Carlo (GFMC) method is the front-runner of the nuclear models described here, since it depends solely on two-nucleon and three-nucleon potentials. Even though the complexity of the calculations increase exponentially with the mass number A, most nuclei with $A \leq 12$ were calculated successfully. The first step to model a nucleus is a variational Monte-Carlo calculation to obtain an approximate solution of the many-body Schrödinger equation. The basis of the variational approximation is the fact that the real ground-state wave function of a Hamiltonian has the lowest energy E_0 of all possible wavefunctions and thus a normalized trial function ψ_V has an energy

$$E_V = \frac{\langle \psi_V | H | \psi_V \rangle}{\langle \psi_V | \psi_V \rangle} \geq E_0 \ . \tag{2.6}$$

Variation of the expansion coefficient c_k of a trial function $\psi_V = \sum_k c_k |k\rangle$ of states $|k\rangle$ with specific spin and isospin to minimize the expectation value of the Hamiltonian from the nuclear model, leads to the approximate solution. This is then used as the starting point

Table 2.3. Point-proton (p) and neutron (n) root-mean-square radii for the lithium isotopes calculated with the GFMC method [Pie01, Pie02].

Nucleus	$\bar{r}_{\mathrm{p}}$[fm]	$\bar{r}_{\mathrm{n}}$[fm]
^{6}Li	2.39	2.39
^{7}Li	2.25	2.44
^{8}Li	2.09	2.45
^{9}Li	2.04	2.57

for the Greens-Function Monte-Carlo calculations, which are based on the propagation of the wave function under the Hamiltonian, that means

$$\psi_0 = \lim_{n \cdot \Delta T \to \infty} \left[e^{-(H-E_0)\Delta T} \right]^n \psi_V \ , \tag{2.7}$$

where ΔT is a small timestep and n is the total number of integrated steps. In the limit $n \cdot \Delta T \to \infty$, ψ_0 is the ground state wavefunction with exact eigenenergy E_0.

This method has been used to calculate the ground states of ^{6,7,8,9}Li [Pie01, Pie02] and predicted charge radii for the combination of the AV18 NN potential and the IL2 NNN potential are summarized in Table 2.3. The GFMC, as well as most other theories treat the proton and neutrons as point-like particles. The calculated so-called point-proton and point-neutron radii are therefore denote r_{p} and r_{n} respectively. For comparison with measured charge radii r_{c}, the proton and neutron root-mean-square charge radii have to be included (see Section 5.8).

Unfortunately, the halo nucleus ^{11}Li could not be treated so far. Due to the weak two-neutron binding energy of only 375 keV [Bac05] the calculated trial function in the variational Monte Carlo calculation approach usually "falls apart" during the propagation procedure [Pie05].

2.2.3 Stochastic Variational Multi-Cluster Model

The Stochastic Variational Multi-Cluster (SVMC) model is a compromise between the simple three-body models and the more rigorous treatment in the Greens-function Monte-Carlo approach, in the sense that the ^{11}Li system is divided into subsystems, so called clusters, whose intrinsic structure is approximated by harmonic-oscillator (HO) wave functions, while the individual nucleons inside the clusters are taken into account for the nucleon-nucleon interaction. The lithium nuclei, for example, are divided in the cluster configurations listed in Table 2.4 [Suz02].

Table 2.4. Cluster decomposition of the lithium nuclei into ^{4}He (α), ^{3}H (t), and single-nucleons in the SVMC model [Suz02].

Nucleus	Cluster model	Most relevant channels
^{6}Li	$\alpha + \mathrm{p} + \mathrm{n}$	$\alpha + \mathrm{d}$, $^5\mathrm{He} + \mathrm{p}$, $^5\mathrm{Li} + \mathrm{n}$
^{7}Li	$\alpha + \mathrm{t}$	$\alpha + \mathrm{t}$
^{8}Li	$\alpha + \mathrm{t} + \mathrm{n}$	$^7\mathrm{Li} + \mathrm{n}$, $^5\mathrm{Li} + \mathrm{t}$
^{9}Li	$\alpha + \mathrm{t} + \mathrm{n} + \mathrm{n}$	$^7\mathrm{Li} + \mathrm{n} + \mathrm{n}$, $^5\mathrm{He} + {}^4\mathrm{H}$, $^8\mathrm{Li} + \mathrm{n}$
^{11}Li	$\alpha + \mathrm{t} + \mathrm{n} + \mathrm{n} + \mathrm{n} + \mathrm{n}$	$^9\mathrm{Li} + \mathrm{n} + \mathrm{n}$, $^{10}\mathrm{Li} + \mathrm{n}$

The wave function of an n-cluster system is constructed using correlated Gaussians and the stochastic variational approach is used to solve the Schödinger equation of the system under consideration. The wave function of ^{11}Li is constructed by adding two neutrons to ^{9}Li. The total wavefunction of ^{9}Li in the stochastic variational multi-cluster approach is a linear combination of different arrangements μ, each associated with a particular set of Jacobi coordinates $\boldsymbol{\varrho}_1^\mu, \ \ldots, \ \boldsymbol{\varrho}_{n-1}^\mu$. An example of the possible arrangements of the two halo neutrons in ^{11}Li relative to the ^{9}Li core is shown in Fig. 2.3(a,b). It should be noted that the model treats the ^{9}Li core still as a clustered object of $\alpha + \mathrm{t} + \mathrm{n} + \mathrm{n}$, as shown in Table 2.4, and all possible arrangements and relative angular momenta l_1, l_2, l_3 are considered. Two examples of such arrangements are shown in Fig. 2.3(c,d). The spin of the clusters couple to the total spin S and the orbital momenta l_i^μ belonging to the Jacobi coordinates ϱ_i^μ are coupled to the total angular moment L,

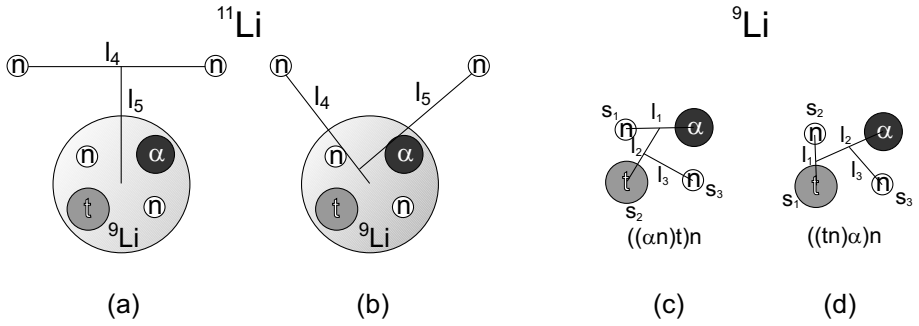

Figure 2.3. (a) T- and (b) Y-type arrangements of $^{11}\mathrm{Li} \equiv {}^9\mathrm{Li} + \mathrm{n} + \mathrm{n}$, with the relative angular momenta l_4 and l_5. (c,d) Description of ^{9}Li as $\alpha + \mathrm{t} + \mathrm{n} + \mathrm{n}$ including two examples of all arrangements and relative angular momenta l_1, l_2, l_3. The spin of the clusters is $\mathsf{s}_\mathsf{i} = 1/2$; the spin of the alpha particle is zero and it is omitted.

$$\Psi = \sum_{\mu} \sum_{(s_1,\ ...,\ s_n)S} \sum_{(l_1,\ ...,\ l_{n-1})L} \Psi^{\mu}_{[(s_1,\ ...,\ s_n)S,\ (l_1,\ ...,\ l_{n-1})L]JM} \ , \tag{2.8}$$

where for each arrangement μ, Ψ^{μ} is a product of the wavefunction of the intrinsic cluster motion $\Phi_{(s_1,\ ...,\ s_n)S}$ and the intercluster motion $\Gamma^{\mu}_{K(l_1,\ ...,\ l_{n-1})L}(\boldsymbol{\varrho}^{\mu}_1,\ \ \ldots,\ \ \boldsymbol{\varrho}^{\mu}_{n-1})$

$$\begin{aligned}\Psi^{\mu}_{[(s_1,\ ...,\ s_n)S,\ (l_1,\ ...,\ l_{n-1})L]JM} &= \sum_{K} C^{\mu}_{K,\ (s_1,\ ...,\ s_n)S,\ (l_1,\ ...,\ l_{n-1})L} \\ &\mathcal{A}\left\{\left[\Phi_{(s_1,\ ...,\ s_n)S}\Gamma^{\mu}_{K(l_1,\ ...,\ l_{n-1})L}(\boldsymbol{\varrho}^{\mu}_1,\ \ \ldots,\ \boldsymbol{\varrho}^{\mu}_{n-1})\right]_{JM}\right\} \ ,\end{aligned} \tag{2.9}$$

where K stands for the set of the indices $\{k_1,\ \ \ldots,\ k_{n-1}\}$, $\mathcal{A}$ is the intercluster antisymmetrizer to obey the Pauli principle, $\Phi_{(s_1,\ ...,\ s_n)S}$ is a vector coupled product of Slater determinants of harmonic oscillator wavefuntions with the size parameter $\beta = m\omega/\hbar$, and the intercluster motion is approximated by a combination of Gaussians with size parameter $\nu^{\mu}_{k_i}$

$$\Gamma^{\mu}_{k_i} \sim e^{-\nu^{\mu}_{k_i}(\varrho^{\mu}_i)^2}\mathcal{Y}_{l_i m_i}(\hat{\boldsymbol{\varrho}}^{\mu}_i) \ ; \qquad \mathcal{Y}_{l_i,m_i}(\mathbf{x}) = x^{l_i}Y_{l_i,m_i}(\hat{\mathbf{x}}) \ . \tag{2.10}$$

The size parameter β is adjusted to get the correct values for the sum of the radii of the free $(\alpha + \mathrm{t})$ and $(\alpha + {}^3\mathrm{He})$ clusters, and by energy minimization of these states. The ν_{k_i} are the free parameters of the model in order to minimize the ground state energy of the respective nucleus in a stochastic variational calculation.

This approach is quite powerful since it treats the different possible correlations explicitly. The partial waves in a given cluster arrangement form a complete set of states and therefore the different Jacobi coordinate systems are equivalent. However, a particular arrangement can only be represented by an infinite sum in terms of another arrangement.

It was discovered that for a description of the motion of the system at short distances it is sufficient to choose a few states in any of these arrangements, emphasizing particular types of correlation, to provide a major part of the binding energy.

Finally, it should be mentioned that the Stochastic Variational Multi-Cluster approach in Varga *et al.* uses an effective NN interaction of the Minnesota type, which consists of a central part, Coulomb interaction, and a spin-orbit force. The strength parameter of the central part was fixed to get the energies of the ^{7}Be, ^{8}B and ^{7,8}Li states right, while the spin orbit force was adapted to give the correct spacing between the $3/2^-$ and $1/2^-$ states of ^{7}Li and ^{7}Be. After fixing these parameters, there were no further free parameters in the interaction used.

All lithium isotopes were described in a coherent manner and the results for the charge radii are summarized in Table 2.5. Here, two rows of values for ^{11}Li are given, one cor-

Table 2.5. Properties of the lithium nuclei for the $\alpha + t + n + \cdots + n$ multicluster model. Point-proton (p), neutron (n), and mass (m) root-mean-square radii $\bar{r}$. Q is the nuclear electric quadrupole moment, and μ_I the nuclear magnetic moment. S_{2n} is the binding energy of the last two neutrons for this cluster model. The row ^{11}Li* is obtained assuming a "frozen" ^{9}Li core [Suz02].

Nucleus	$\bar{r}_p$[fm]	$\bar{r}_n$[fm]	$\bar{r}_m$[fm]	Q[e fm^2]	$\mu_I[\mu_N]$	S_{2n}[MeV]
^{7}Li	2.27	2.38	2.33	-3.65	3.15	
^{8}Li	2.18	2.58	2.44	2.23	1.17	
^{9}Li	2.12	2.54	2.41	-3.37	3.40	
^{11}Li*	2.26	3.21	3.15	-3.52	3.21	-0.12
^{11}Li	2.43	3.09	3.03	-3.71	3.23	-0.34

responds to the full calculation while the other on (^{11}Li*) gives results from calculations where the ^{9}Li core was frozen to its ground state. It is obvious that this frozen approximation misses a considerable amount of binding energy, typically 100-200 keV, which is quite significant for halo nuclei. Additionally, including intrinsic excitations leads to a considerably larger charge radius while the matter radius actually shrinks. The reduced neutron radius in the full calculation is probably caused by the additional 220 keV binding energy. The core polarization[2] gives also rise to an increased quadrupole moment. The difference between ^{11}Li and ^{9}Li is on the order of 10 % instead of only 5% when the core is frozen, whereas the influence onto the magnetic moment is marginally. The model predicts a decrease in the magnetic moment between ^{9}Li and ^{11}Li while experimentally an increase is observed.

2.2.4 Large-Basis No-Core Shell-Model

In the framework of the *ab-initio* Large-Basis No-Core Shell Model (LBNCSM) calculations, the light nuclei are considered as systems of A nucleons (usually up to $A = 16$) interacting by realistic internucleon forces [Nav98]. The calculations are performed using a large but finite harmonic-oscillator basis. Due to the basis truncation, it is necessary to derive an effective interaction from the underlying internucleon interaction that is appropriate for the basis employed. The technique is based on a separation between the model space and the excluded space at the two-body level. For the p-shell nuclei, like $^{7-11}$Li, the calculations are performed using two-body effective interactions derived from a microscopical nucleon-nucleon potential which includes isospin breaking. The calculations

[2]Intrinsic excitation, core polarization, and core distortion are synonymous.

Table 2.6. Calculated point-proton root-mean-square radii ($\bar{r}_p$), quadrupole moments (Q) and magnetic moments (μ_I) for the the lithium nuclei in the No-Core Shell Model. The results correspond to the $6\hbar\Omega$ for ^{7}Li and 4 $\hbar\Omega$ for $^{8-11}$Li. The harmonic-oscillator parameter was taken to be $\hbar\Omega = 17$ MeV for $^{7-8}$Li, 16 MeV for ^{9}Li and 15 MeV for ^{11}Li respectively [Nav98].

Nucleus	$\bar{r}_p$[fm]	Q[e fm^2]	$\mu_I[\mu_N]$
^{7}Li	2.045	-2.710	2.994
^{8}Li	1.941	2.208	1.419
^{9}Li	1.946	-2.085	2.940
^{11}Li	1.986	-2.301	3.601

are performed as a function of the harmonic-oscillator frequency Ω. For ^{7}Li and $^{8-11}$Li up to 6 $\hbar\Omega$ and 4 $\hbar\Omega$ excitations relative to the unperturbed ground state were allowed, respectively. Table 2.6 resumes the calculated properties for the lithium nuclei.

Point-proton radii in the LBNCSM are considerable smaller that in the GFMC or SVMC approaches. The electromagnetic moments show much less agreement with the experiment (Table 2.1), especially remarkable is the large difference in the magnetic moment between ^{9}Li and ^{11}Li.

2.2.5 Dynamic Correlation Model

The dynamic correlation model (DCM) is a scheme that, starting from shell model states, introduces neutron-core interaction via a two-body potential. This leads to an admixture of virtually excited single-particle states from the core. The advantage of this model is to provide larger configuration spaces than used in the shell model calculation, to include exactly the Pauli principle in the coupled spaces, and to generate correlated solutions for the n paired systems. The phenomenological particle-particle and particle-hole interactions, which correlate the nucleons and lead to an excitation of the nuclear core, are treated by a G-matrix and phenomenological matrix elements respectively.

Calculated root-mean square nuclear charge, matter radii and magnetic moments of ^{6,7,9,11}Li are given in Table 2.7. The magnetic moments ^{6,7,9}Li are all slightly larger than the experimental values by $0.003 - 0.004$ μ_N.

Table 2.7. Calculated point-nucleon root-mean-square charge and matter radii, and magnetic moments of lithium isotopes in the Dynamic Correlation Model [Tom02].

Nucleus	$\bar{r}_{\rm c}$[fm]	$\bar{r}_{\rm m}$[fm]	$\mu_I[\mu_{\rm N}]$
^{6}Li	2.55	2.41	0.8260
^{7}Li	2.41	2.36	3.2534
^{9}Li	2.42	2.42	3.4427
^{11}Li	2.67	3.64	-

2.3 Atomic Physics

2.3.1 Isotope Shift

Root-mean-square nuclear charge radii of short-lived isotopes can only be extracted in a nuclear-model independent way from isotope shift measurements. The isotope shift of an electronic transition ($\delta\nu^{A,A'}$), that is the shift in frequency of a spectral resonance between two isotopes ($\nu^{A} - \nu^{A'}$), can be expressed as the sum of two contributions, the mass shift ($\delta\nu^{A,A'}_{\rm MS}$) and the field shift ($\delta\nu^{A,A'}_{\rm FS}$) [Ott87],

$$\delta\nu^{A,A'} = \nu^{A} - \nu^{A'} = \delta\nu^{A,A'}_{\rm MS} + \delta\nu^{A,A'}_{\rm FS} \ . \tag{2.11}$$

The mass shift is usually divided into two terms, the normal mass shift (NMS) $\delta\nu^{A,A'}_{\rm NMS}$, which is given by a simple replacement of the electron mass with the reduced mass of the system, and the specific mass shift (SMS) $\delta\nu^{A,A'}_{\rm SMS}$, which reflects the influence of the electron correlations onto the nuclear motion:

$$\delta\nu^{A,A'}_{\rm MS} = \delta\nu^{A,A'}_{\rm NMS} + \delta\nu^{A,A'}_{\rm SMS} \ . \tag{2.12}$$

Both contributions have the same nuclear mass dependence which, to a good approximation, is given by

$$\delta\nu^{A,A'}_{\rm MS} = (K_{\rm NMS} + K_{\rm SMS})\frac{M_A - M_{A'}}{M_A M_{A'}} \ , \tag{2.13}$$

where $K_{\rm NMS}$ and $K_{\rm SMS}$ indicate the so-called normal mass shift and specific mass shift coefficients respectively.

The field shift in the atomic energy levels is produced by the change in the charge density distribution of the nucleus which is caused by the change in the neutron number. In the non-relativistic approximation the field shift can be written as a function of the difference in the mean-square nuclear charge radii of the isotopes under consideration,

$$\delta\nu^{A,A'}_{\rm FS} = -\frac{2\pi}{3} Z e^2 \Delta|\Psi(0)|^2 \left(\left\langle {r_{\rm c}}^2 \right\rangle_A - \left\langle {r_{\rm c}}^2 \right\rangle_{A'}\right) = F\ \delta\left\langle {r_{\rm c}}^2 \right\rangle^{A,A'} \ . \tag{2.14}$$

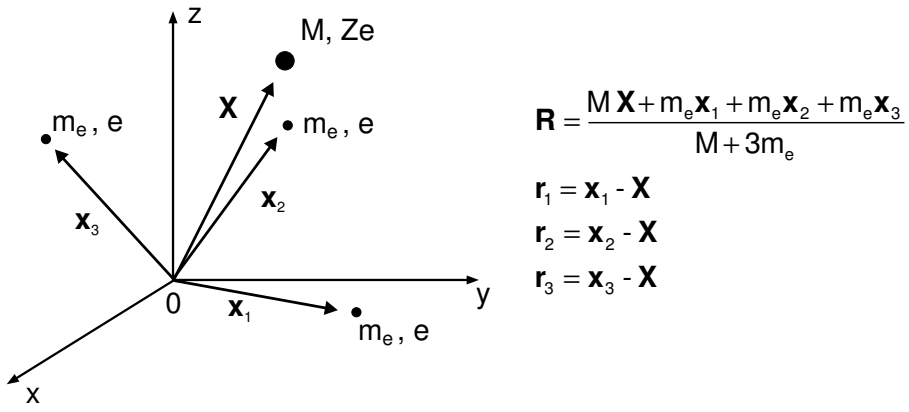

Figure 2.4. Definition of coordinates for a three-electron atom. After making the center of mass transformation, **R** can be regarded as an ignorable coordinate.

$F = -(2\pi/3)Ze^2\Delta|\Psi(0)|^2$ is known as the electronic field shift coefficient, with Ze being the charge of the atomic nucleus, and $\Delta|\Psi(0)|^2$ the change in the electron charge density at the nucleus between the lower and upper state of an optical transition.

To resume, the total isotope shift can be expressed by

$$\delta\nu^{A,A'} = \delta\nu_{\mathrm{MS}}^{A,A'} + F\,\delta\langle r_{\mathrm{c}}{}^2\rangle^{A,A'} \ . \tag{2.15}$$

For light elements, like helium or lithium, the field shift contribution is about ten thousand times smaller than the mass shift. Thus, to extract nuclear charge radius information from isotope shift measurements, a precise calculation of the mass shift is required where it is indispensable to include the electron correlations. Much progress has been achieved in this field recently. However, the three-electron system is still at the forefront of todays possibilities. Gordon Drake and Zong-Chao Yan have performed such calculations and a short summary will be given in the next section.

2.3.2 Atomic Theory for a Three-Electron Atom

The nonrelativistic Schrödinger equation for an atomic system consisting of three electrons orbiting around an atomic nucleus of charge Ze and mass M [Dra05], as depicted in Fig. 2.4, can be expressed, after rescaling distances according to $\boldsymbol{\rho}_i = \mathbf{r}_i(\mu e^2/\hbar^2)$, as

$$\left(-\frac{1}{2}\sum_{i=1}^{3}\nabla_{\rho_i}^2 - Z\sum_{i=1}^{3}\frac{1}{\rho_i} + \sum_{i>j}^{3}\frac{1}{|\boldsymbol{\rho}_i - \boldsymbol{\rho}_j|} - \frac{\mu}{M}\sum_{i>j}^{3}\boldsymbol{\nabla}_{\rho_i}\cdot\boldsymbol{\nabla}_{\rho_j}\right)\Psi = \mathcal{E}\Psi \ , \tag{2.16}$$

where $\mu = m_e M/(m_e + M)$ is the reduced mass of the electron, and

$$\mathcal{E} = \left(\frac{m_e}{\mu}\right)\frac{E_{\mathrm{NR}}\hbar^2}{e^4} = \frac{E_{\mathrm{NR}}}{2R_\infty(1-\frac{\mu}{M})} \ , \tag{2.17}$$

the rescaled nonrelativistic (NR) energy of the system with R_∞ being the Rydberg constant for an infinite heavy nucleus. The equation (2.16) can be expressed as

$$\left[H_0 + \left(-\frac{\mu}{M}\right) H_1\right] \Psi = \mathcal{E}\Psi, \tag{2.18}$$

where $H_1 = \sum_{i>j}^{3} \boldsymbol{\nabla}_{\rho_i} \cdot \boldsymbol{\nabla}_{\rho_j}$ and H_0 is the Hamiltonian for an infinite heavy nucleus. Eq. (2.18) can be solved perturbatively by expanding Ψ and $\mathcal{E}$ according to

$$\Psi = \Psi_0 - \frac{\mu}{M}\Psi_1 + \cdots \ , \tag{2.19}$$

$$\mathcal{E} = \mathcal{E}^{(0)} - \frac{\mu}{M}\mathcal{E}^{(1)} + \left(\frac{\mu}{M}\right)^2 \mathcal{E}^{(2)} - \cdots \ . \tag{2.20}$$

Substituting these two expansions into (2.18), one can obtain the following equations

$$\begin{aligned} H_0\Psi_0 &= \mathcal{E}^{(0)}\Psi_0, & (2.21)\\ (H_0 - \mathcal{E}^{(0)})\Psi_1 &= (\mathcal{E}^{(1)} - H_1)\Psi_0, & (2.22)\\ &\vdots \end{aligned}$$

with $\mathcal{E}^{(1)} = \langle\Psi_0|H_1|\Psi_0\rangle$. Both Ψ_0 and Ψ_1 are solved variationally in multiple basis sets in Hylleraas coordinates. According to (2.17), $E_{\rm NR}$ can finally be expressed as

$$E_{\rm NR} = 2R_\infty \left[\mathcal{E}^{(0)} - \frac{\mu}{M}(\mathcal{E}^{(0)} + \mathcal{E}^{(1)}) + \left(\frac{\mu}{M}\right)^2 (\mathcal{E}^{(1)} + \mathcal{E}^{(2)}) + \cdots \right] \ , \tag{2.23}$$

or,

$$E_{\rm NR} = E_{\rm NR}^{(0)} + \frac{\mu}{M}E_{\rm NR}^{(1)} + \left(\frac{\mu}{M}\right)^2 E_{\rm NR}^{(2)} + \cdots \ . \tag{2.24}$$

The next step is to include relativistic and quantum electrodynamic (QED) corrections by perturbation theory. In terms of the fine structure constant $\alpha = e^2/\hbar c$, the total energy is then given by an expression of the form

$$E_{\rm tot} = E_{\rm NR} + \alpha^2 E_{\rm rel} + \alpha^3 E_{\rm QED} + \cdots + \Delta E_{\rm nuc} \ , \tag{2.25}$$

where $\alpha^2 E_{\rm rel}$ is the leading relativistic correction, $\alpha^3 E_{\rm QED}$ is the leading quantum electrodynamic (QED) correction, and $\Delta E_{\rm nuc}$ is the shift in the energy produced by the finite nuclear volume. The dependence of these quantities on the ratio μ/M is as follows

$$\begin{aligned} E_{\rm rel} &= E_{\rm rel}^{(0)} + \frac{\mu}{M}E_{\rm rel}^{(1)} + \cdots \ , & (2.26)\\ E_{\rm QED} &= E_{\rm QED}^{(0)} + \frac{\mu}{M}E_{\rm QED}^{(1)} + \cdots \ , & (2.27) \end{aligned}$$

and in lowest order $\Delta E_{\rm nuc}$ is given by

$$\Delta E_{\rm nuc} = \frac{2\pi Z e^2 \left\langle {r_{\rm c}}^2 \right\rangle}{3} \left\langle \sum_{i=1}^{3} \delta(\mathbf{r}_i) \right\rangle \ , \tag{2.28}$$

Table 2.8. Mass shift contribution $\delta\nu_{MS}^{11,7}$ for the $2s\,^2S_{1/2} \rightarrow 3s\,^2S_{1/2}$ electronic transition in lithium.

Contribution, (order)	Mass Shift [MHz]
Nonrelativistic, μ/M	25 104.483(20)
Nonrelativistic, $(\mu/M)^2$	-2.968(0)
Relativistic, $\alpha^2\mu/M$	0.417(121)
QED, $\alpha^3\mu/M$	-0.120(6)
Total	25 101.812(123)

where $\left\langle \sum_{i=1}^{3} \delta(\mathbf{r}_i) \right\rangle$ denotes the expectation value of the electron density at the nucleus.

The energy difference between two isotopes A and A' can be written in the form

$$\begin{aligned} \Delta E^{A,A'} &= \left[\left(\tfrac{\mu}{M}\right)_A - \left(\tfrac{\mu}{M}\right)_{A'}\right]\left(E_{\mathrm{NR}}^{(1)} + \alpha^2 E_{\mathrm{rel}}^{(1)} + \alpha^3 E_{\mathrm{QED}}^{(1)}\right) \\ &\quad + \left[\left(\tfrac{\mu}{M}\right)_A^{\,2} - \left(\tfrac{\mu}{M}\right)_{A'}^{\,2}\right] E_{\mathrm{NR}}^{(2)} + \ldots + \Delta E_{\mathrm{nuc}}^{A} - \Delta E_{\mathrm{nuc}}^{A'} \,, \end{aligned} \tag{2.29}$$

where terms of higher order in α and μ/M can be neglected at present levels of experimental accuracy. It is clear that equation (2.29) is equivalent to equation (2.15) and the field shift $\boldsymbol{F}\,\delta\langle r_c{}^2\rangle^{A,A'} = \Delta E_{\mathrm{nuc}}^{A} - \Delta E_{\mathrm{nuc}}^{A'}$ can be determined if the other terms on the right hand side of equation (2.29) can be calculated with sufficient accuracy and substracted from the measured isotope shift. An important point is that theoretical uncertainties in the mass-independent quantum electrodynamic correction term $\alpha^3 E_{\mathrm{QED}}^{(0)}$ cancel from the isotope shift, leaving only the much smaller term $\left[\left(\frac{\mu}{M}\right)_A - \left(\frac{\mu}{M}\right)_{A'}\right]\alpha^3 E_{\mathrm{QED}}^{(1)}$, which can be calculated to sufficient accuracy. Without this cancellation, the quantum electrodynamic uncertainties would be comparable in size to the nuclear volume terms of interest, and would prohibit the measurement of the nuclear charge radius.

For the lithium isotopes, the (μ/M)-dependent terms in the right hand side of (2.29) which are identified as the mass shift in (2.15), have been calculated for the $2s\,^2S_{1/2} \rightarrow 3s\,^2S_{1/2}$ transition. The different contributions to the mass shift between ^{11}Li and ^{7}Li are listed in Table 2.8 where the recent measurement of the ^{11}Li nuclear mass of from MISTRAL has been used.

Accuracy is limited by the by the computational uncertainty of the relativistic recoil term. Uncertainty in the QED terms could be significantly reduced when it became possible to calculate the Bethe logarithm contribution to high accuracy for the first time [Yan03].

One effect that has not been included in the theory is the polarization of the nuclear charge distribution by the atomic electrons. To estimate the possible size of this effect,

it is compared to the corresponding correction for the deuteron as discussed by Pachucki *et al.* [Pac96, Eq. (39)]. The correction for the energy of the $1s$ electronic ground state caused by nuclear polarization is -22 kHz, and it scales in proportion to the nuclear polarizability $\alpha_{\rm d}$ and the electron density at the nucleus. For lithium there is a great deal of cancellation for the $2s \rightarrow 3s$ transition because the contribution to the electron density caused by the inner $1s$ electrons is the same. Using the expectation values of the respective δ-functions, the correction to the isotope shift is

$$\Delta E = 7.33 \frac{\alpha_{\rm d}(^{11}{\rm Li}) - \alpha_{\rm d}(^{7}{\rm Li})}{\alpha_{\rm d}({\rm D})} \text{ kHz} , \tag{2.30}$$

where $\alpha_{\rm d}(^{11}{\rm Li})$ and $\alpha_{\rm d}(^{7}{\rm Li})$ are the polarizabilities of the two lithium isotopes, and $\alpha_{\rm d}({\rm D}) = 0.635$ fm^3 is the polarizability of the deuteron. The polarizability of the deuteron is unusually large because it has a low-lying resonance that is accessible by electric dipole transitions. Accurate values for the lithium nuclear polarizabilities are not currently available, but since the experimental accuracy for the isotope shift is about 120 kHz, the polarization correction is negligible, unless the difference $\alpha_{\rm d}(^{11}{\rm Li}) - \alpha_{\rm d}(^{7}{\rm Li})$ is an order of magnitude larger than $\alpha_{\rm d}({\rm D})$.

2.3.3 Nuclear Charge-Radius Determination

An isotope shift measurement provides only information about the difference in nuclear charge radii. To extract absolute charge radii at least the nuclear charge radius from one isotope has to be measured with a different technique. The root-mean-square nuclear charge radius of ^{7}Li , $\overline{r}_{\rm c}(^{7}{\rm Li})$, measured by elastic electron scattering, has been taken as reference. Then the root-mean-square charge radius of the other lithium isotopes can be extracted from the theoretically calculated mass shift $\delta\nu^{A,7}_{\rm MS}$ and a measured isotope shift $\delta\nu^{\rm A,7}$ by

$$\left\langle {r_{\rm c}}^2 \right\rangle_A = \left\langle {r_{\rm c}}^2 \right\rangle_7 + \frac{\delta\nu^{A,7} - \delta\nu^{A,7}_{\rm MS}}{F} , \tag{2.31}$$

where $\overline{r}_{\rm c}(^{7}{\rm Li}) = \sqrt{\left\langle {r_{\rm c}}^2 \right\rangle_7} = 2.39(3)$ fm [Jag74][3], and the electronic factor F and the calculated mass shifts $\delta\nu^{A,7}_{\rm MS}$ values are given in Table 2.9.

2.3.4 Hyperfine Splitting

The orbital motion and the spin of the electrons in the atom generate a magnetic field $\mathbf{B}_0 = \bar{B}_0 \mathbf{J}/\hbar J$ at the position of the atomic nucleus. This field couples to the nuclear

[3]This value is the weighted average of the results in [Jag74], but also coincides with a result form Suelzle *et al.* [Sue67].

Table 2.9. Values for the electronic factor $\mathbb{F}$ [MHz/fm^2] and the mass shift contribution $\delta\nu_{\mathrm{MS}}^{\mathrm{A},7}$ [MHz] for the $2s\,^2S_{1/2} \rightarrow 3s\,^2S_{1/2}$ transition of lithium [Dra05].

Transition	F	$\delta\nu_{\mathrm{MS}}^{6,7}$	$\delta\nu_{\mathrm{MS}}^{7,7}$	$\delta\nu_{\mathrm{MS}}^{8,7}$	$\delta\nu_{\mathrm{MS}}^{9,7}$	$\delta\nu_{\mathrm{MS}}^{11,7}$
$2s \rightarrow 3s$	-1.5661	-11 453.010(56)	0	8 635.113(42)	15 332.025(75)	25 101.812(123)

magnetic moment $\boldsymbol{\mu}_I = -g_I \mu_{\mathrm{N}} \mathbf{I}/\hbar$ and orients the nuclear spin $\mathbf{I}$. The Hamiltonian which describes this interaction is:

$$H_{\mathrm{HFS}} = -\boldsymbol{\mu}_I \cdot \mathbf{B}_0 = \frac{g_I \mu_{\mathrm{N}} \bar{B}_0}{\hbar^2 J} \mathbf{I} \cdot \mathbf{J} \ , \tag{2.32}$$

where g_I/I is the g-factor of the nucleus, μ_{N} is the nuclear magneton, and $\bar{B}_0$ is the averaged magnetic field generated by the electrons at the nucleus.

The total angular momentum of the electrons $\mathbf{J}$ and the nuclear spin $\mathbf{I}$ couple to a total angular momentum $\mathbf{F}$

$$\mathbf{F} = \mathbf{J} + \mathbf{I}, \tag{2.33}$$

where $\mathbf{F}$ must obey the angular momentum rules [May85]. The eigenvalues of $\mathbf{F}^2$ and F_z are $F(F+1)\hbar^2$ and $m_F\,\hbar$ respectively, where F must be an integer or half integer and $m_F = -F,\ -F+1, \ldots,\ F$, all together $2F+1$ values. The corresponding J-energy level splits into several sublevels designated by the quantum number F which can take one of the following values:

$$J + I,\ J + I - 1, \ldots,\ |J - I| \ . \tag{2.34}$$

Depending on whether I is smaller or larger than J, there are $(2I+1)$ or $(2J+1)$ possibilities respectively. The Hamiltonian of this hyperfine splitting (HFS) can then be expressed as,

$$H_{\mathrm{HFS}} = \frac{\mathbb{A}}{2\hbar^2} \mathbf{I} \cdot \mathbf{J} = \frac{\mathbb{A}}{2\hbar^2} \left(\mathbf{F}^2 - \mathbf{I}^2 - \mathbf{J}^2 \right) \ , \qquad \text{with } \mathbb{A} = \frac{g_I \mu_{\mathrm{N}} \bar{B}_0}{J} \ . \tag{2.35}$$

The energy eigenvalues of (2.35) are

$$E_{\mathrm{HFS}} = \frac{\mathbb{A}}{2}(F(F+1) - I(I+1) - J(J+1)) = \frac{\mathbb{A}}{2} C_F \tag{2.36}$$

and represent the energy shift of the hyperfine components F relative to the J-level energy. The C_F are called Casimir coefficients. As it can be seen in Table 2.1, all lithium isotopes have nuclear spin, therefore the $2s\,^2S_{1/2}$ and $3s\,^2S_{1/2}$ levels split into two hyperfine components. For ^{6}Li a schematic representation of the hyperfine splitting is shown in Fig. 2.5.

Table 2.10. Center-of-gravity frequencies ν_{cg} for the $2s\,^2S_{1/2} \rightarrow 3s\,^2S_{1/2}$ electronic transition in lithium isotopes.

I	isotope	F	F'	C_F	$C_{F'}$	ν_{cg}
1	^{6}Li	1/2	3/2	-2	1	$\frac{2}{3}\nu_{3/2} + \frac{1}{3}\nu_{1/2}$
3/2	^{7}Li, ^{9}Li, ^{11}Li	1	2	-5/2	3/2	$\frac{5}{8}\nu_2 + \frac{3}{8}\nu_1$
2	^{8}Li	3/2	5/2	-3	2	$\frac{3}{5}\nu_{5/2} + \frac{2}{5}\nu_{3/2}$

In this case the transition frequency for the $2s\,^2S_{1/2} \rightarrow 3s\,^2S_{1/2}$ has to be taken as the center-of-gravity over all hyperfine components [Ott87]. It should be noted that in first-order perturbation theory, which is usually an excellent approximation, the hyperfine splitting interaction does not shift the center-of-gravity. The center-of-gravity for the $2s \rightarrow 3s$ transition in lithium can be obtained from,

$$\nu_{cg} = \frac{C_F\,\nu_{F'} - C_{F'}\,\nu_F}{C_F - C_{F'}}\,, \tag{2.37}$$

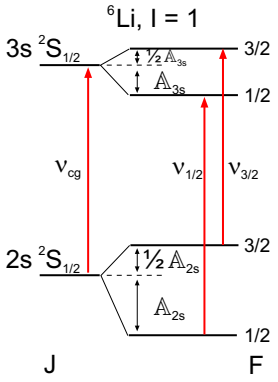

Figure 2.5. Schematic representation of the hyperfine splitting in ^{6}Li.

where ν_F is the transition frequency for the respective F. The resulting formulas for the center-of-gravity frequencies of the different lithium isotopes are given in the right column of Table 2.10.

2.3.5 Zeeman Effect in the Hyperfine Structure of Lithium

So far the hyperfine structure of lithium was treated without the influence of an external magnetic field. However, such external fields are often existing at the experiment location and care must be taken that they do not have a considerable effect onto the transition energies or isotope shift. In such an external static magnetic field $\mathbf{B}_{ext} = B_{ext}\hat{\mathbf{e}}_z$, all hyperfine structure components with $F \neq 0$ split in $2F + 1$ m_F sublevels. For weak magnetic fields, the coupling of the electronic angular momentum **J** and the nuclear spin **I** to **F** is still dominant and the energy shift of the different sublevels can be simply be written as [May85]:

$$\Delta E_{weak} = g_F \mu_B B_{ext} m_F, \tag{2.38}$$

the Zeeman effect of the hyperfine structure. But the coupling of **I** and **J** is weak, because of the small nuclear magnetic moment, and already at moderate field strength the angular

momenta decouple and the Hamiltonian must be rewritten to

$$\begin{aligned} H_{\mathrm{Z}} &= -(\boldsymbol{\mu}_J + \boldsymbol{\mu}_I) \cdot \mathbf{B}_{\mathrm{ext}} \ , \\ &= g_J \mu_{\mathrm{B}} B_{\mathrm{ext}} \frac{J_z}{\hbar} + g_I \mu_{\mathrm{N}} B_{\mathrm{ext}} \frac{I_z}{\hbar} \ . \end{aligned} \tag{2.39}$$

It can be treated as a perturbation term that is added to the hyperfine splitting Hamiltonian (2.35), resulting in the full Hamiltonian

$$H = H_{\mathrm{HFS}} + H_{\mathrm{Z}} = \frac{\mathbb{A}}{2\hbar^2} \mathbf{I} \cdot \mathbf{J} + g_J \mu_{\mathrm{B}} B_{\mathrm{ext}} \frac{J_z}{\hbar} + g_I \mu_{\mathrm{N}} B_{\mathrm{ext}} \frac{I_z}{\hbar} \ . \tag{2.40}$$

The eigenstates E_{HFS} (2.36) of the hyperfine splitting Hamiltonian H_{HFS} are at the same time also eigenstates of the operators $\{\mathbf{F}^2,\ F_z,\ \mathbf{I}^2,\ \mathbf{J}^2\}$. Thus, the matrix for H_{HFS} in the basis $\{|F, m_F\rangle\}$ is diagonal. However, the matrix for the Hamiltonian H_{Z} is diagonal in the basis $\{|m_I, m_J\rangle\}$, which are eigenstates of the operators $\{\mathbf{I}^2,\ I_z,\ \mathbf{J}^2,\ J_z\}$.

For spin 1/2 systems, this problem can be solved analytically, see Appendix A. The resulting dependence of these energy levels as a function of B_{ext} for the $2s$ state in ^{6}Li is shown in Fig. 2.6(a), where $g_J = 2$, $g_I = -0.822$, $\mu_{\mathrm{B}}/h = 1.40$ MHz/G, $\mu_N/h = 7.62\times10^{-4}$ MHz/G, and $\mathbb{A}_{2s}(^6\mathrm{Li})/h = 152.137$ MHz. It exhibits the typical behavior for $s = 1/2$ systems. In the very low fields the Zeeman effect is linear and proportional to m_F, while for large fields the splittings show a regrouping corresponding to the m_J and m_I values. The behavior for ^{11}Li is similar and shown in Fig. 2.6(b).

These dependencies will in Section 5.6.4 be used to extract an estimation of systematic uncertainties caused by the residual magnetic fields in the experimental region.

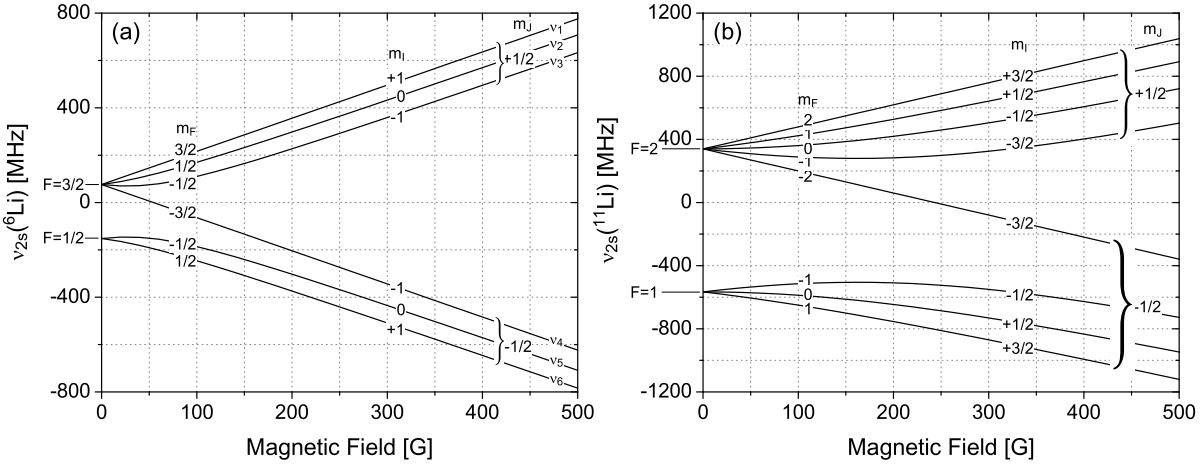

Figure 2.6. Energies of the 2s hyperfine levels of (a) ^{6}Li and (b) ^{11}Li as a function of the applied external magnetic field. $\nu = E/h$.

3 Fundamental Techniques

In this chapter the fundamental techniques that are used for the determination of the isotope shift in the $2s \rightarrow 3s$ two-photon transition in lithium will be presented. The production of radioactive ion beams, Doppler-free and resonance ionization spectroscopy will be covered in some detail.

3.1 Production of High Intensity Radioactive Beams

A well-established technique for on-line production of high intensity and high quality radioactive ion beams is Isotope Separation On-Line (ISOL) [Lin04]. This technique is very attractive because the ions are produced at rest, making it ideally suitable for low-energy experiments. Such an instrument is basically composed of a target, an ion source, and an electromagnetic mass analyzer. Radioactive isotopes are produced by bombarding a thick target, often made of a heavy element like uranium or tantalum, with a high power "driver" beam, *e.g.*, an intense proton beam of several 100 MeV or a high energy ion beam. The reaction products are stopped, they thermalise inside the hot target and diffuse out to an ion source from which they are further accelerated and mass separated. Because many isobars of different elements are produced simultaneously in the target, special care needs to be taken for the right choice of target material, driver beam and ion source in order to obtain large production rates for the desired radioactive isotopes.

The chemically selective steps in the production, which determine to a large part which ions are available from ISOL sources, are the diffusion out of the target and the desorption from the surface. Usually the atoms effuse into some type of ion source, *e.g.* a surface ion source or an electron cyclotron resonance (ECR) ion source. Alkaline elements like lithium are favorite candidates for ISOL facilities since they have high diffusion coefficients, are quickly desorbed from the surface, and can be easily surface ionized. Other species with similar advantages are the rare gases, but an ECR source must be used to ionize the atoms.

Highest intensities of ^{11}Li beams can be obtained by proton induced reactions on heavy targets as it is realized, *e.g.*, at the ISOLDE and TRIUMF facilities. Three main reaction channels are responsible for the bulk production of ions: spallation, fragmentation and fission, as illustrated in Fig. 3.1. The production of the radioactive lithium isotopes is

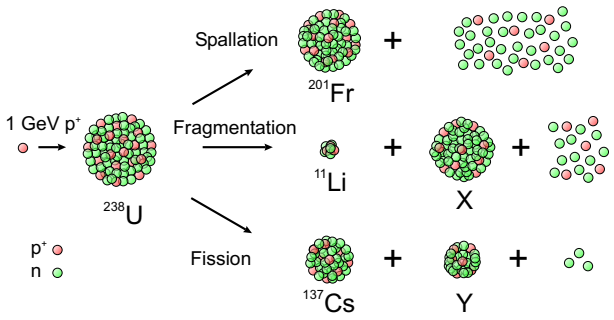

Figure 3.1. Three main reaction channels for ISOL production.

mainly related to the fragmentation channel.

3.2 Doppler-Free Two-Photon Spectroscopy

The accuracy that is needed to obtain a meaningful value for the charge radius of ^{11}Li requires a high-resolution and therefore a Doppler-free technique. Since high efficiency has to be maintained to reach sufficient detection probability for the rare particles, the two-photon spectroscopy has been chosen.

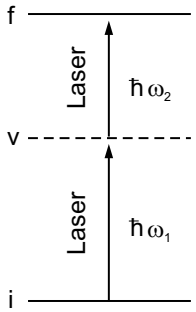

Figure 3.2. Two-photon transition with a "virtual intermediate level" v.

An atom at rest that is irradiated by two laser beams $\boldsymbol{E}_1 = A_1 e^{i(\omega_1 t - \mathbf{k}_1 \cdot \mathbf{r})}$ and $\boldsymbol{E}_2 = A_2 e^{i(\omega_2 t - \mathbf{k}_2 \cdot \mathbf{r})}$ [Dem88] may simultaneously absorb two photons, one out of each laser beam, if the resonance condition

$$E_f - E_i = \hbar(\omega_1 + \omega_2) \tag{3.1}$$

for an atomic transition $i \rightarrow f$ between two energy levels E_i, E_f is fulfilled. If the atom moves with a velocity $\mathbf{v}$ in the laboratory frame, the frequency $\omega = 2\pi\nu$ of the laser with wave vector $\mathbf{k}$ is Doppler-shifted in the reference frame of the moving atom,

$$\omega' = \frac{\omega - \mathbf{k} \cdot \mathbf{v}}{\sqrt{1 - v^2/c^2}} = \omega - \mathbf{k} \cdot \mathbf{v} + \frac{\omega}{2}\frac{v^2}{c^2} - \cdots \ . \tag{3.2}$$

The resonance condition (3.1) will now change to

$$(E_f - E_i)/\hbar = (\omega_1' + \omega_2') = (\omega_1 + \omega_2) - \mathbf{v} \cdot (\mathbf{k}_1 + \mathbf{k}_2) + \frac{(\omega_1 + \omega_2)}{2}\frac{v^2}{c^2} + \cdots \ . \tag{3.3}$$

Two lasers with equal frequencies $\omega_1 = \omega_2 \equiv \omega$ traveling in opposite directions have wave vectors $\mathbf{k_1} = -\mathbf{k_2}$ and (3.3) shows that the first-order Doppler shift of the two-photon transition vanishes:

$$(E_f - E_i)/\hbar = 2\omega + \omega\frac{v^2}{c^2} + \cdots \ . \tag{3.4}$$

If the atom has a thermal velocity $(v/c) \ll 1$, the second-order Doppler shift is negligible as long as the experiment does not require an accuracy on the order of few kHz. Thus, all the atoms in a gas sample with Maxwellian velocity distribution absorb the same sum frequency $\omega_1 + \omega_2 = 2\omega$. The typical lineshape of a two-photon transition is shown on a logarithmic scale in Fig. 3.3. Integration over all velocity classes leads to a strong Doppler-free Lorentzian profile for atoms absorbing photons of opposite direction and a Doppler-broadened Gaussian background from atoms absorbing photons propagating in the same direction. Quantitatively, the area under the Doppler-free line is twice that under the Doppler-broadened line [Dem88]. When the homogeneous width of the Doppler-free Lorentzian profile is Γ_{L}, its magnitude therefore exceeds that of the background by a factor $2\Gamma_{\mathrm{BG}}/\Gamma_{\mathrm{L}}$, where Γ_{BG} is the width of Doppler-broadened Gaussian background.

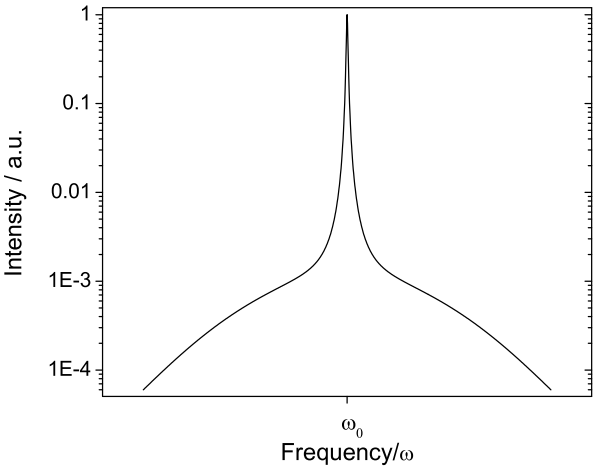

Figure 3.3. Lineshape of a two-photon transition.

The two-photon transition rate R for the transition from the ground state i to the excited state f is proportional to

$$R \propto I^2 \left| \sum_{k=1}^{n} D_{i\,k}\, D_{k\,f} \left(\frac{2}{E_k - \hbar\omega} \right) \right|^2 , \tag{3.5}$$

where I is the intensity of the laser beam. The summation is over all possible intermediate states k having energies E_k, and electric dipole moment matrix elements $D_{i\,k}$, $D_{k\,f}$ connecting them to the ground as well as the excited state. For an $s \rightarrow s$ transition, as it is used in the case of lithium, the transition is realized only through the far reaching wings of the off-resonant p-states. Equation (3.5) indicates that high intensities are needed to saturate the two-photon transition and that the efficiency increases with the square of the laser intensity. Thus, an optical resonator around the interaction region is used to provide photons from both directions as well as sufficient laser intensity [Ewa05].

If F is the total angular momentum of the atom, as described in section 2.3.4, then the general two-photon selection rules to connect the initial state i and the final state f are [Bon84]: $|\Delta F| = |F_f - F_i| \leq 2$, F_i and F_f must have the same parity, $F_i + F_f =$ integer. Two-photon transitions are also dependent on the polarization of the light. For example, two parallel laser beams, one with right-handed circular polarization (σ^+) and the other

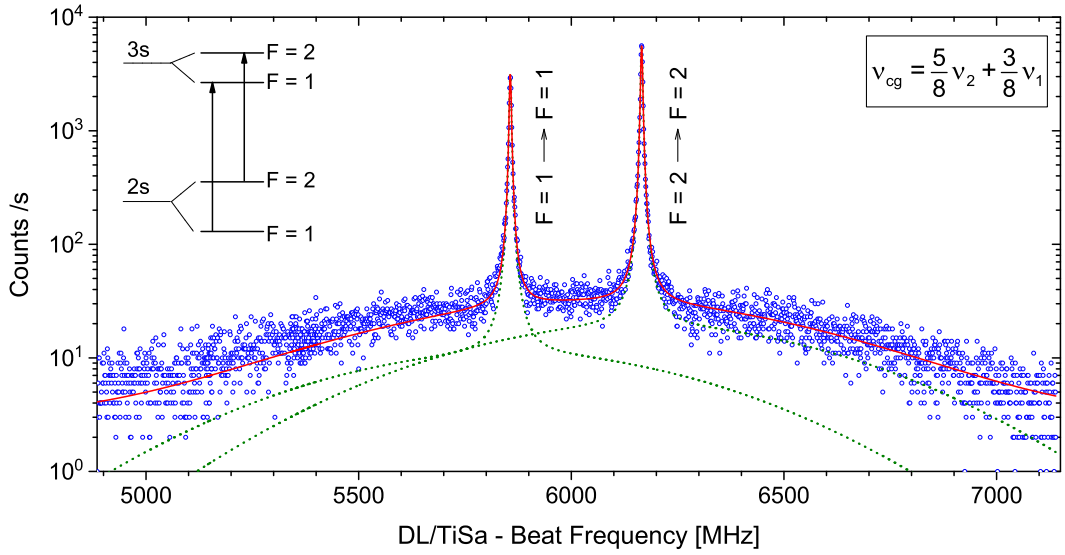

Figure 3.4. Lineshape of the ^{7}Li resonance in the 2s → 3s two-photon transition.

with left-handed polarization (σ^-), induce two-photon transitions with $\Delta m_F = m_{F_f} - m_{F_i} = 0$. The last rule is also valid for two parallel laser beams with linear polarized light (π). In the special case of an $s \rightarrow s$ transition the selection rule $\Delta F = 0$ has to be fulfilled.

Figure 3.4 shows an overall resonance profile obtained for ^{7}Li [Ewa05]. As it has been already described in Section 2.3.4, the nuclear spin of ^{7}Li $I = 3/2$ causes the splitting of the atomic energy levels into their hyperfine components. The narrow Doppler-free components are labelled with their respective F quantum numbers. Each of the two peaks was fitted with a Voigt plus a background Gaussian function represented by the green dotted lines. The Voigt profile is the convolution of a Lorentzian profile with a homogeneous linewidth Γ_{L} and a Gaussian profile mainly determined by the linewidth of the laser Γ_{G}. The solid red line is the overall fitting function. Such spectra were recorded to investigate and understand the lineshape of the resonance profile [Ewa05]. A good description of the lineshape is important for an accurate determination of the lineshape without systematics shifts, caused *e.g.*, by asymmetries that are not taken into account. The overall fitting function in Fig. 3.4 shows an excellent agreement with the experimental data points over more than 2 GHz frequency range and about 4 orders of magnitude experimental signal intensity.

3.3 Resonance Ionization Spectroscopy

Resonance Ionization Spectroscopy (RIS) monitors the absorption of photons on an atomic or molecular transition $i \rightarrow f$ by detecting ions or electrons, produced by some means out

of the excited state f. The ionization of the excited atom can for example be performed by a photoionization process,

$$A(i) \xrightarrow{+\hbar\omega} A(f) \xrightarrow{+\hbar\omega'} A^+ + e^- + E_{\text{kin}} \ , \tag{3.6}$$

where the ionizing photon, with a frequency ω', may come either from the same laser which has excited the level f ($\omega = \omega'$), or from a separate source of light, *e.g.*, another laser. The advantage of this technique lies in the large excitation and photoionization cross sections and in the fact that the produced charged particles can be detected with almost 100% efficiency while, *e.g.*, fluorescence detection is always hampered by relatively small solid angles.

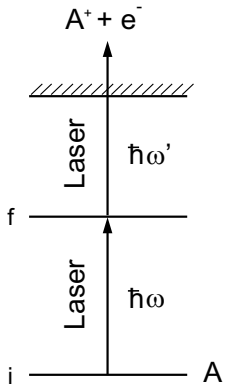

Figure 3.5. General level scheme for a simple resonance ionization process.

Figure 3.6 shows the Li I level scheme with the chosen path for the resonance ionization. Lithium atoms in the $2s$ ground state are excited via the Doppler-free two-photon transition to the $3s$ state, with laser light of 735 nm. As it has been described above, this transition offers a narrow resonance line as well as efficient excitation since all velocity classes are excited simultaneously. This two-photon step is followed by a spontaneous decay into the $2p$ states which decouples the $3s$ state from the ionizing laser and thus crucially reduces AC-Stark broadening and AC-Stark shifts [Sch00, Ewa05]. The decay is followed by a resonant excitation into the $3d$ state at 610 nm and subsequent photoionization by absorbtion of a photon at either 735 nm or 610 nm.

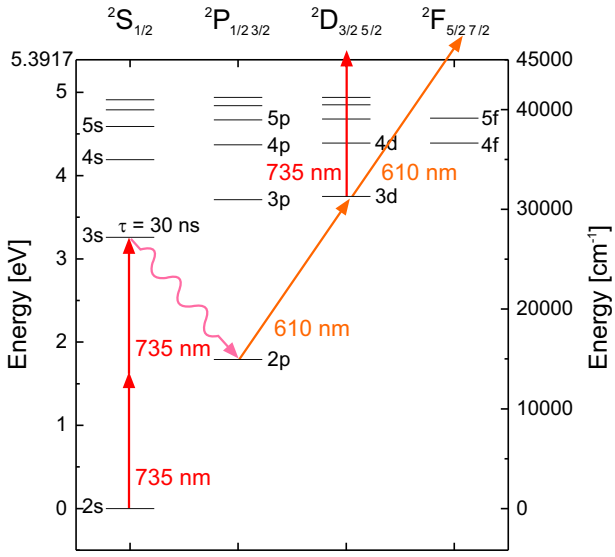

Figure 3.6. Resonance ionization scheme for lithium.

This process has the advantage that a produced photo-ion can be detected with a very high efficiency. An appropriate device for this process is a quadrupole mass spectrometer, that can at the same time be used to suppress background ions, generated by other processes, *e.g.*, by surface ionization.

3.4 Quadrupole Mass Spectrometer

A quadrupole mass spectrometer (QMS) [Pau53] is a very compact device that can be readily combined with continuous wavelength (cw) resonance ionization to provide additional suppression of unwanted ions of different mass [Bus87]. In these applications it is often operated in a mode where it does not provide very high resolution but transmission of almost 100% and suppression of neighboring masses at $A \pm 1$ of 10^8 or higher. Other advantages like for example: (a) suppression of the background due to residual gas collisions, (b) low acceleration voltage at the ionization region, (c) rapid switching between masses without magnetic hysteresis and finally (d) the small size and low cost, make the quadrupole mass spectrometer or mass filter an extraordinarily useful device.

The geometry of a quadrupole mass spectrometer with electrodes of circular cross-section is shown in Fig. 3.7. For mass analysis, a combination of a static (dc) electric potential U and an alternating (ac) potential $V\cos(wt)$ in the radio frequency range is applied to the rod: $\Phi_0(t) = U + V\cos(wt)$. The relative amplitudes of the dc and ac potentials control the ability of the system to separate different masses in a low energy beam of ions travelling along the z-axis with typical energies on the order of 5 eV. In

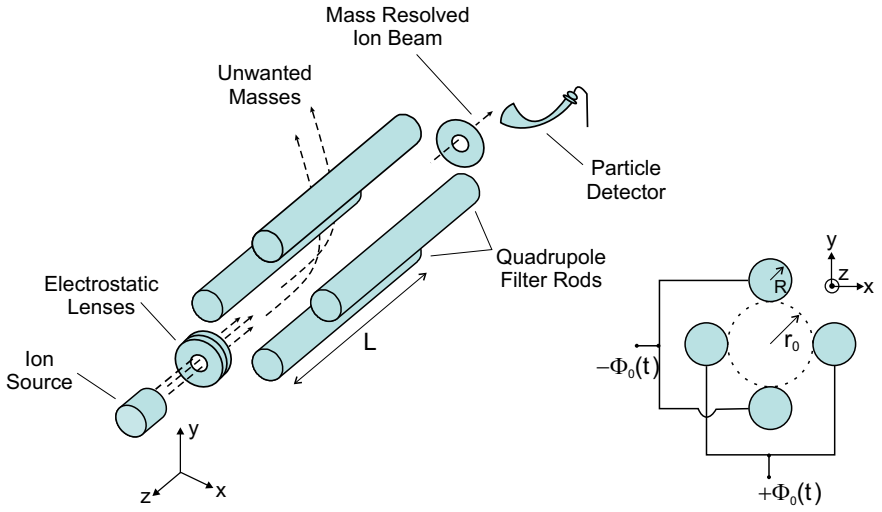

Figure 3.7. Schematic diagram of the typical quadrupole mass spectrometer consisting of an ion source, rod system, and particle detector. The free field radius is r_0, the rod radius and rod length are R and L respectively.

the $x - y$ direction they make a complicated oscillation movement which is governed by the Mathieu equations. The oscillation amplitude of ions with wrong mass grows exponentially until the ions hit a rod, whereas the amplitude of ions with the right mass stays finite. Those which pass through the system are detected with a single-particle detector.

4 Experimental Setup

Figure 4.1 shows a simplified scheme of the experimental arrangement for laser spectroscopy of the Doppler-free $2s \rightarrow 3s$ two-photon transition in lithium as it will be discussed in this chapter. The lithium ions produced in an ISOL-type ion source are accelerated to 30 keV, mass separated and transferred to the experimental area where they are stopped in a thin carbon catcher which is heated to about 1800 °C with a CO_2 laser. The implanted lithium diffuses quickly out of the foil and atoms, released from the surface, drift into the ionization region of a quadrupole mass spectrometer. At this point the lithium atoms are resonantly ionized with laser light at 735 nm (provided by a titanium-sapphire laser) and 610 nm (generated by a dye laser) using the ionization scheme described in Section 3.3:

$$2s\,^2S_{1/2} \xrightarrow{2\text{x}735\text{nm}} 3s\,^2S_{1/2} \xrightarrow[\tau\approx 30\text{ns}]{\text{decay}} 2p\,^2P_{3/2,1/2} \xrightarrow{610\text{nm}} 3d\,^2D_{3/2,5/2} \xrightarrow{610\text{nm},735\text{nm}} \text{Li}^+ \,. \quad (4.1)$$

The created photo-ions are then mass analyzed with a quadrupole mass spectrometer and detected with a continuous dynode electron multiplier (CDEM) detector. The isotope shift in the $2s \rightarrow 3s$ transition is measured by tuning the 735 nm light across the lithium resonances.

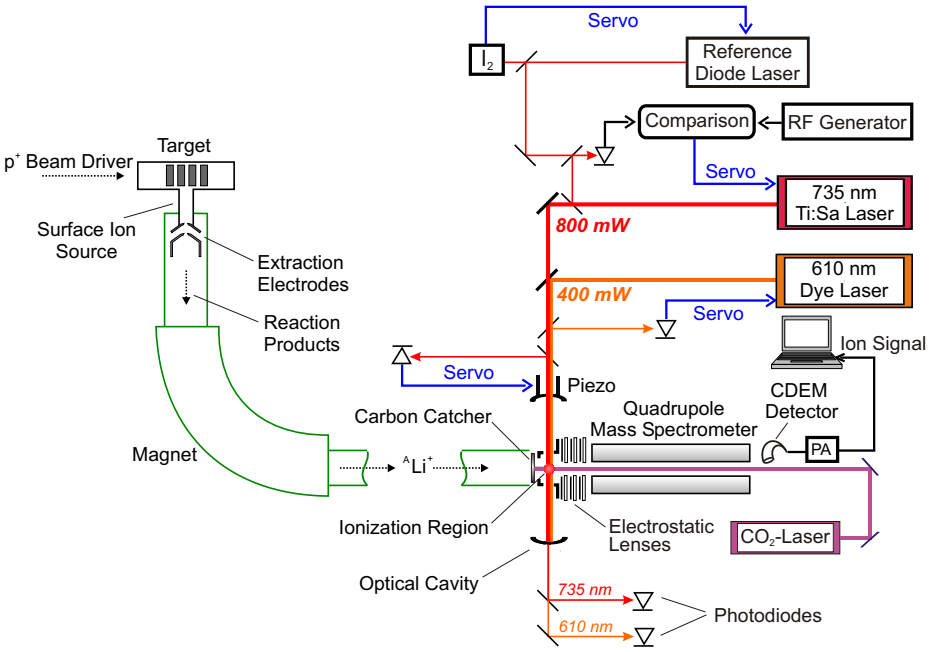

Figure 4.1. Experimental setup to measure the $2s\,^2S_{1/2} \rightarrow 3s\,^2S_{1/2}$ electronic transition in lithium.

In the following sections a detailed description of the experimental setup is given with a focus on the changes that were necessary to adapt the experiment to the small production rates of ^{11}Li and the conditions at the Isotope Separation and Acceleration (ISAC) facility at TRIUMF, Vancouver BC, Canada.

4.1 The ISAC Facility at TRIUMF

4.1.1 Cyclotron

The beamlines and experimental facilities of TRIUMF are shown in Fig. 4.2. Location of the ToPLiS experiment is also indicated. The heart of TRIUMF is a cyclotron which

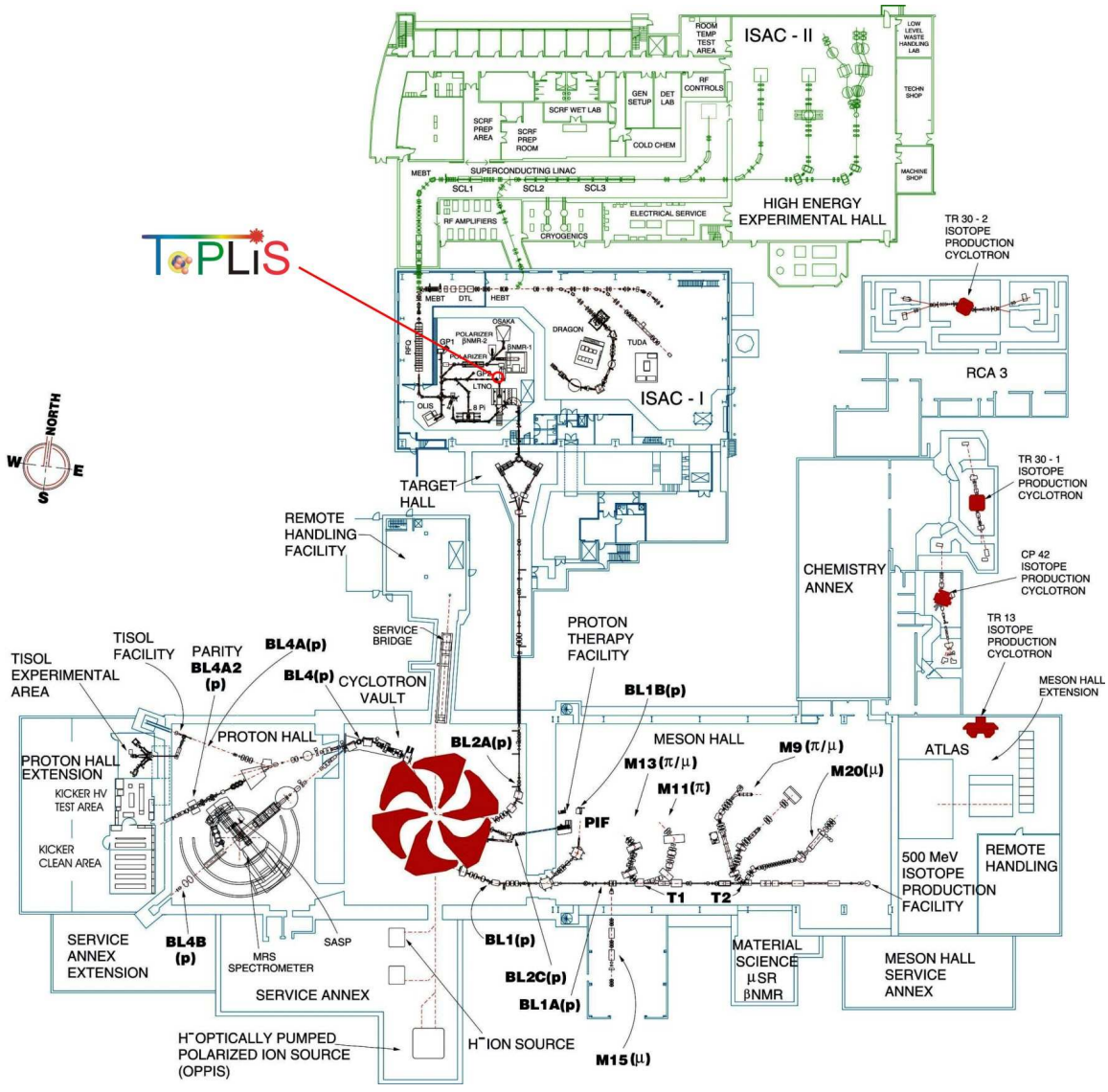

Figure 4.2. Beamlines and ISAC experimental halls at TRIUMF.

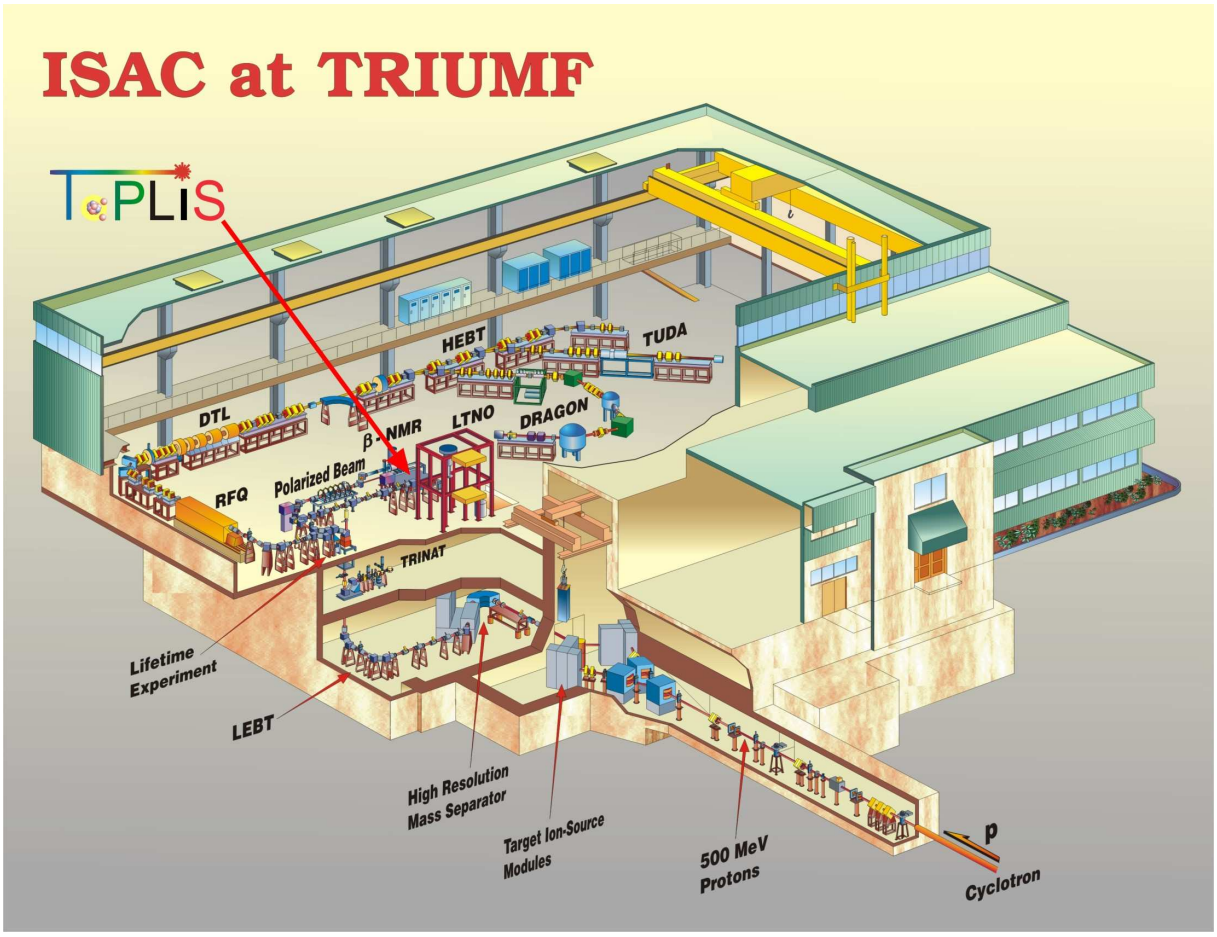

Figure 4.3. The ISAC facility at TRIUMF.

can produce a proton current as large as 400 µA at a maximum energy of about 520 MeV. The cyclotron has six huge magnets, arranged in a "pinwheel" pattern as shown in Fig. 4.2. These magnets produce a magnetic field as large as 5600 G that holds H^- ions in a spiral path while they are being accelerated by an electrostatic potential with a nominal operation frequency of about 23 MHz. After acceleration, the protons are produced by stripping the electrons off from the H^- ions using a 25 µm thick stripping carbon foil. The extraction efficiency is 99.95 %. The extracted beam has a typical energy spread of 1 MeV and is directed along the injection beam line BL2A—a 50 m long underground tube—towards the online ion source of the ISAC facility, shown in Fig. 4.3. Here a 15° switching dipole steers the beam to either one of the two heavily shielded target stations, which contain proton beam monitoring equipment, the production target and ion sources, a beam dump, and the front-end ion optics [Bri99].

4.1.2 Radioactive Beam Production

Figure 4.4 shows a photo of a target ion source as it is used at ISAC for the production of radioactive ions. The p^+ beam enters the 18 cm long tantalum tube and hits the target foils which are stacked inside the tube. Using foils of refractory material, like tantalum, up to 40 µA proton beam current can be accommodated. The target ion source is mounted on ceramic insulators on a water cooled copper support plate and surrounded by a water cooled copper heat shield. It is operated at variable high voltages up to 60 keV. The extraction electrode is at a variable negative voltage with respect to the target ion source. There is also a ground electrode which is separated from the surrounding ground to allow current measurements of the beam hitting the electrode.

Target development has been a key issue at ISAC during the last years. Standard targets, as shown in Fig. 4.4, typically provided yields for ^{11}Li on the order of a few 10 000 ions/s at proton beam currents of 40 µA. The production rate of radionuclides usually scales with the proton beam current [Dom00]. In order to achieve even higher yields, a new target design, called "high-power target", that was able to sustain up to 70 µA proton beam current was tested during the ToPLiS beam time in October 2004. However, due to problems with the alignment of the new target and the proton beam steering into the target region, the operating conditions were not optimal and even at proton currents of 60 µA the production of lithium isotopes was lower than with the standard target. Therefore a standard target which was mounted on the second target station was used

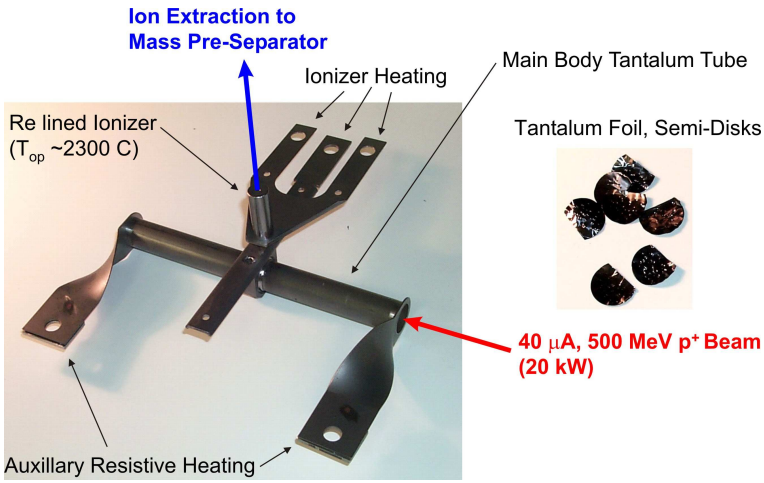

Figure 4.4. Production target. It consists of an 18 cm long and 19 mm diameter tantalum tube filled with 525 semi-disks made from tantalum foil. The operational temperature of the foils is about 2000 °C. A second tantalum tube intersects the target tube orthogonally and it is the sole means of escape for products from the target and serves as the surface ionizing source.

Table 4.1. Typical ion yields of radioactive lithium ions produced at ISAC with a standard and a high-power-type tantalum target during the beam times for the ToPLiS experiment. The measurement of the ion yields were done using a beta detector.

Beamtime	Tantalum Target		p^+ beam		Yields [ions/s]		
	Type	Status	Current[μA]	Energy [MeV]	$^8Li^+$	$^9Li^+$	$^{11}Li^+$
Sep 04	standard	used	40	500	10^8	10^6	-
Oct 04	high power	new	60	500	7.7×10^8	1.1×10^8	-
		new	68	500	-	-	8.4×10^3
	standard	new	40	500	8×10^8	9×10^7	3.5×10^4

later on. Target types, operating conditions and ion yields during the ToPLiS runs are summarized in Table 4.1.

4.1.3 Mass Separator and Beam Transport

The two-stage mass separator can handle beams from mass 6 to 238 amu with source extraction voltages between 12 and 60 keV. Preliminary mass selection is achieved using a 60° pre-separator magnet. This acts as a cleaning stage in order to limit the radioactive contamination of the main separator. The pre-separator is followed by the main separator which is a 120° dipole magnet. A fast switch (kicker) is installed behind the main mass separator and can be used for turning the ion beam on and off. The mass separated ion beam is then transported into the ISAC low-energy experimental area. At the entrance into the hall, a counting station is installed where the ion yields can be detected. The beamlines at ISAC contain ion beam steering, monitoring, and focussing equipment. The ToPLiS experiment was added to the GP3 beamline. In order to have the necessary freedom for ion beam steering and focussing, the beamline was extended with a pipe containing an electrostatic quadrupole triplet, two deflectors and a Faraday cup. The geometry is shown in Fig. 4.5.

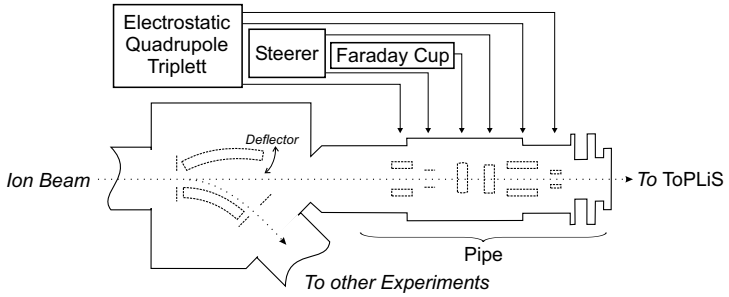

Figure 4.5. Steering and focussing equipment for the ToPLiS experiment at ISAC.

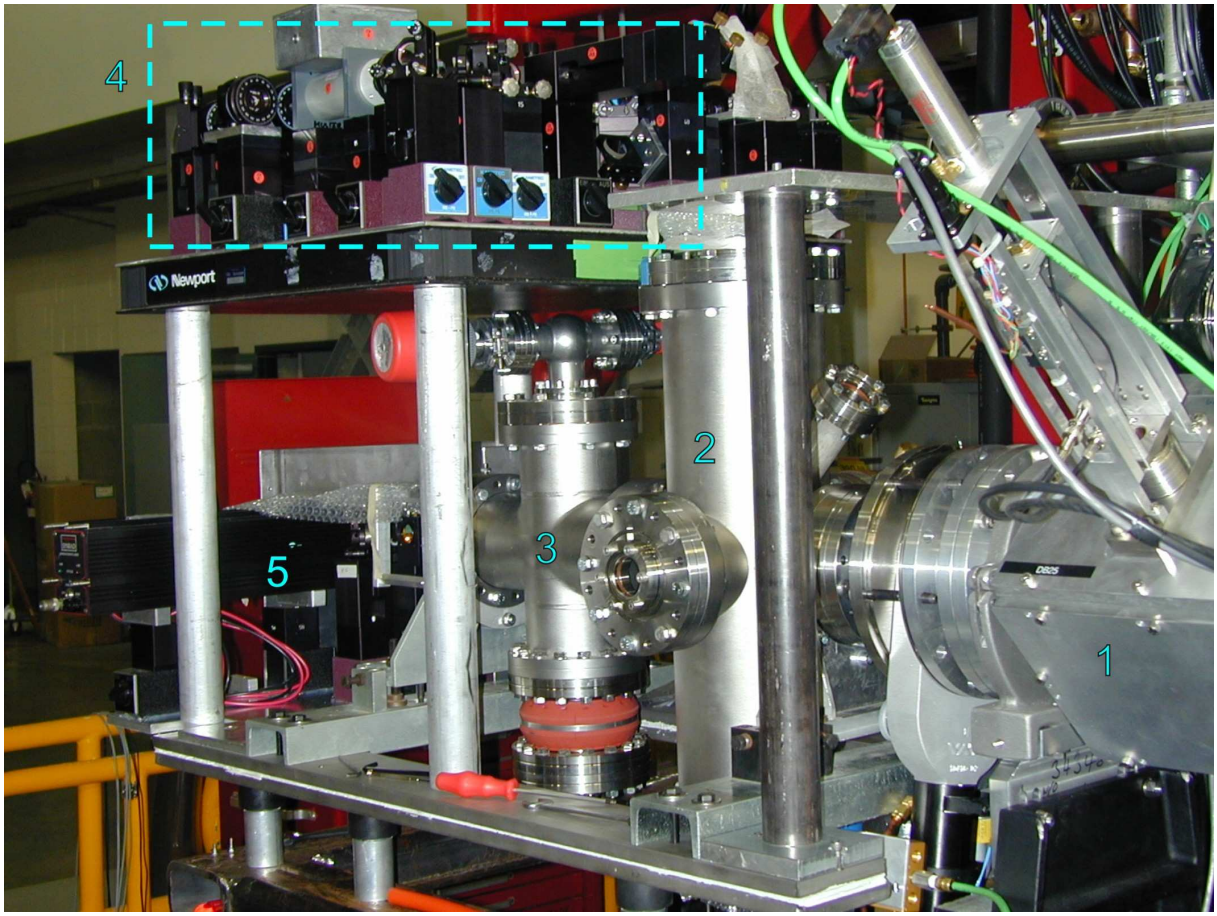

Figure 4.6. ToPLiS experimental apparatus at ISAC. (1) End of the GP3 beamline with a pipe containing ion beam steering and focussing elements. Vacuum chamber containing (2) the optical resonator and (3) the quadrupole mass spectrometer. (4) Optics for the stabilization of the optical resonator and dye laser. (5) CO_2 laser.

4.2 The ToPLiS Setup

In the following sections (4.2.1 - 4.2.5) the setup is described from the point of view of a lithium ion that arrives at the experimental station. The lithium ion is first stopped and neutralized in a carbon catcher foil (4.2.1), evaporated (4.2.3), then again ionized by laser excitation and finally guided through a quadrupole mass spectrometer (4.2.2) before detection. Operation of the ion optical elements in the beamline for focusing and steering the ion beam onto the right spot on the carbon catcher are described in (4.2.4). A special procedure was developed to achieve this overlap for the very small ion yields of ^{11}Li. In order to keep track of the radioactive ion beams (4.2.5) particle and photon detectors were installed nearby the experimental station. Section 4.2.6 gives a summary of the laser system, which has been described in detail in [Ewa05].

4.2.1 Carbon Catcher

In front of the interaction region, the mass separated lithium ion beam is stopped and neutralized inside a carbon catcher. The thickness of the catcher was chosen from SRIM simulations [Ewa05] in order to stop the ions shortly before they leave the catcher foil again. The catcher foils with thickness of about 300 nm (see right part of Fig. 4.7) were prepared in the GSI target laboratory and glued onto a stainless-steal holder, providing three positions equipped with catchers of different thickness and a hole. Additionally, a small channeltron detector is attached to the holder. This device is for direct detection of the weak ^{11}Li ion beams as discussed in Section 4.2.4. The target holder is mounted on a linear feedthrough that moves the holder along the x-position so that different foils can be located in front of the quadrupole mass spectrometer. The feedthrough itself can be moved in y and z directions, as indicated schematically in the left part of Fig. 4.7, so that the vertical position of the catcher and the distance to the quadrupole mass spectrometer ion optics can be changed. Fast release is essential for the measurements of the ^{11}Li isotope which has a half-life of only 8.5 ms. In order to achieve this, a small spot of only 2 mm diameter is heated to about 1800 °C with a CO_2 laser beam that is coupled into the system along the axis of the quadrupole mass spectrometer. When the lithium ions are implanted into the hot carbon catcher, they are mainly released as neutral atoms but ions

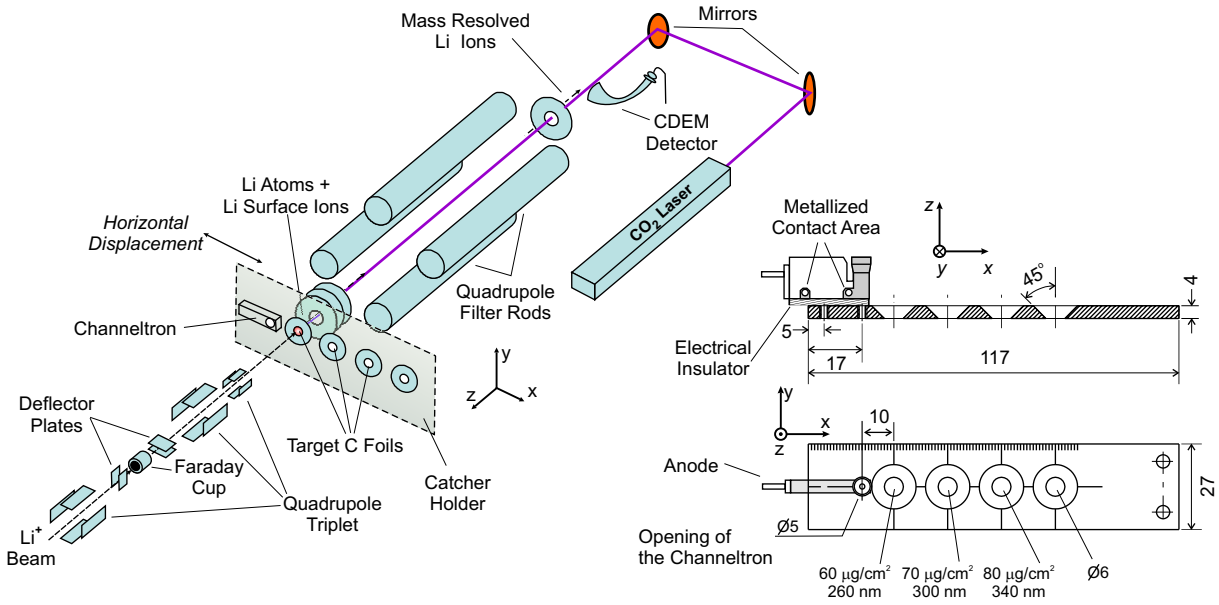

Figure 4.7. Left: Schematic representation of how the carbon-foil holder is mounted in front of the ionization region of the quadrupole spectrometer. Right: Carbon catchers of different thickness mounted on a stainless-steal holder. The position of a small channeltron on the target holder is also given. Dimensions are given in mm. The holder is fixed to a linear feedthrough that can be moved horizontally and vertically in the x- and y-direction.

are also created on the hot catcher surface. About 10^{-4} of the incoming ions are released as surface ions under standard operating conditions [Ewa05].

4.2.2 Quadrupole Mass Spectrometer Settings

The quadrupole mass spectrometer that is used for the ToPLiS experiment is a commercial instrument from ABB Extrel (Model No. 150 QC) with a free-field radius of $r_0 = 19$ mm and it is operated at a radio frequency of 2.9 MHz. This model provides transmissions close to 100 % and an excellent neighboring mass suppression as it has been demonstrated in simulations [Bla00] and ultratrace analysis applications [Wen99, Bla00, Bus00]. The ionization region of the device has been adapted for the purpose of this experiment. The axial electron-impact ion source was removed and the extraction- and ion-region electrodes were replaced. The design of the ionization region and the subsequent ion optical lens system is shown in Fig. 4.8. The QMS ion optics can be operated to accept either the laser ions created resonantly inside the ion region or the surface ions created on the hot carbon catcher. In the first mode, a positive potential of 3.9 V relative to the catcher at ground potential is applied to the ion region; this efficiently repels the surface ions, while neutral atoms can enter. The potential difference between the catcher and the ionization region is still small enough that electrons, emitted from the hot catcher surface and accelerated into the ion region, do not gain enough energy to ionize lithium atoms via electron impact ionization (ionization potential: 5.39 eV). Laser ions created by resonance ionization are then extracted with the negative extractor voltage and focussed into the QMS rod structure using the remaining electrostatic lenses. In the second mode, surface ions are accelerated into the QMS with a negative voltage at the ion region and the extractor is operated as another lens for adapting the beam properties to the QMS acceptance. Ion optical settings of all lenses for both detection modes are summarized in

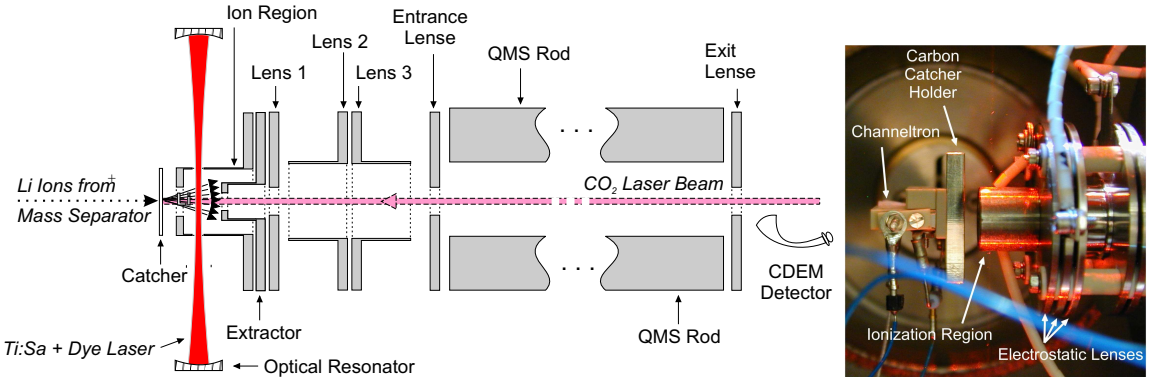

Figure 4.8. Schematic representation of the electrostatic ion optics of the quadrupole mass spectrometer. The picture on the right shows the ionization region and the catcher holder.

Table 4.2. Settings for the electrostatic ion optics in volts for the detection of either surface ions or resonant laser ions.

	Ion Region	Extractor	Lens 1	Lens 2	Lens 3	Entrance Lens	pde bias	exit lens
Laser Ions	+3.9	-9	-43	+8	-43	+2	0	-2
Surface Ions	-4.9	-165	-60	-310	-60	-7	-1.4	+9

Table 4.2. Ions transmitted through the rod system are focussed with an exit lens and detected with a continuous dynode electron multiplier (CDEM) detector. The properties of this detector will be discussed later in Section 4.2.4. In this case the CDEM detector model (DeTech 5402AH-021) was chosen for a very low dark count rate. Typical rates for these devices are on the order of 5-20 mHz.

For the mass suppression between two neighboring isotopes, the quadrupole mass spectrometer was tested with ions of the stable isotopes ^{6,7}Li produced by surface ionization in the hot carbon catcher. Ion optical parameters were optimized in order to obtain a flat top profile with steep flanks and maximum transmission. An example for the peak profile of surface ions is shown in Fig. 4.9. Typically, a suppression of neighboring masses of $> 10^8$ was achieved. The dark count rate of the CDEM detector was about 10 mHz.

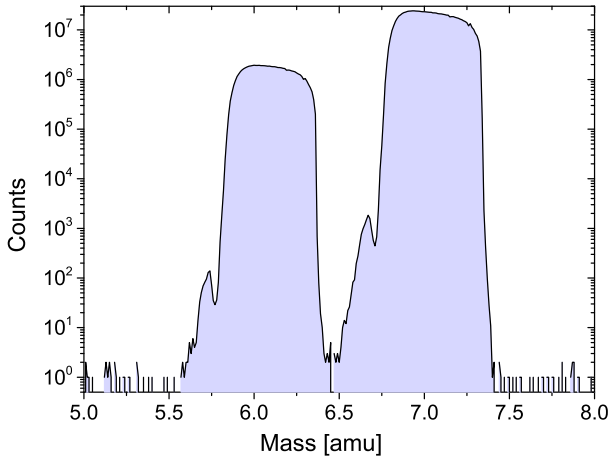

Figure 4.9. Mass spectrum for the detection of surface-ionized lithium.

4.2.3 Release Time Measurements

The release time of the lithium atoms from the graphite catcher was measured by observing the increase of surface ions as a function of time after turning the ion beam on. For this purpose the fast kicker at the mass separator was used, the electrostatic ion optics of the quadrupole mass spectrometer were set for surface ion detection and the output of the CDEM detector was fed into a fast timing amplifier (Model FTA 810L) for linear pulse

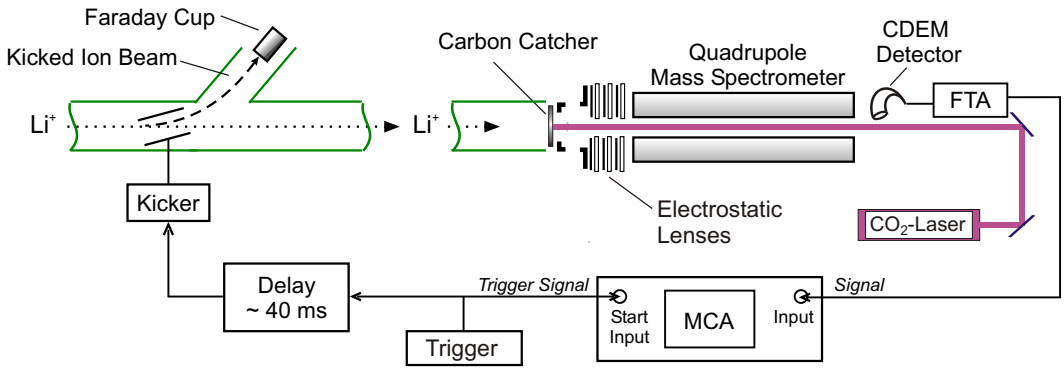

Figure 4.10. Schematic of the setup used to measure the release time of lithium out of the carbon foil.

amplification. The amplified signal was recorded with a multichannel analyzer (MCA, Model ORTEC TRUMP-PCI MCA) operated in a multi-channel scaler mode. Figure 4.10 shows the setup: A TTL signal was delivered to the "Start" input of the MCA and, with a time delay of approximately 45 ms, to the fast kicker controller. First measurements were performed using a ^{9}Li ion beam, but the fast rising flank of the surface ions was obscured by slow saturation of the CDEM signal caused by the α decay of the ions implanted in the CDEM as shown in Fig. 4.11(a). To avoid this complication, a beam of stable ^{6}Li was used. The signal observed with a time resolution of 500 µs is shown in Fig. 4.11(b). The rise time is obviously less than 1 ms and limited by the MCA resolution. Thus, the measurement was repeated with 50 µs step width and the result is shown in Fig. 4.11(c). The ion signal rises to about 70% of the total signal within 100 µs and is then followed by a slightly slower increase to the full intensity which is reached after about 300 µs. This is only 3% of the ^{11}Li half-life and clearly sufficient to have a good release efficiency for this isotope.

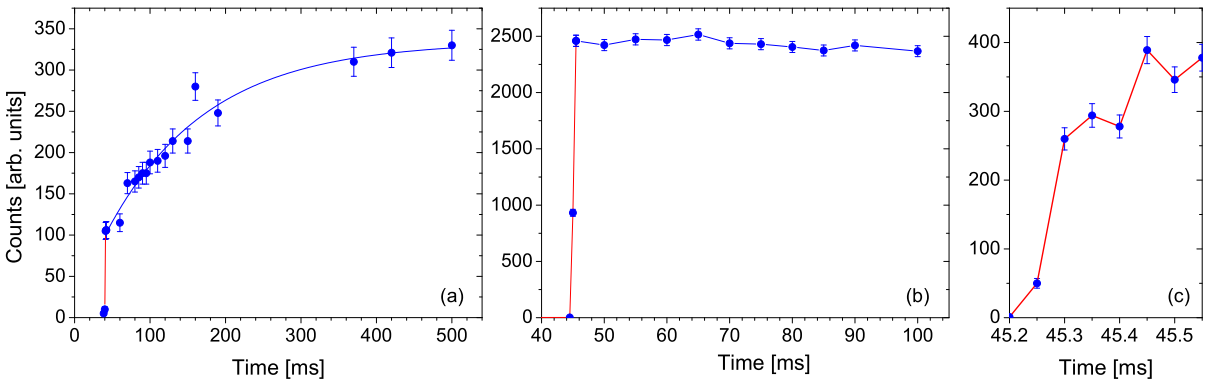

Figure 4.11. Time resolved surface ion release recorded for (a) ^{9}Li and (b, c) ^{6}Li to determine the release time.

4.2.4 Ion Beam Alignment

4.2.4.1 Lithium-6, -7, -8, and -9 Beams

To achieve a highly efficient transformation of the ion beam into slow atoms, the ions must be implanted into the small hot spot at the carbon catcher foil that is heated by the CO_2 laser beam. Focusing and steering of the ion beam is realized with the electrostatic quadrupole triplet and the deflector plates in front of the catcher (see left part of Fig. 4.7). Once the electrostatic optics of the QMS was set to detect surface ions, the settings of the steerer and quadrupole triplet were optimized onto the hot-spot (see Fig. 4.8) of the catcher for ^{6,7,8,9}Li by changing the electrostatic quadrupole and steering settings until the maximum rate of surface ions was obtained. For ^{11}Li this approach could not be used since the ion beam of 30 000 ions/s produced only ∼3 surface ions per second which are not sufficient for optimization. Thus, a more direct method had to be developed that will be presented in the next section.

4.2.4.2 Lithium-11 Beams

For the direct detection of the low intensity beam of ^{11}Li ions, a small CDEM was mounted onto the target holder. A CDEM, offen called "channeltron", is a detector that responds to charged particles, hard and soft X-rays, and ultraviolet radiation. The inner surface of the channeltron is coated with a high-resistive layer. When a potential is applied between the input and output of this device the resistive surface acts as a continuous dynode. A dynode has the property of emitting secondary electrons when primary particles impinge upon it. The secondary electrons are accelerated down the channel by a positive bias until they strike the surface again and generate further secondary electrons, an effect that is enhanced by the curvature of the channel. When the avalanche reaches the anode, an electron cloud containing about 10^8 electrons has been generated. This electron cloud is collected at the anode and a single pulse with a typical pulse duration of approximately 10 ns (FWHM) is produced. Figure 4.12 shows schematically the Channeltron (type: KBL5RS/R, Sjuts Optotechnik GmbH) and the readout and pulse shaping electronics

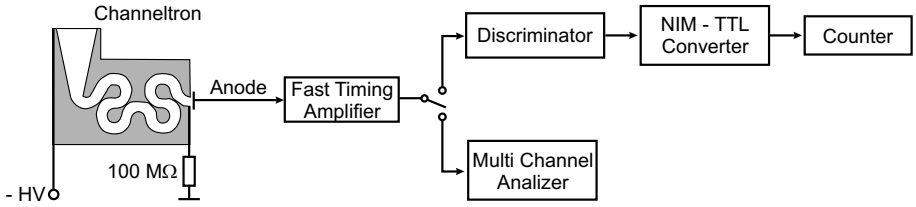

Figure 4.12. Setup for measuring the $^{11}Li^+$ yield with a Channeltron. A negative high voltage (HV = 2000 V) is applied at the Channeltron input.

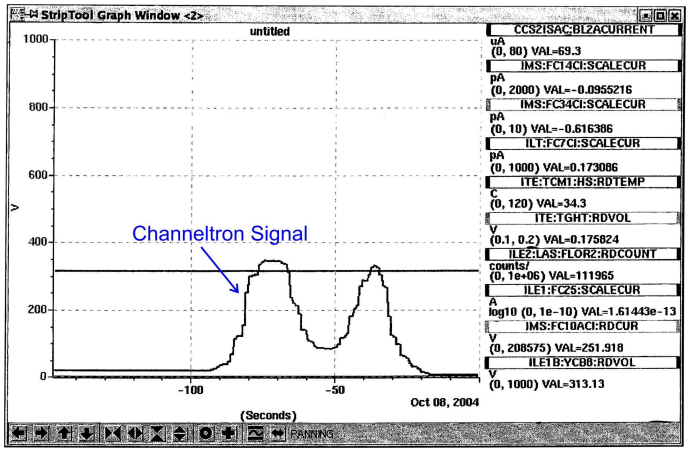

Figure 4.13. Profile of the channeltron counts while the target holder was moved manually in horizontal direction. The two maxima represent its border, the minimum its center.

that was used to detect the ^{11}Li ions. The channeltron model was chosen because of its small size (length×width×height = $27 \times 6 \times 14$ mm) which allows the arrangement on the carbon-catcher holder as shown in the right part of Fig. 4.7. To make sure that the ^{11}Li ion beam hits exactly the hot region of the carbon foil a two-step procedure was developed. First, a ^{9}Li ion beam is used and its position is optimized by observing the surface ion count rate as described previously. Next, without any changes of the beam line settings, the ^{9}Li ion yield is reduced about three orders of magnitude by closing slits located behind the mass separator. This reduction is detected by a Faraday cup placed in front of the hot carbon foil. Then the CO_2 laser beam is blocked and the Faraday cup is taken out of the ion beam path. Now the target holder is moved horizontally until the weak $^{9}Li^{+}$ beam hits the channeltron. Figure 4.13 shows a typical behavior of the count rate detected with the channeltron while the target holder is moved horizontally (for example, from right to left). The two maxima represent the channeltrons edge while the minimum represents its center. This is caused by the fact that the pulses triggered by ions which enter deep into the central channel of the CDEM are offen not sufficiently amplified to trigger the discriminator. The vertical position of the channeltron is now slightly changed and the procedure repeated until the best contrast ratio between the two peaks and the center minimum is observed. Then the channeltron is moved to the minimum. With the holder position fixed at the minimum, the ^{11}Li ion beam is now selected with the mass separator. The mass separator settings and the steerer voltages along the beam lines are scaled with respect to the mass difference. Fine tuning of the exact beam position is then done using the electrostatic steerer plates in front of the catcher foils. The beam is tuned across the channeltron in vertical and horizontal directions. Figure 4.14 shows the surface ion rate

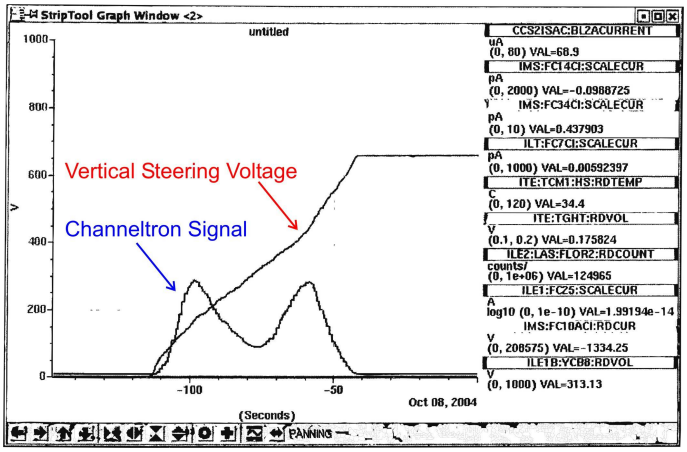

Figure 4.14. Channeltron signal and steerer voltage while tuning the beam across the vertical profile of the channeltron opening.

and the vertical steering voltage. After recording the profile, the beam is centered in the minimum position and the procedure is repeated with the horizontal steerers. Once the beam was centered in the region of the minimum count rate, we are sure that it will hit the hot spot of the carbon catcher. The target holder is moved horizontally back until the beam hits the carbon foil and the CO_2 laser is turned on again to heat the catcher.

4.2.5 Tracking of the Radioactive Ion Beams

Fluctuations of the radioactive lithium ion beam were tracked by detecting directly and/or indirectly the decay products. For that, a plastic scintillator and a NaI scintillator were used.

The plastic scintillator detector that was used during the ToPLiS experiment at TRIUMF is composed by a 5.5 cm long times 6.5 cm diameter (BC408) plastic and a photomultiplier tube (Phillips 4312/B) with a transistorized base (VD123K). In order to prevent the influences of magnetic fields, the photomultiplier is surrounded by 0.2 mm thick mu-metal[1]. The scintillator was able to detect the gamma-rays produced from the beta bremsstrahlung in the stainless steel chamber (on the order of one per decay), and neutrons. The detector's gain changed by less than 2 % at 100 KHz count rate.

In order to observe the β^--decay of the ^{11}Be daughter ($T_{1/2} = 13.81$ s) from ^{11}Li, a NaI detector was also used. This was because in principle characteristic gamma-rays could be gated. The detector itself is a 5 cm long times 5 cm diameter NaI from Bicron, and a commercial photomultiplier known to saturate at about 20 KHz rate.

Both detector signals were fed into level discriminators with thresholds set slightly

[1]Mu-metal is a nickel-iron alloy that is highly effective for shielding magnetic fields

higher than the natural background, and the pulses were sent to the data acquisition system. For the ^{11}Li run, the detectors were placed as close as possible to the vacuum chamber but still only subtended about 1 % solid angle, so the limited statistics from the ^{11}Li decay meant that there was no chance for gating in characteristic radiation and all events above the simple threshold were used.

4.2.6 Laser System and Stabilization Chain

For the resonance ionization of lithium using the excitation path described in section 3.3 two tunable continuous wave (cw) lasers were used. The 735 nm light was produced by a titanium sapphire (Ti:Sa) laser pumped with 15 W of an argon-ion laser (multi-line visible), while the 610 nm light was provided by a dye laser (Rhodamin 6G in Ethylenglycol) pumped with 6 W of a second argon ion laser (multi-line visible). The reference frequency for the isotope shift measurement was provided by an amplified diode laser system (Toptica, Model PDL 100) locked to an hyperfine component in the $X\,^1\Sigma_g^+ \rightarrow BO_u^+$ $R(114)$ 11-2 transition in molecular iodine by frequency modulation saturation spectroscopy [Ewa04]. The setup of the reference laser system is shown in Fig. 4.15. The light produced by the master laser and amplified in a broad area diode laser (BAL 740-100-1, Sacher) is cleaned with a grating from the small amount of amplified spontaneous emission (ASE) of the amplifier. The beam is split at the edge of a mirror into two components and each beam is sent through a single mode fiber (Newport S-FS-C) to obtain a good TEM-00 mode structure. The pump beam is frequency shifted (8 MHz) and amplitude modulated at 6.6 kHz with an acoustic optical modulator (AOM) in front of the fiber, while the probe beam

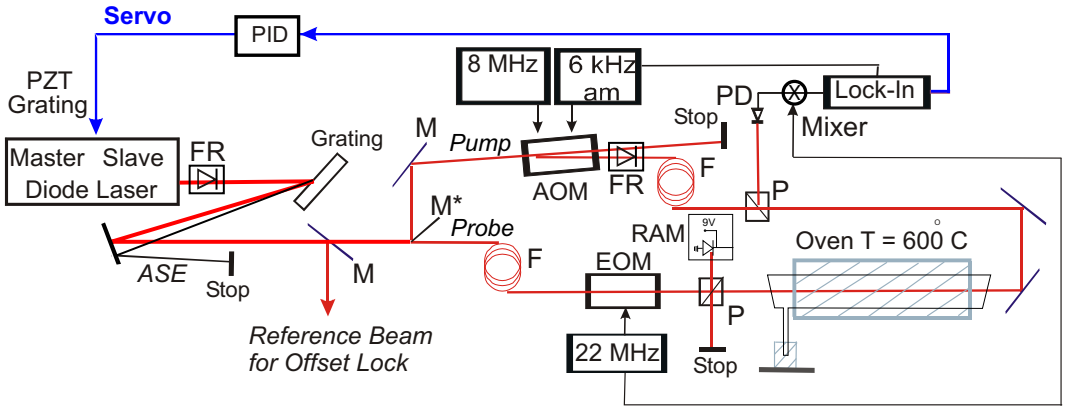

Figure 4.15. Setup for the reference laser system as described in the text. Abbreviations are: Faraday rotator (FR), amplified spontaneous emission (ASE), mirror (M), fiber (F), acoustic optical modulator (AOM), electro-optical modulator (EOM), polarizer (P), photodiode (PD), proportional integrated differential (PID) regulator, piezo (PZT) grating, and rest-amplitude-modulation (RAM).

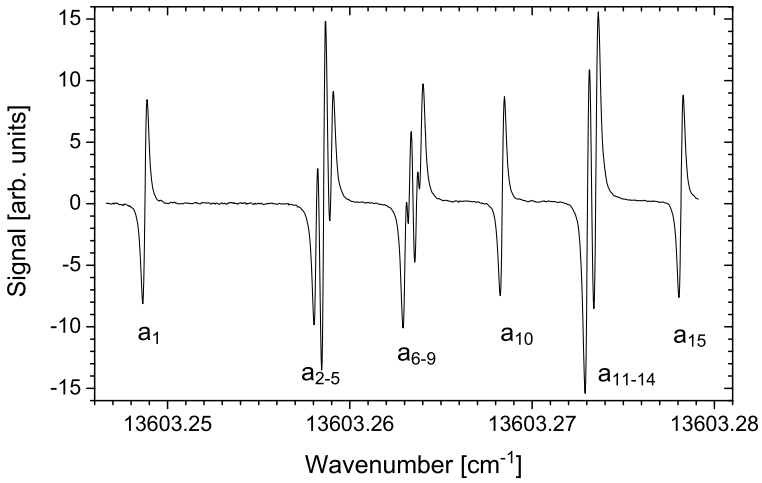

Figure 4.16. Hyperfine structure spectrum of the reference iodine line.

is frequency modulated (22 MHz) with an electro optical modulator (EOM) for side band generation after the fiber. Both beams are then superimposed in a counter-propagating geometry and with perpendicular polarization in an iodine cell (pump: 5 mW, probe: 3 mW, beam diameter 1 mm). To sufficiently populate the $\nu = 11$ vibrational level of the electronic ground state the cell is heated in an oven to 600 °C. The iodine reservoir is kept outside the oven in a cooling finger at a fixed temperature of 29°C to control the vapor pressure inside the cell. Pressure broadening of the lines was only observed at cooling finger temperatures clearly above 30°C, a pressure-dependent shift could not be observed at these temperatures [Ewa05]. After passing through the iodine cell, the probe beam is directed onto a photodiode. The obtained signal is amplified, demodulated with a mixer at the EOM frequency, and fed into a lock-in amplifier for phase-sensitive detection to extract the signal at the 6.6 kHz AOM chopping frequency. A typical spectrum is shown in Fig. 4.16. The a_1 hyperfine component is used for locking since it is clearly separated from the other components. The output of the lock-in amplifier is then used to produce a servo signal for the diode laser stabilization with a PID (Proportional, Integral, Differential) regulator.

The Ti:Sa laser is locked to the iodine laser via the frequency-offset locking technique. A small part of the diode laser beam is superimposed with a fraction of the Ti:Sa beam and the beat signal is observed with a fast photodiode (New Focus, Model 1434, 25 GHz). A two-way splitter is used to guide one part of the RF signal to a microwave frequency counter (HP, Model 5350B), while the second part is used for frequency-offset locking of the Ti:Sa laser. For this, the beat frequency is mixed with the RF-Output of a synthesized sweeper (Hewlett Packard, Model 83752A) and a frequency difference of exactly 160 MHz between the sweeper and the beat frequency is maintained. This is accomplished with

a frequency discriminator (MiTeq, Model FD-2PZ-160/10PC) that provides an output voltage proportional to the deviation of the input frequency from 160 MHz. Its output is fed into a PID regulator and the correction signal is applied to the external scan input of the Ti:Sa laser. By changing the RF frequency, the Ti:Sa laser can be set and stabilized to any arbitrary frequency around the reference line within the bandwidth of the fast photodiode. The laser linewidth can be estimated from the frequency spectrum of the beat signal. At GSI it was usually on the order of 1 MHz [Ewa05], while at TRIUMF a slightly larger linewidth of 2-3 MHz was observed. This increase was mainly due to the frequency jitter of the diode laser, caused by the acoustic noise of a CAMAC crate located nearby. However, with about 1 s integration time, the frequency measured by the frequency counter was stable to within a few 10 kHz.

The main part of the Ti:Sa laser light is transported from the TRINAT[2] laser laboratory to the experimental hall with a 25 meter long photonic-crystal fiber (Crystal Fibers, LMA-020) that can transmit high cw powers without significant losses and without indication of nonlinear Brioullin scattering [Rus03]. Typical transmission through the fiber was about 80% for 1 W input Ti:Sa laser power. The light is coupled into an optical enhancement cavity that is placed inside the vacuum chamber around the ionization region. The resonator has a length of approximately 30 cm and mirror curvature radius of 50 cm. The diameter of the TEM-00 mode in the focus is approximately 500 µm. One of the cavity mirrors is mounted on a piezoelectric transducer (PZT) for fine tuning of the cavity length. Collimating optics for the fiber, lenses for spatial mode-matching and sideband generation with an EOM required for the Pound-Drever-Hall locking [Dre83] is mounted on a breadboard above the vacuum chamber as shown in the photo in Fig. 4.17 [Ewa05]. Briefly, the locking technique can be described as follows: when the carrier is not exactly in resonance with the cavity, the two sidebands are reflected from the cavity with different intensities and phase shifts. In this case a beat signal between the carrier and the sidebands in the reflected light can be observed with a photodiode. The signal is demodulated at the EOM frequency and the result is fed into a PID regulator to generate a servo signal, which is then applied to the PZT to change the cavity length. Resonance enhancement of approximately 100 is observed, which provides sufficient excitation efficiency for the two-photon transition.

The dye laser light that drives the $2p \rightarrow 3d$ transition is transported from the laser laboratory to the experimental hall with a second photonic-crystal fiber of the same type. Transmission efficiencies of about 70% for up to 600 mW input dye laser power were achieved. This light must also be coupled into the optical resonator. In this case, the dye

[2]TRINAT stands for TRIUMF's Neutral Atom Trap.

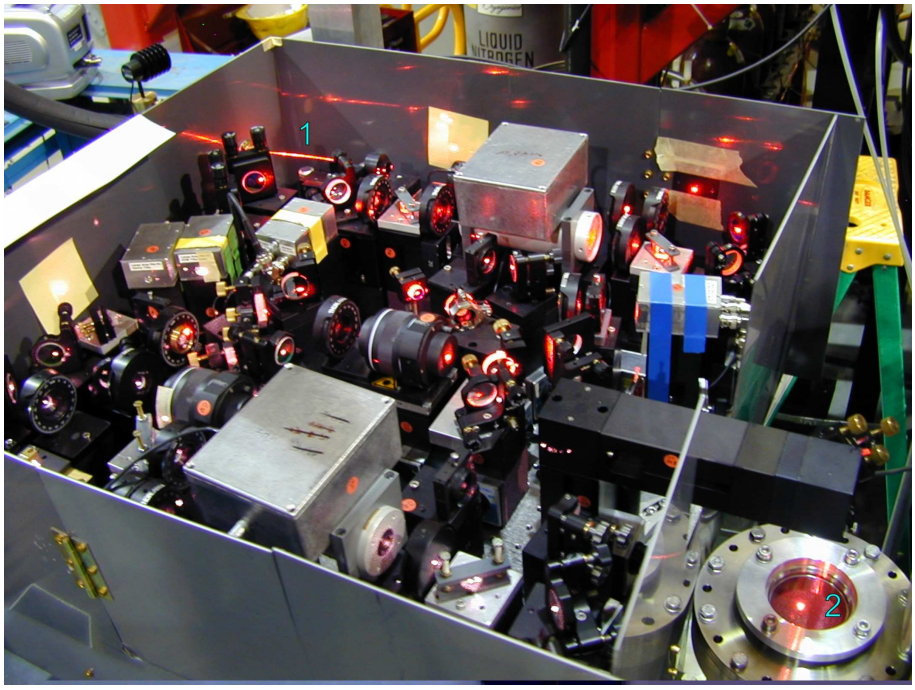

Figure 4.17. Foto of the optics used at ISAC for the stabilization of the optical resonator and dye laser. (1) Optical fiber for the dye laser light. (2) Entrance window of the vacuum chamber containing the optical resonator.

laser frequency is adjusted to match a longitudinal mode of the external resonator. This approach does not allow to tune the laser exactly to the $2p \rightarrow 3d$ resonance transitions, but since the high laser intensities cause a strong power broadening of the allowed dipole transition, this is not a serious disadvantage. With typical linewidths of 7 GHz (FWHM) and a free-spectral range of the optical resonator of 500 MHz it is always possible to find a locking point that provides maximum excitation efficiency. This point is further discussed in Chapter 5. More details of the laser setup are provided in [Ewa05].

4.3 Data Acquisition and Scanning Procedure

Data acquisition (DAQ) is based on the Multi-Branch System (MBS) developed at GSI. The MBS runs under the operating system Lynx OS (v2.5), a realtime UNIX system, on a CAMAC processor board CVC developed at GSI. The system works standalone, it reads all data from the CAMAC and writes it on a local tape drive; no other computers are necessary to take data and store it. For on-line analysis, however, workstations or personal computers are required. For the ToPLiS experiment, the data of each scan was transferred via a TCP/IP connection (Transmission Control Protocol / Internet Protocol) into the data analysis package Origin 7.0, running on a PC. C++ routines written in the

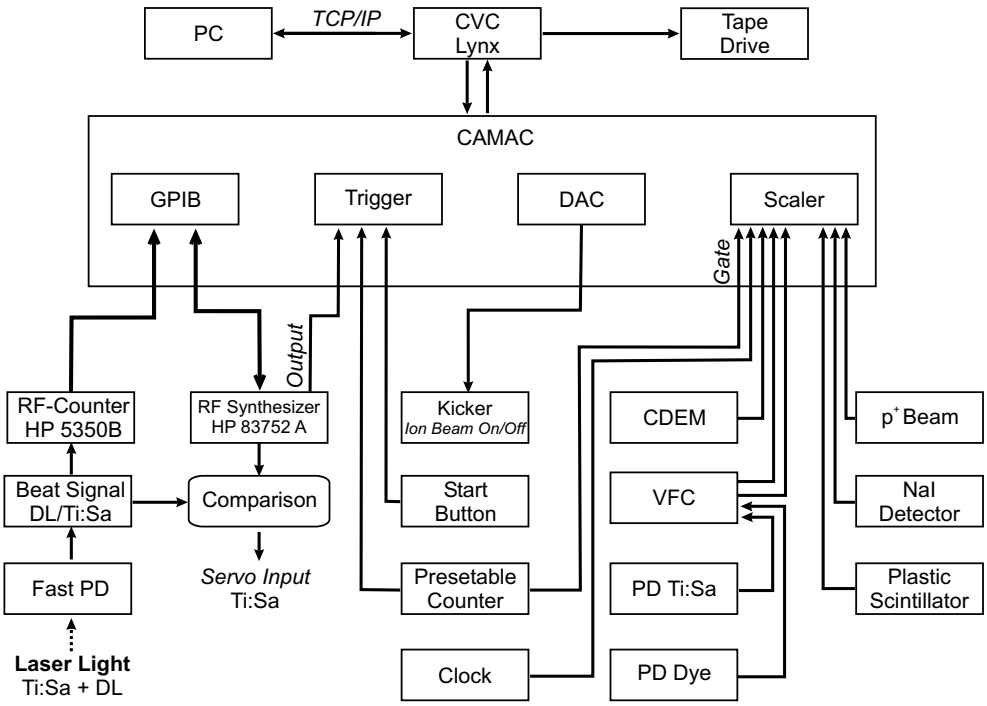

Figure 4.18. Schematic representation of the most relevant CAMAC crate hardware components and their connections to the experimental setup. Abbreviations are explained in the text.

Origin environment where finally used to analyze the data.

Adaption of the MBS system to the ToPLiS experiment was performed by programming the master readout task (m_read_meb) which runs on the CVC node and is called whenever a trigger bit in the GSI trigger module is polled. It reads the local crate and controls all hardware devices. The CAMAC crate is equipped with a number of modules which schematically are shown in Fig. 4.18. A CAMAC-GPIB (General Purpose interface Bus) controller allows communication with the RF synthesizer and the microwave counter, a Digital-to Analog Converter (DAC) is used, amongst others, to turn the ion beam on and off, while count rates and voltages are recorded with two Scalers and an Analog-to-Digital Converter (ADC), respectively.

The scaler receives the signal from the different monitoring devices, *e.g.*, the Continuous Dynode Electron Multiplier (CDEM), the photodiodes (PD) for the Ti:Sa and dye lasers, a clock, the proton beam current and the gamma and neutron detectors. The signals from the photodiodes were first converted into a frequency via a voltage to frequency converter (VFC) [Ewa05]. The beat signal between the Diode Laser (DL) and the Ti:Sa laser is split and send to the RF-counter and the frequency-offset-lock electronics.

A scan across the hyperfine structure components of a lithium isotope is performed in the following way: the Ti:Sa and dye lasers are set to the desired frequencies and the

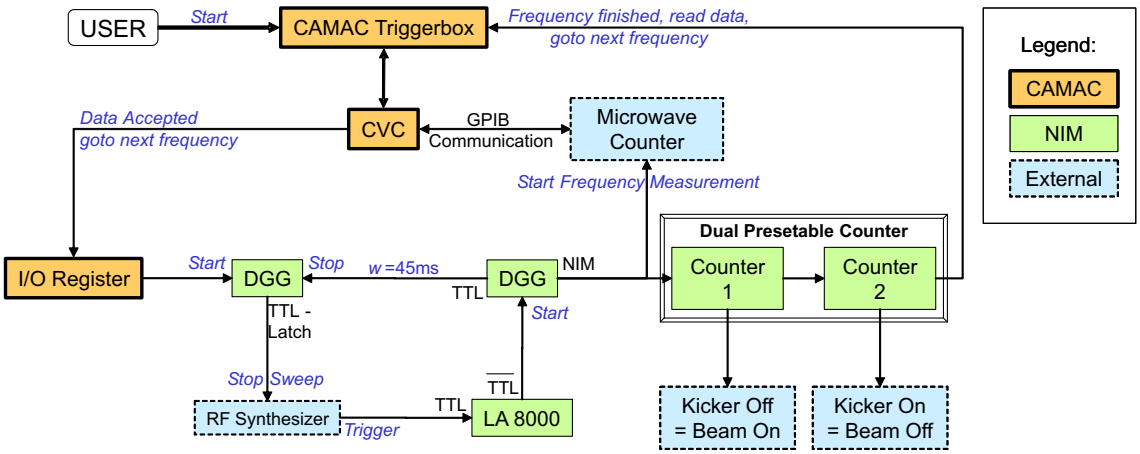

Figure 4.19. Data acquisition control of the laser frequency and the ion beam.

full stabilization chain is locked. A dual presetable counter is used to define two time periods: one during which the ion beam is turned on (1 s for the stable isotopes, 10 s for the short-lived isotopes), and a second one with the ion beam turned off (stable isotopes: 0 s, ^{8}Li: 5 s, ^{9,11}Li: 1 s). The duration of the second period exceeds 5 half-lifes of the respective isotope and serves to make sure that signals from radioactive decay of ions implanted in the CDEM detector at one frequency are not recorded in the next frequency channel. The two presetable counters are arranged in a way that finishing the first time period triggers the start of the second counter. The gates from the counters are sent to the fast kicker to control the ion beam and are also used to gate the two CAMAC scalers. This allows to distinguish between events that happen while the ion beam is on and those during the beam-off time. While, for instance, the laser intensity is only relevant during the time in which resonance ions are created (beam-on) the information from the beam normalization detectors during beam-off times can be used for background correction. Detection events from the channeltron detector during the beam-off time, resulting from α-decays are added to the resonance signal. During the two time intervals the scaler and ADCs are read once a second and the data is written on tape. With this information the time behavior of a signal can also be resolved at least with limited resolution.

After finishing one beam-on - beam-off cycle, the scalers are cleared and the next frequency is set. This is performed using the "Trigger" output and the "Stop Sweep" input of the RF synthesizer as shown in Fig. 4.19. If data recording for one frequency is finished, the CVC creates a signal at an I/O register that latches a Digital Gate Generator (LeCroy Model DGG 222) and its output is fed into the Stop-Sweep input of the RF synthesizer. While the scan was hold before, pulling the input high continues the scan. The sweeper range is divided into intervals and at the end of each interval a TTL signal

appears at the Trigger output. This TTL is used to end the latch of the DGG, the RF synthesizer holds, and the first of the presetable counters is started. The same signal also starts the microwave counter to integrate the beat signal of the frequency-offset lock over a period of 1 s.

Data were recorded at 1 MHz steps over ±15 MHz about the resonance positions, skipping the long region between the two peaks[3]. When the scan is completed, the RF synthesizer returns to the starting frequency. Since the software of the generator does not allow a continuous sweep backwards, the frequency was set back in a single step which usually caused the stabilization chain to fall out of lock. However, this was not a serious interruption, since relocking is typically performed within a few seconds and the next scan could be started. The isotopes ^{6,8}Li exhibit a relatively small hyperfine structure splitting. Hence, the scan covers only a small frequency range and the stabilization chain often stayed locked when the frequency was reset and the next scan could be performed immediately. This was one of the reasons that the isotope ^{6}Li was chosen as the reference for the isotope shift measurements, despite the fact that ^{7}Li is used as the reference for the charge radius (see Chapter 2).

Whenever the stabilization of the cavity or the dye laser fell out of lock during the scan, or the ion beam stopped due to a breakdown of the cyclotron, an alarm was started and the scan was stopped. This allowed continuation of the scan after relocking the cavity or laser or when the proton beam was back. In such a case, only the channel in which the dropout occurred was lost and had to be removed in the data analysis.

[3]This is referred to as "skip-steps scans" in what follows.

5 Experimental Results

The ToPLiS collaboration requested two beam times at the ISAC facility. A first beam time of 10 shifts[1] was devoted for remeasuring ^{8,9}Li, which were previously measured at GSI in 2003 [Ewa04, Ewa05], but this time with much higher production yields and better statistics. This run was also used for a careful investigation of systematic frequency shifts. A second beam time of 20 shifts was mainly required for measuring the isotope shift of the halo nucleus ^{11}Li. Both were approved under the experiment number E991 and the results are summarized in this chapter.

5.1 Measurements of the Stable Isotopes - Lithium-6 and -7

5.1.1 Resonance Profiles

Figure 5.1 shows spectra recorded for the $2s \rightarrow 3s$ transition in ^{6}Li and ^{7}Li using the measurement procedure described in Section 4.3. The incoming ion yield from the Off-Line Isotope Separator (OLIS) was about 2×10^8 ions/s and 5×10^7 ions/s for ^{6}Li and ^{7}Li respectively[2]. For each channel the observed number of events (N_{Raw}) were normalized with the Ti:Sa laser power signal ($P_{\mathrm{Ti:Sa}}$) that was recorded with the photodiode located after the enhancement cavity (see Fig. 4.1).

$$N_{\mathrm{Norm}} = N_{\mathrm{Raw}} \times \left(\frac{P_{\mathrm{Ti:Sa}}}{\langle P_{\mathrm{Ti:Sa}} \rangle} \right)^{-2}, \tag{5.1}$$

where $\langle P_{\mathrm{Ti:Sa}} \rangle$ is the average Ti:Sa laser power while recording the spectrum. The uncertainty of N_{Norm} was calculated from the statistical uncertainty and from the laser power fluctuations using Gaussian error propagation. The spectrum was fitted with the lineshape function discussed in Section 3.2 applying a Levenberg-Marquardt minimization procedure. Lorentzian and Gaussian linewidths of the Voigt profile are constraint to be equal for both hyperfine structure components. The Doppler background width was fixed to be 1.7 GHz as observed in previous measurements of stable isotopes [Ewa05]. Tests with the fitting program showed that this parameter can vary over a large range without affecting the resonance position. Typical observed linewidths of the Voigt pro-

[1] 1 shift = 12 hours

[2] The intensities do not reflect the natural isotopic abundance since spectra were taken with different settings at the ion source.

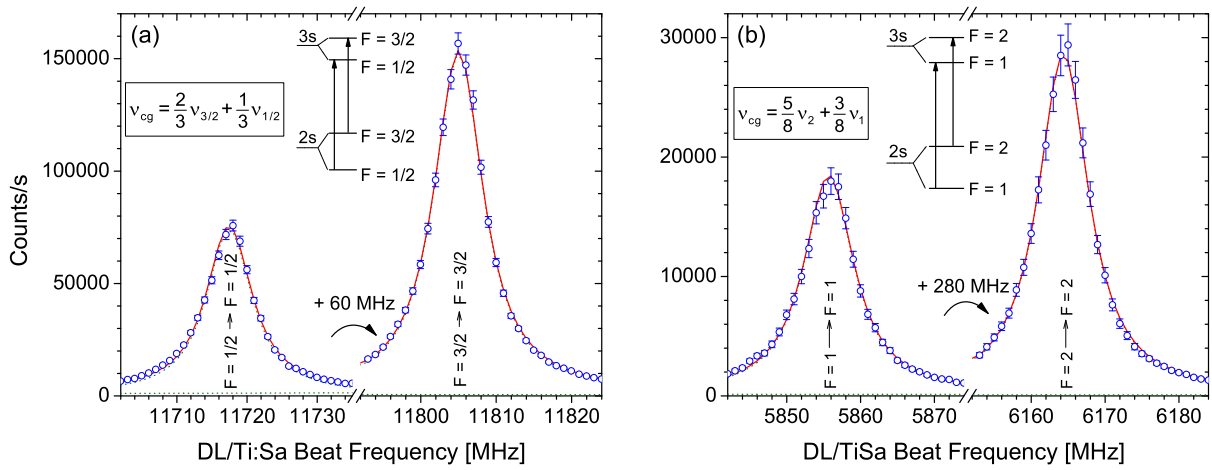

Figure 5.1. Typical resonance-ionization spectra recorded for ^{6}Li (a) and ^{7}Li (b). The horizontal-axis is the beat frequency between the reference diode laser (ν_{DL}) and the Ti:Sa laser ($\nu_{Ti:Sa}$), where $\nu_{Ti:Sa} < \nu_{DL}$. "Skip-steps scans" were used during the beam times and the size of the skipped frequency range is indicated at the breaks. Once the data were normalized against the Ti:Sa laser power (blue circles) they were fitted with the line profile discussed in section 3.2. Dotted green lines show the individual peak function while the solid red line is the overall fitting function.

files are 3 MHz for the Lorentzian and 1-3 MHz for the Gaussian components (see Section 5.1.2). The overall fitting function, represented by the solid red line in Fig. 5.1, fits excellent to all data points. The center-of-gravity (cg) of the transition was calculated with the formulas given in Table 2.10, from which, $\nu_{cg}(^6\text{Li}) = 11775.823(20)$ MHz and $\nu_{cg}(^7\text{Li}) = 6048.610(27)$ MHz were obtained. To correct systematic light shift, measurements at various Ti:Sa laser powers were performed. Results of such measurements for ^{6}Li and ^{7}Li are shown in Fig. 5.2. The center-of-gravity frequency is plotted against the average Ti:Sa laser power $\langle P_{\text{Ti:Sa}} \rangle$ and a linear behavior is observed:

$$\nu_{cg} = b_{0\,\text{Ti:Sa}} + b_{1\,\text{Ti:Sa}} \langle P_{\text{Ti:Sa}} \rangle \ . \tag{5.2}$$

For these examples $b_{0\,\text{Ti:Sa}} = 11777.542(25)$ MHz and $b_{1\,\text{Ti:Sa}} = -0.0549(14)$ MHz/mW for ^{6}Li, and $b_{0\,\text{Ti:Sa}} = 6050.507(42)$ MHz and $b_{1\,\text{Ti:Sa}} = -0.0574(20)$ MHz/mW for ^{7}Li respectively, where the uncertainties are at the 95 % confidence limit.

It should be noted that the AC-Stark shift slope coefficients $b_{1\,\text{Ti:Sa}}$ do not agree within their respective uncertainties. This is different to the behavior observed in measurements at GSI, where agreement for ^{6,7,8}Li was found. The effect has no consequences for ^{6,7,8,9}Li isotope shifts determined via extrapolation to zero laser power but may severely influence ^{11}Li measurements. This will be discussed and analyzed in Section 5.4.

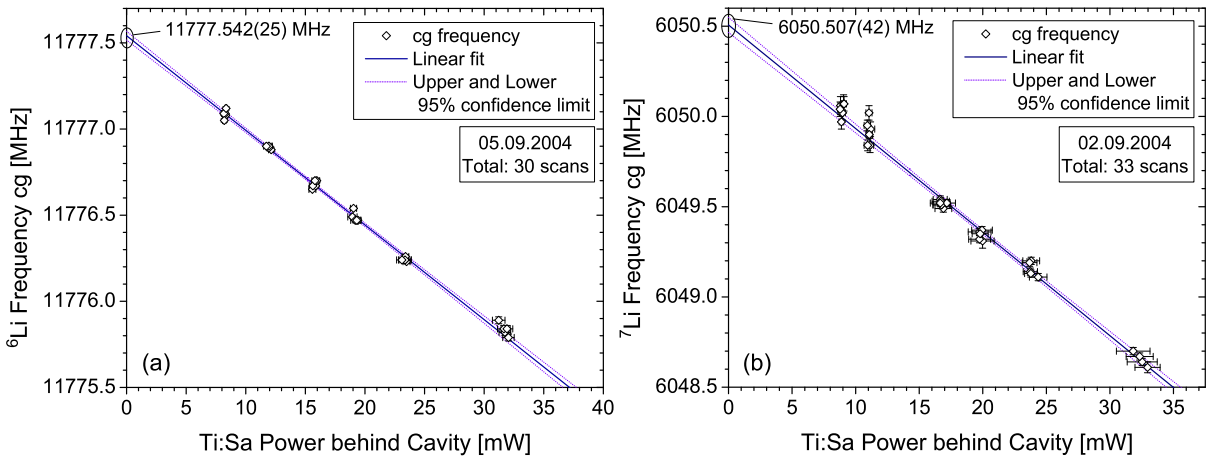

Figure 5.2. AC-Stark Shift in ^{6}Li (a) and ^{7}Li (b). The open black diamonds represent the center-of-gravity frequency for each scan. The solid blue lines are linear fits to the data points weighted with their respective uncertainties, and the dotted violet lines give the 95% confidence interval of the fit.

5.1.2 Saturation and Linewidth

High intensities of the Ti:Sa laser inside the optical resonator causes saturation and thus line broadening. This effect was studied by measuring the Lorentzian linewidth Γ_L of the narrow Voigt profiles in ^{6}Li . Figure 5.3 shows the result as a function of the Ti:Sa laser intensity inside the cavity $\langle I_{\mathrm{Ti:Sa}} \rangle$. The intensity was calculated from the transmitted power with a measured cavity mirror transmission of 0.05 % and a calculated cavity mode diameter of 0.46 mm. The solid red line, is a fit of the function for the power broadened

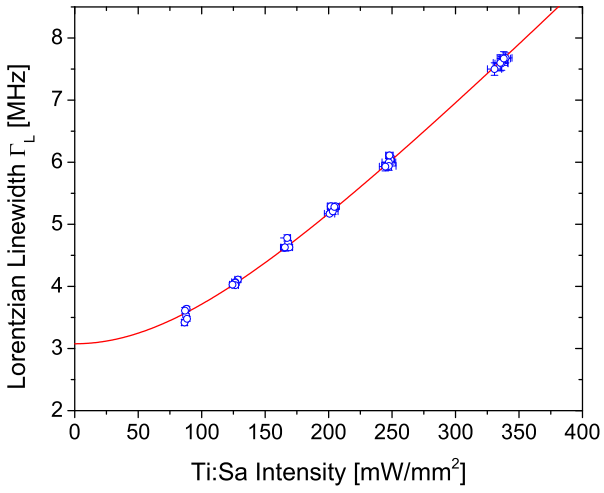

Figure 5.3. Linewidth of ^{6}Li as a function of the Ti:Sa laser intensity.

linewidth of a two-photon transition

$$\Gamma_L = \Gamma_0 \sqrt{1 + \left(\langle I_{\text{Ti:Sa}} \rangle / I_{\text{Sat}}\right)^2} \tag{5.3}$$

to the data points where $\Gamma_0 = 3.08(2)$ MHz is the unsaturated linewidth and $I_{\text{Sat}} = 148(2)$ W/mm^2. These results are in good agreement with the previously determined values in [Ewa05]. The natural linewidth of the transition is $\Gamma_{0\,\text{nat}} = 2.65$ MHz. The small deviation is either caused by laser intensity fluctuations inside the cavity causing a varying AC-Stark shift for all atoms or an artefact from the fit program having trouble to distinguish between homogeneous and inhomogeneous widths.

5.1.3 Line Shape of the $2p \rightarrow 3d$ Transition

The change in the Ti:Sa laser frequency during a scan induces a change of the dye laser frequency because both lasers are coupled to longitudinal modes of the same optical resonator. Since the Ti:Sa is tuned across the $2s \rightarrow 3s$ transition, the dye laser can not match exactly the $2p \rightarrow 3d$ transition frequency, but this does not cause a difficulty because of strong power broadening in this transition. The lineshape of the $2p \rightarrow 3d$ transition was studied to find maximum excitation efficiency and to ensure a constant ionization efficiency along the whole scan. The QMS was set to detect laser ions of ^{6}Li, the Ti:Sa laser was locked in resonance position of the $F = 3/2 \rightarrow F = 3/2$ transition. Then the frequency of the dye laser was changed manually until a longitudinal mode of the cavity was reached. There, the dye laser was stabilized to the cavity and resonant laser ions were detected for a period of 3 s, before the dye laser frequency was changed to the next cavity mode. The free spectral range of the cavity is approximately 500

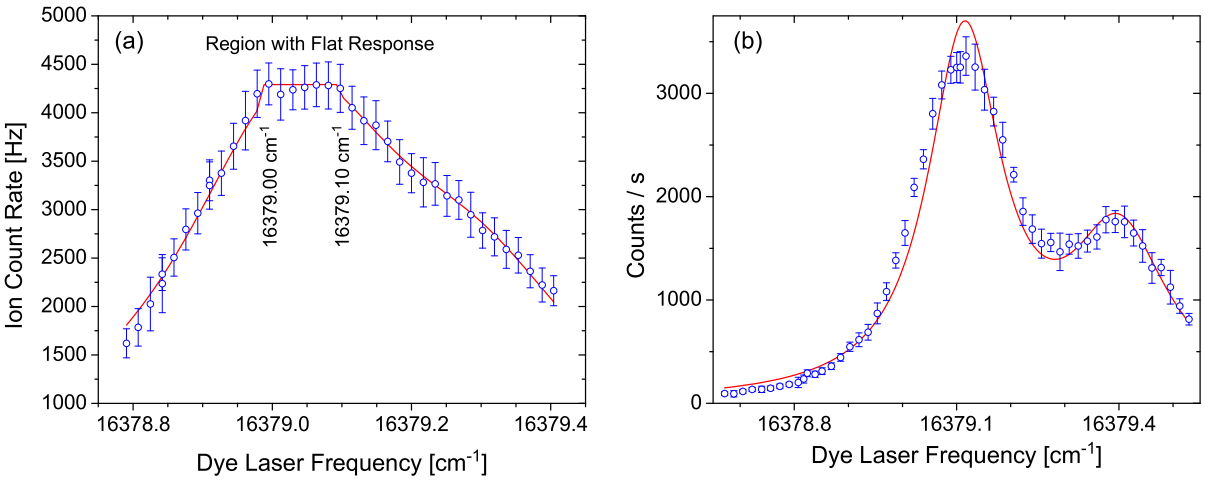

Figure 5.4. (a) 2p → 3d transition in ^{6}Li. The solid red line serves only to guide the eye. (b) 2p → 3d transition in ^{7}Li from [Ewa05].

MHz, which determined the step size. Figure 5.4(a) shows the detected ion count rate (open blue points) as a function of the dye laser frequency, measured with an ATOS wavemeter. This spectrum was taken with the Ti:Sa laser intensity reduced to 25 % of the maxima achievable power. The profile shows a large flat region of about 0.1 cm^{-1} (3 GHz) width, ideal for looking the dye laser during a scan. The dye laser power is sufficient to overlap not only the $2p\,^2P_{3/2} \rightarrow 3d\,^2D_{3/2,5/2}$ components but also the $2p\,^2P_{1/2} \rightarrow 3d\,^2D_{3/2,5/2}$ transition. This was not possible in measurements at GSI where less dye laser power was available. Figure 5.4(b) shows spectra taken at GSI for comparison, where the $2p\,^2P_{1/2} \rightarrow 3d\,^2D_{3/2}$ transition was still clearly resolved. Thus, the overall efficiency should be increased by about 30 % compared to the GSI measurement since the laser will also excite and ionize the fraction of atoms decaying from the $3s\,^2S_{1/2}$ to the $2p\,^2P_{1/2}$ state.

5.2 Measurements of Lithium-8

Figure 5.5 shows a typical spectrum for ^{8}Li with a target/ion source extraction voltage of 30 kV recorded during the October 2004 beamtime. Incoming yields were about 10^9 ions/s. For each channel the raw data (N_{Raw}) were normalized for lithium ion-beam current fluctuation using the plastic scintillator signal, N_γ, and for Ti:Sa laser power fluctuations with the photodiode signal, $P_{\mathrm{Ti:Sa}}$, according to

$$N_{\mathrm{Norm}} = N_{\mathrm{Raw}} \times \left(\frac{N_\gamma}{\langle N_\gamma \rangle}\right)^{-1} \times \left(\frac{P_{\mathrm{Ti:Sa}}}{\langle P_{\mathrm{Ti:Sa}} \rangle}\right)^{-2}. \tag{5.4}$$

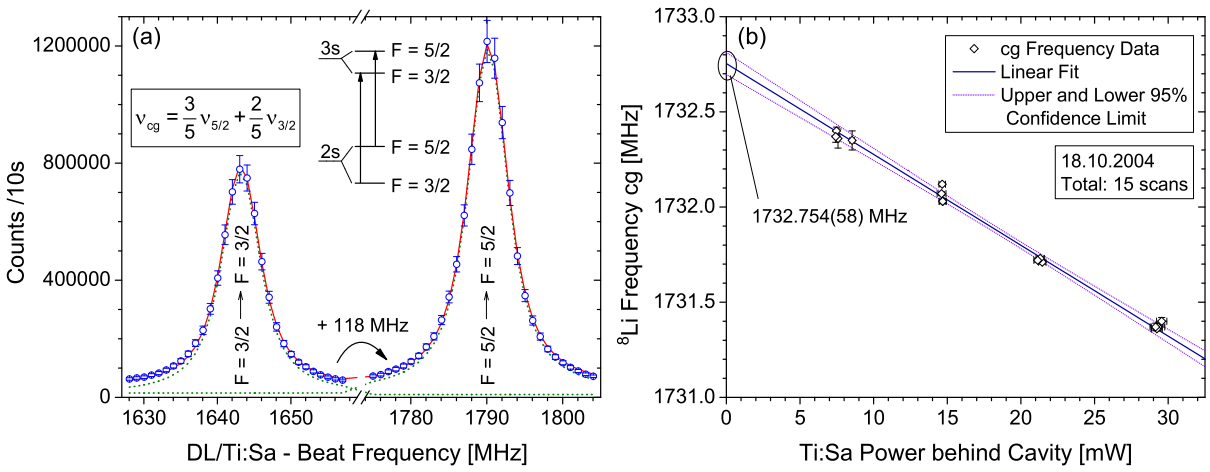

Figure 5.5. (a) Spectrum recorded for ^{8}Li during the October 2004 beamtime, $\nu_{\mathrm{Ti:Sa}} < \nu_{\mathrm{DL}}$. (b) AC-Stark shift effect with linear fit and 95 % confidence interval.

$\langle N_\gamma \rangle$ and $\langle P_{\text{Ti:Sa}} \rangle$ are the averaged gamma intensity and Ti:Sa laser power while recording the spectrum. A correction of the γ-ray-background was not necessary since the count rate with ion-beam on was orders of magnitude larger than the dark-background with the ion-beam turned off. Once the data were fitted, the center-of-gravity of the transition was extracted using the equation given in Table 2.10. Similar as for ^{6}Li and ^{7}Li the data obtained needed to be corrected for systematic light shift effects. Therefore several spectra were taken at different Ti:Sa laser powers. Figure 5.5(b) shows the linear dependence of the center-of-gravity frequency on the averaged Ti:Sa laser power. By fitting (5.2) to ν_{cg} data the coefficients values of $b_{0\,\text{Ti:Sa}} = 1732.754(58)$ MHz and $b_{1\,\text{Ti:Sa}} = -0.0477(29)$ MHz/mW were obtained.

5.3 Measurements of Lithium-9

With typical production ^{9}Li yields of $10^7 - 10^8$ ions/s at TRIUMF, signal count rates as high as 120 kHz were observed and the AC-Stark shift could be studied systematically in a similar way as for the other isotopes. A typical spectrum is shown in Fig. 5.6(a) and the AC-Stark shift in Fig. 5.6(b). Note that the order of the hyperfine components is now reversed and the slope of the AC-Stark shift line is positive since the Ti:Sa frequency is now higher than the reference-laser frequency and an increasing beat signal therefore corresponds to an increase in Ti:Sa-laser frequency. From the linear fit (5.2), a slope coefficient of $b_{1\,\text{Ti:Sa}} = 0.0466(7)$ MHz/mW and an intercept of $b_{0\,\text{Ti:Sa}} = 1615.982(16)$ MHz was obtained for this data set.

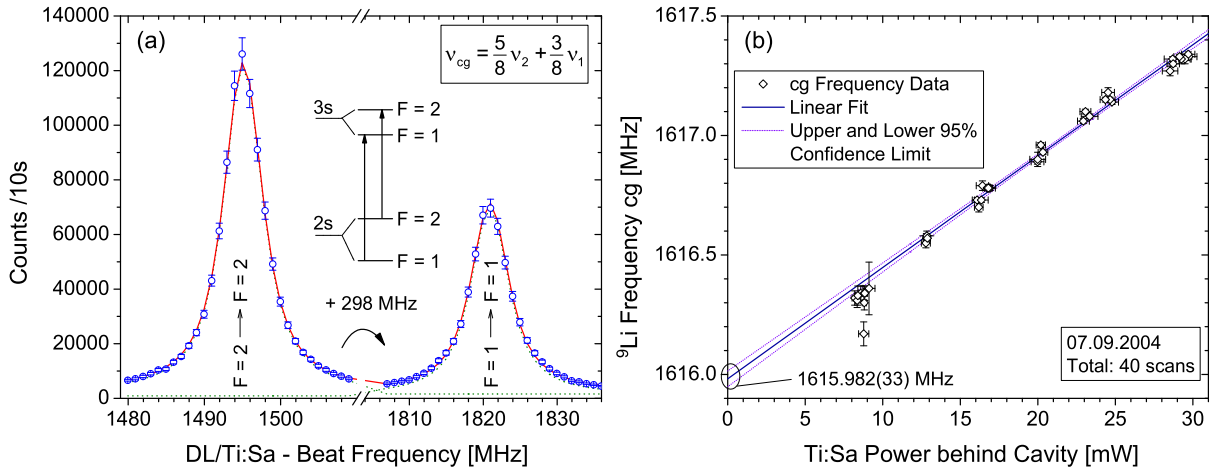

Figure 5.6. Typical spectrum (a) and AC-Stark Shift (b) for ^{9}Li observed during the October 2004 beamtime, $\nu_{\text{Ti:Sa}} > \nu_{\text{DL}}$.

5.4 Systematic Effects of the Light Field

5.4.1 Ti:Sa Laser AC-Stark Shift

The production rates of ^{8,9}Li at ISAC allowed a variation of the laser power over a large range and thus an extrapolation to zero laser intensity. This approach is not feasible for ^{11}Li because the production rates are four orders of magnitude smaller than for ^{9}Li and the count rate at reduced laser power will be clearly below 1 Hz. An alternative approach is to perform measurements only with full laser power and to calculate the isotope shift by comparison with the ^{6}Li center-of-gravity frequency at the same laser power. To avoid systematic errors, it must be ensured that all isotopes react in the same way to the light field, *i.e.*, that the slope of the AC-Stark shift line is equal for all isotopes. Previous measurements at GSI [Ewa05] showed that the slope coefficients for ^{6,7,8}Li agreed within their uncertainty of approximately 2 kHz/mW, while the production rate for ^{9}Li at GSI was too small for such a measurement. Hence, ^{9}Li measurements at GSI were only performed at highest laser intensities and the uncertainty of the isotope shift was limited by the systematic uncertainty. At TRIUMF, however, the AC-Stark shift showed a larger fluctuation as already mentioned previously.

On the left part of Fig. 5.7(a) the slope coefficients obtained for ^{6,7,8,9}Li during the September beamtime are shown. The straight lines fitted to the different sets serve just to guide the eye. It can be clearly seen that there is a systematic trend: the heavier the isotope the steeper the AC-Stark shift. This seemed to indicate a mass-dependent effect which could be caused by the different velocities of the atoms. A hypothesis that

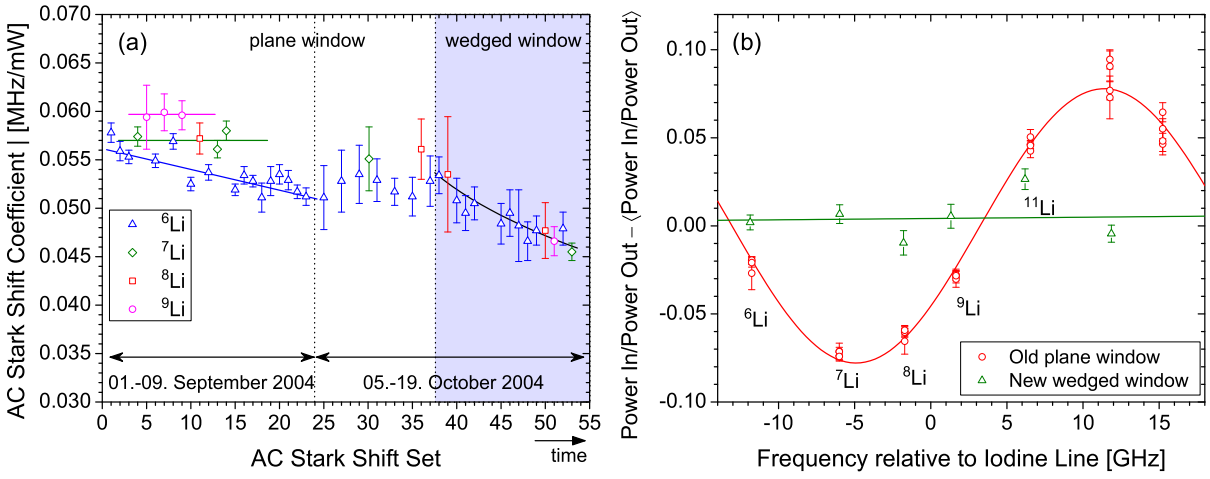

Figure 5.7. (a) AC-Stark Coefficients $b_{1\,\mathrm{Ti:Sa}}$ for all isotopes and measurements obtained during the two beamtimes in September and October 2004. (b) Etalon effect of the exit window as discussed in the text.

was checked by measuring the AC-Stark shift of ^{6}Li at different catcher temperatures by varying the CO_2 laser power. However a systematic effect could be not be observed, the slope coefficients all agreed within their uncertainties.

Another possibility for such a change in the slope could be that the laser intensity inside the cavity was not proportional to the recorded light power on the photodiode. The light has to pass the high reflector of the cavity and the bottom viewport of the vacuum chamber before it hits the photodiode. An etalon effect in either of these components would result in a frequency and, hence, isotope dependent variation of the recorded power at identical laser intensities inside the cavity.

To test this hypothesis a test measurement was performed: a part of the incident Ti:Sa laser beam was directed to a photodiode in front of the enhancement cavity, while the transmitted laser power was measured with the photodiode located behind the cavity. In Fig. 5.7(b) the variation of the ratio between the input and the output power is plotted against the Ti:Sa laser frequency (red circles). Particulary, those points where the lithium resonances appear were chosen. It is obvious that the ratio depends on the frequency. The measurement shows a variation of ± 8 % in the light power, which can be translated into a change in the slope coefficient $b_{1\,\mathrm{Ti:Sa}}$ of approximately ± 4 kHz/mW and is in good agreement with the isotope-dependent effect observable in Fig. 5.7(a). The solid red line is a sinus function fitted to the data points to guide the eye and to give a crude estimation of the free spectral range (FSR) which was found to be on the order of 30 GHz.

For an etalon with thickness d, refractive index of the medium n ($n = 1.4$ for glass), and orthogonal incidence of the light, the free spectral range is given by $(\Delta\nu)_{\mathrm{FSR}} \approx c/2nd \approx 30$ GHz, where c is the speed of light. Thus the object must have a thickness of $d \approx 3$ mm, which is about the thickness of the plane bottom window of the chamber.

The window was replaced by a new wedged window and the test measurement was repeated. The result is included in Fig. 5.7(b) (green triangles) and does not show a clear signature of a systematic effect anymore. The data points have a standard deviation of 1.1 % around the average power, the largest deviation is 2.5 %. This corresponds to an effect of 0.5 kHz/mW and is smaller than the typical statistic uncertainty in the determination of the $b_{1\,\mathrm{Ti:Sa}}$ coefficient. The summary of the data analysis during the October 2004 beamtime, as depicted in the right part of Fig. 5.7(b), showed that after the replacement of the window, the coefficients of the AC-Stark shift effect did not show an isotopic dependence and only a small drift and scatter are present. The reason for the residual drift is not completely understood but may be ascribed to degradation of the cavity mirrors.

5.4.2 Dye Laser AC-Stark Shift

The variation of the dye laser intensity produces also a change in the resonance frequencies and was studied as well during the two beamtimes. Figure 5.8 shows the ^{6}Li center-of-gravity frequency as a function of the dye laser power. Similar as for the Ti:Sa laser, the leaking dye laser light from the cavity was recorded using a photodiode located behind the optical resonator.

Data in Fig. 5.8(a) were obtained by keeping the Ti:Sa laser power approximately constant and varying only the dye laser power. The center-of-gravity resonance frequencies were corrected to take into account the AC-Stark shift effect produced by the Ti:Sa laser using, $\nu_{\mathrm{cg}}^{\mathrm{corr}} = \nu_{\mathrm{cg}} - b_{1\,\mathrm{Ti:Sa}} P_{\mathrm{Ti:Sa}}$, where $b_{1\,\mathrm{Ti:Sa}} = -0.0505(8)$ MHz/mW is the Ti:Sa-AC-Stark slope coefficient which was obtained from the ^{6}Li AC-Stark-shift reference measurement closest in time. From the linear fit

$$\nu_{\mathrm{cg}}^{\mathrm{corr}} = b_{0\,\mathrm{dye}} + b_{1\,\mathrm{dye}} \langle P_{\mathrm{dye}} \rangle \ , \tag{5.5}$$

the values of $b_{0\,\mathrm{dye}} = 11\,777.373(35)$ MHz and $b_{1\,\mathrm{dye}} = 0.115(25)$ MHz/mW were obtained, where the uncertainties are at the 2σ level.

In a second measurement a different procedure was used. Three different dye laser powers were chosen and for each power a complete AC-Stark shift measurement for the Ti:Sa laser was performed. The extrapolated values for vanishing Ti:Sa power are shown in Fig. 5.8(b) and a linear fit, $\nu_{\mathrm{cg}} = b_{0\,\mathrm{dye}} + b_{1\,\mathrm{dye}} \langle P_{\mathrm{dye}} \rangle$, is now used to extrapolate also to zero dye intensity, where $b_{0\,\mathrm{dye}} = 11\,777.404$ MHz and $b_{1\,\mathrm{dye}} = 0.089$ MHz/mW. At 1σ level

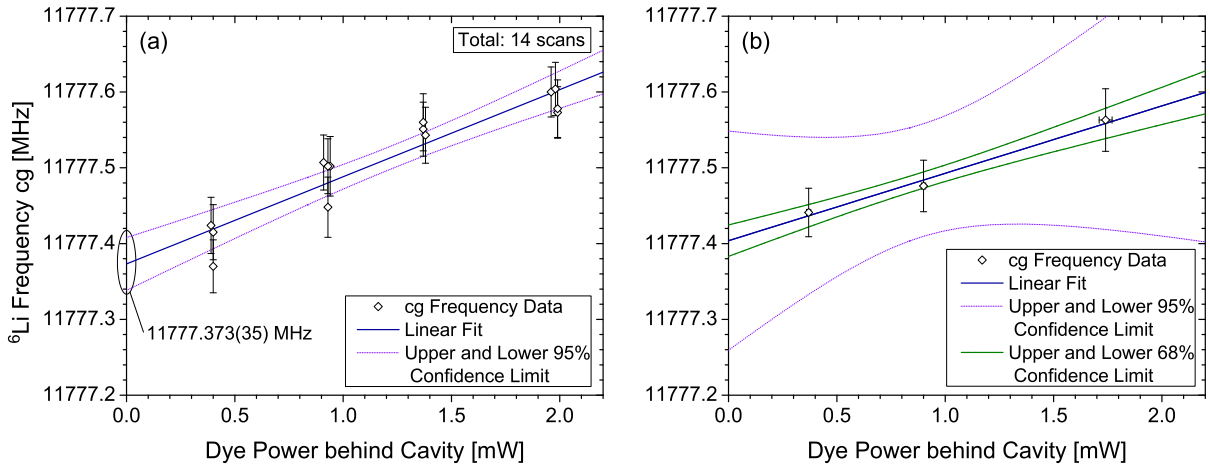

Figure 5.8. AC-Stark shift effect in ^{6}Li produced by the dye laser. (a) The Ti:Sa laser intensity was kept constant while taking the dye AC-Stark shift measurements, later the data were corrected for the Ti:Sa laser power as explained in the text. (b) Every point represents the extrapolated value to zero Ti:Sa laser intensity of a complete Ti:Sa AC-Stark shift measurement.

(68 % confidence limit), the uncertainties are $\Delta(b_{0\,\mathrm{dye}}) = 0.021$ MHz and $\Delta(b_{1\,\mathrm{dye}}) = 0.020$ MHz/mW respectively, while at 2σ level (95 % confidence limit) they are $\Delta(b_{0\,\mathrm{dye}}) = 0.145$ MHz and $\Delta(b_{1\,\mathrm{dye}}) = 0.139$ MHz/mW. It is obvious that the fit to only three data points will result in a large uncertainty at the 95 % confidence level. The results of both measurements show god agreement.

5.5 Measurements of Lithium-11

5.5.1 Background of Beryllium-11

An open question concerning the ^{11}Li detection was whether the β-decay of the ^{11}Be daughter would trigger additional channeltron events as it is the case for the α-particles created in the ^{8,9}Li decay. If this is the case, the 13.6 s half-life of ^{11}Be would require a beam-off time of about 1 min after each frequency step, at least after those channels with a considerable number of events. To check the response of the channeltron on the β-decay of ^{11}Be the following measurement was performed: the quadrupole mass spectrometer was set to detect ^{11}Li laser ions, the Ti:Sa laser was locked on the ^{11}Li $F = 2 \rightarrow F = 2$ resonance transition, the dye laser was also locked for resonance ionization, and ^{11}Li laser ions were detected over a period of 200 seconds with the channeltron detector. The ^{11}Li ion-beam was then turned off and subsequent events were recorded. The result is shown in Fig. 5.9. Overall 234 ^{11}Li events were detected during the beam-on period, while within 100 seconds after turning off the ion-beam no further event was recorded. Such a measurement was repeated several times but an indication for a detection of ^{11}Be decays was never observed. The 2α channel contributes only to 2 % to the ^{11}Be decay and

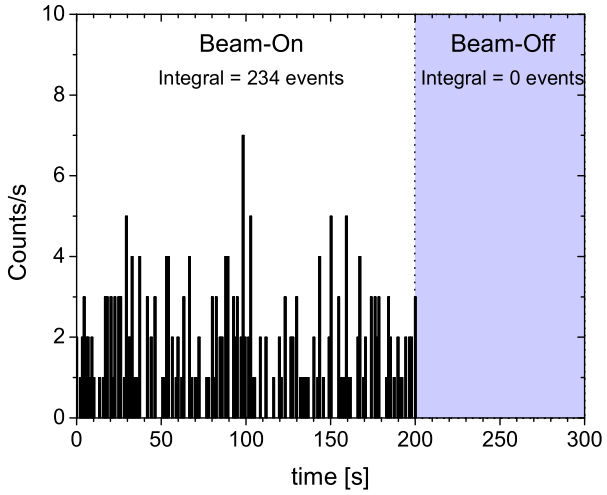

Figure 5.9. Search for events caused bye the decay of the ^{11}Li daughter ^{11}Be inside the channeltron as described in the text.

channeltron events caused by this decay chain can be neglected. Thus, the ion beam-off time between two frequency channels was always set to 1 s for ^{11}Li.

5.5.2 Production Rates for Lithium-11

Figure 5.10(a) shows the gamma events detected with the plastic scintillator detector during the ^{11}Li runs. The almost constant average rate of 300 counts/10s that was observed during 6 days corresponds to a ^{11}Li yield of about 30 000-35 000 ions/s, as measured with the small channeltron detector used for the alignment of ^{11}Li ion-beam (see Section 4.2.4.2). The rise around measurement number 40 was caused by a realignment of the mass separator and optimization of the QMS ion optics and channeltron voltages.

5.5.3 Spectra for Lithium-11

To record spectra of ^{11}Li, the acquisition time per frequency channel with ion-beam was set to 10 s as in the case of ^{8,9}Li. The beam-off time was chosen to be 1s, which is much longer than five times the ^{11}Li half-life. The advantage is that the background events from the plastic scintillator, which cannot be neglected anymore, can be determined during this period and can be taken into account in the data analysis. Figure 5.10(b) shows an example of a single scan. The total recording time for such a spectrum was about 11 min. The x-axis represents the laser frequency as given also by the recorded Diode Laser-Ti:Sa beat frequency, but the intermediate skipped region is not indicated.

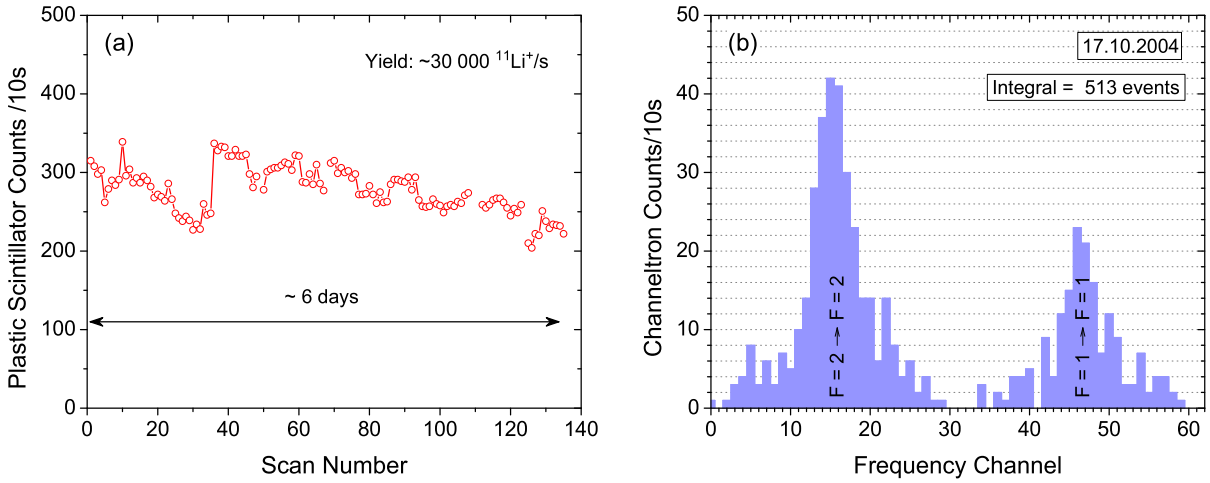

Figure 5.10. (a) Production yield of ^{11}Li during the beam time. (b) Raw data of an individual ^{11}Li scan.

5.5.4 Data Analysis for Lithium-11

For the analysis of the recorded raw data the following procedure was used. For each individual scan as shown in Fig. 5.10(b), those channels with cavity and/or ^{11}Li ion-beam dropouts were removed. The condition for such a dropout was a reduction of the laser intensity by more than 20 % compared to the previous channel (cavity dropout) or more than 30 % in the case of the plastic scintillator signal (radioactive ion-beam dropout). Normalization of the detected events, N_{raw}, was done first with respect to the ion yield according to

$$N_1^{\mathrm{Norm}} = N_{\mathrm{raw}} \times \left(\frac{N_\gamma / T_{1\,\mathrm{ref}} - N_{\mathrm{BG}} / T_{2\,\mathrm{ref}}}{\langle N_\gamma / T_{1\,\mathrm{ref}} - N_{\mathrm{BG}} / T_{2\,\mathrm{ref}} \rangle} \right)^{-1} , \tag{5.6}$$

where $N_\gamma / T_{1\,\mathrm{ref}}$ is the number of events detected per second with the plastic scintillator while the radioactive ion-beam was turned on (reference time $T_{1\,\mathrm{ref}}$). As discussed before, this count rate must be reduced by the background events N_{BG}, observed during the beam-off time $T_{2\,\mathrm{ref}}$. $\langle N_\gamma / T_{1\,\mathrm{ref}} - N_{\mathrm{BG}} / T_{2\,\mathrm{ref}} \rangle$ represents the average of the plastic scintillator events recorded over the whole spectrum.

Normalization for the Ti:Sa laser power was performed in a second step, similar as for the other lithium isotopes:

$$N_2^{\mathrm{Norm}} = N_1^{\mathrm{Norm}} \left(\frac{P_{\mathrm{Ti:Sa}}}{\langle P_{\mathrm{Ti:Sa}} \rangle} \right)^{-2} . \tag{5.7}$$

Figure 5.11(a) shows seven individual scans with the data normalized according to (5.6 - 5.7). These scans where then combined to a single resonance. To perform this addition an AC-Stark Shift correction of the frequency-axis with respect to the Ti:Sa and dye laser

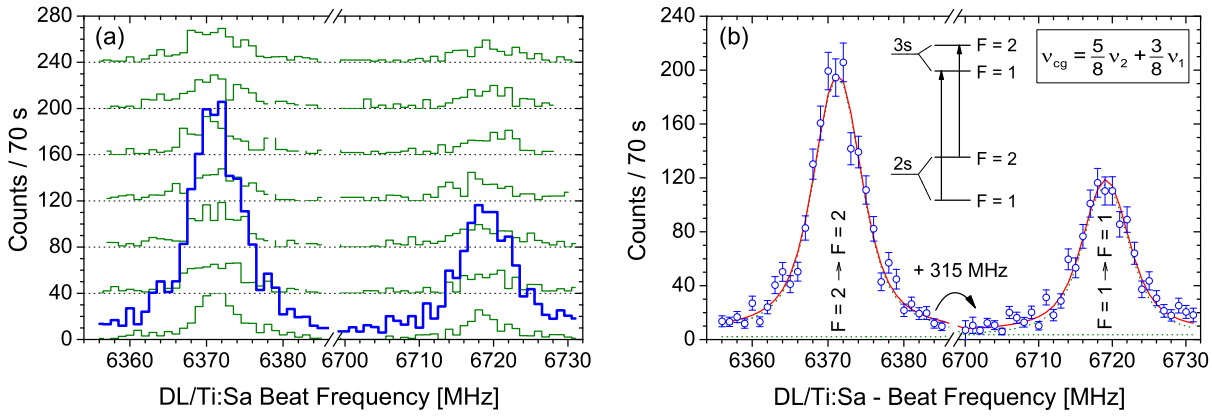

Figure 5.11. (a) Seven individual ^{11}Li scans (thin green lines) with accumulation time of 10 s/channel are summed to a single resonance (ticker blue line). The individual scans are already corrected in the count- and frequency-axis according to (5.6 - 5.7) and (5.8) respectively. (b) Fit of the resonance profile to the hyperfine structure components ($\nu_{\mathrm{Ti:Sa}} > \nu_{\mathrm{DL}}$).

power must be taken into account. The average in Ti:Sa and dye powers over all scans that were added to a single resonance were used as reference powers; they are denoted as $\langle P_{\mathrm{Ti:Sa}}\rangle_{\mathrm{all\ scans}}$ and $\langle P_{\mathrm{dye}}\rangle_{\mathrm{all\ scans}}$ respectively. The AC-Stark frequency shift in a single channel relative to these "reference powers" was calculated for the Ti:Sa and dye laser as follows,

$$\nu_{\mathrm{corr}} = \nu_{\mathrm{meas}} - (P_{\mathrm{Ti:Sa}} - \langle P_{\mathrm{Ti:Sa}}\rangle_{\mathrm{all\ scans}}) \times b_{1\,\mathrm{Ti:Sa}} - \left(P_{\mathrm{dye}} - \langle P_{\mathrm{dye}}\rangle_{\mathrm{all\ scans}}\right) \times b_{1\,\mathrm{dye}}\ , \quad (5.8)$$

where ν_{corr} and ν_{meas} denote the corrected and measured frequencies respectively. The average AC-Stark shift slope coefficient for the Ti:Sa laser was taken as $b_{1\,\mathrm{Ti:Sa}} = -0.055$ MHz/mW, while for dye laser $b_{1\,\mathrm{dye}} = 0.1$ MHz/mW was used.

When summing all individual scans to a single resonance, the average of the individual frequencies (ν_{corr}) was used as the frequency of this channel. Finally it must be considered that some scans had dropouts and therefore not each channel had the same observation time. Thus, all channels were again normalized for their real acquisition time. The result was then a single resonance profile shown in Fig. 5.11(b) with about 200 counts in the maximum. Fits could be performed with typical reduced χ^2 values around 1.7. The range of frequency values for a single channel after correction never exceeded 100 kHz and was usually much smaller. After fitting, the center-of-gravity frequency could be determined according to the formula given in Table 2.10. For the example shown in Fig. 5.11(b), $\nu_{\mathrm{cg}}(^{11}\mathrm{Li}\ ) = 6\,501.71(23)$ MHz could be obtained.

5.6 Isotope Shifts

Results of the isotope shifts measurements for the different lithium isotopes are now summarized. For ^{7,8,9}Li all isotope shifts relative to ^{6}Li are calculated from the intersection points to zero laser intensity. AC-Stark shift measurements of ^{6}Li were performed during the whole beamtime at least once per day. Each measurement of another isotope was then referenced to the ^{6}Li value that was closest in time.

5.6.1 Lithium-7

Figure 5.12 shows all sets of measurements obtained for the isotope shift between ^{6}Li and ^{7}Li ($\delta\nu^{7,6}$). In total 5 sets were obtained during the two beamtimes plus an additional set recorded also at TRIUMF in June 2004. These values are shown by the open blue circles in Fig. 5.12, uncertainties are given as 2σ errors (95 % confidence interval). The calculated weighted average of these values, represented by the full blue circle in the figure, was used as the final isotope shift value where the uncertainty is given by the 2σ standard error

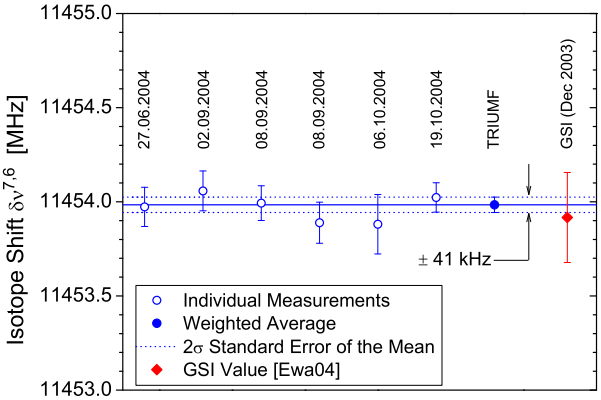

Figure 5.12. Results of ^{7}Li isotope shift measurements relative to ^{6}Li.

of the mean: $\delta\nu^{7,6} = 11\,453.984(41)$ MHz. This value shows good agreement with the previous one determined at GSI, depicted by the solid red diamond.

5.6.2 Lithium-8 and -9

The relatively high ^{8}Li and ^{9}Li ion yields that were delivered during both beam times, allowed a clearly improved measurement of the the respective isotope shift. In total, four sets of isotope shift measurements were obtained for both isotopes during the two beamtimes. The results are represented by the blue open circles in Fig. 5.13, again with an uncertainty at the 95 % confidence level (2σ). The final isotope shift values, represented by the solid blue circles $\delta\nu^{8,6} = 20\,089.765(83)$ MHz and $\delta\nu^{9,6} = 26\,787.262(69)$ MHz, are the statistically weighted average of all four measurements.

The excellent agreement for ^{8}Li is satisfying, the result for ^{9}Li from TRIUMF is slightly larger than that from GSI but still agrees within the 2σ uncertainty. The small difference can be attributed to the fact that the AC-Stark shift could not be measured at GSI. The

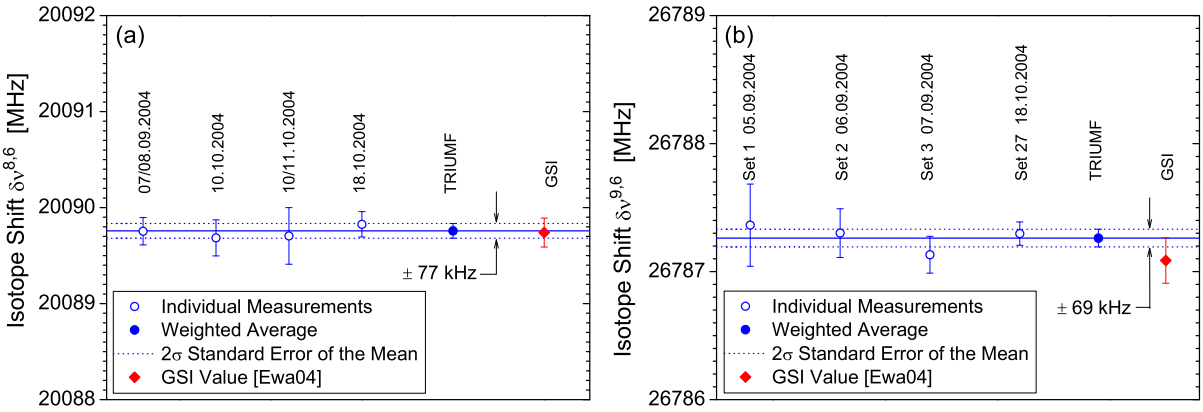

Figure 5.13. Results of isotope shift measurements for (a) ^{8}Li and (b) ^{9}Li.

etalon effect at the exit window of the chamber probably introduced a small systematic effect . The fact that a difference in the slopes of the AC-Stark effect for ^{6,7,8}Li was not observed at that time might have been a fortunate coincidence. But the size of the systematic uncertainty estimation in [Ewa05] was obviously about right.

5.6.3 Lithium-11

The ^{11}Li ion yield of about 35 000 ions/s allowed only to perform measurements at full Ti:Sa laser power. Once the center-of-gravity frequency was determined from a fit as shown in Fig. 5.11(b), the isotope shift was calculated by referencing the ^{11}Li center-of-gravity frequency to the closest-in-time measurement of the Ti:Sa AC-Stark shift line of the reference isotope ^{6}Li at the same laser power. All data obtained for ^{11}Li were combined into 24 resonances. The extracted isotope shifts, $\delta\nu^{11,6}$, are shown in Fig. 5.14 (blue open circles). The final value for the isotope shift, represented by the solid red circle, was calculated as the weighted average of these 24 resonances: $\delta\nu^{11,6} = 36\,555.210(131)$ MHz, where the standard error of the mean was used as statistical uncertainty at 2σ confidence level.

5.6.4 Systematic Uncertainties in Lithium-11 Isotope Shift Measurements

AC Stark Shift To account for systematic shifts introduced by the Ti:Sa AC-Stark shift effect, the variation of the ^{6}Li slope coefficients, $b_{1\,\mathrm{Ti:Sa}}$ during the ^{11}Li measurements was taken into account. The systematic uncertainty was estimated from the standard deviation of all slope coefficients obtained in the time window from set 45 to set 49 in Fig. 5.7 where all ^{11}Li data were recorded: $\sigma_{b_{1\,\mathrm{Ti:Sa}}} = 0.81$ kHz/mW. During this period

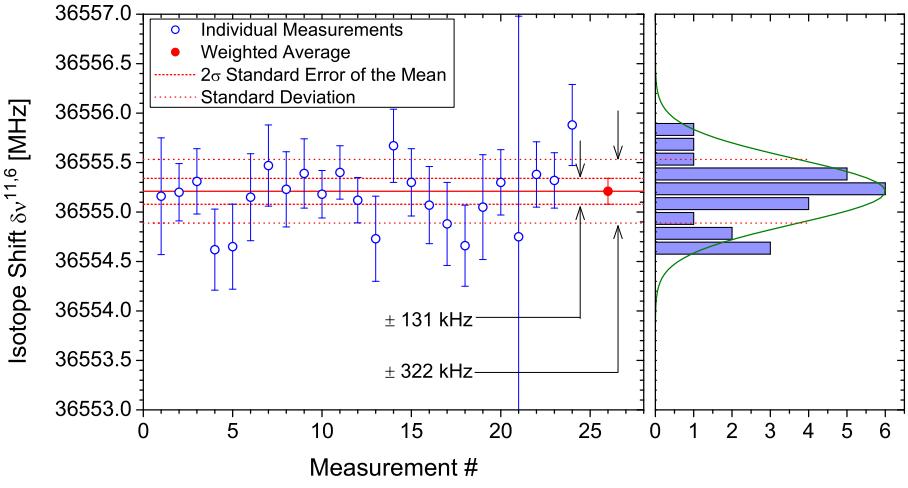

Figure 5.14. Distribution and average of ^{11}Li isotope shift results.

the average power of the Ti:Sa laser was $\langle P_{\text{Ti:Sa}}\rangle_{45\to49} = 30$ mW. Then the systematic error produced by this effect is $\Delta(\delta\nu^{11,6})_{\text{Ti:Sa}} = 2\times2\times0.81$ kHz/mW $\times 30$ mW $= 96$ kHz, where the first factor 2 represents 2σ confidence limit, and the second considers the two photons that are absorbed in the $2s \to 3s$ transition.

A similar calculation for the effect of the dye laser gives a contribution of $\Delta(\delta\nu^{11,6})_{\text{dye}} =$ 17 kHz, again calculated at the 2σ level.

Zeeman Effect in the Isotope Shift The presence of an external magnetic field at the experiment location, especially at the place where the laser ionization occurs can produce a shift in the transition frequencies and therefore it can introduce a systematic error in the isotope shift determination. The Zeeman shift has been discussed in Section 2.3.5 and here the influence on the isotope shift is estimated.

First, considering low external magnetic fields and according to the two-photon selection rules for $s \to s$ transitions ($\Delta F = 0,\ \Delta m_F = 0$), a change in the $2s \to 3s$ transition frequency is calculated for the different m_F states as follows

$$\Delta\nu_{F,m_F} = \nu_{2s,F,m_F} - \nu_{3s,F,m_F} - (\mathbb{A}_{2s} - \mathbb{A}_{3s})C_F/2\ , \tag{5.9}$$

where the term $(\mathbb{A}_{2s} - \mathbb{A}_{3s})C_F/2$ is subtracted in order to have a common origin at $B_{\text{ext}} = 0$. The behavior of ν_{2s,F,m_F} for ^{6}Li as a function of the magnetic field is already shown in Fig. 2.6(a). The $3s$ excited states show a similar behavior but to a much smaller extend. Figure 5.15(a) shows the behavior of $\Delta\nu_{F,m_F}$ obtained for ^{6}Li and ^{11}Li in the low magnetic field region. For example, the largest negative deviation comes from the $F = 3/2 \to F = 3/2$, $m_F = -1/2 \to m_F = -1/2$ transition, denoted by $\Delta\nu_{3/2,-1/2}$, while

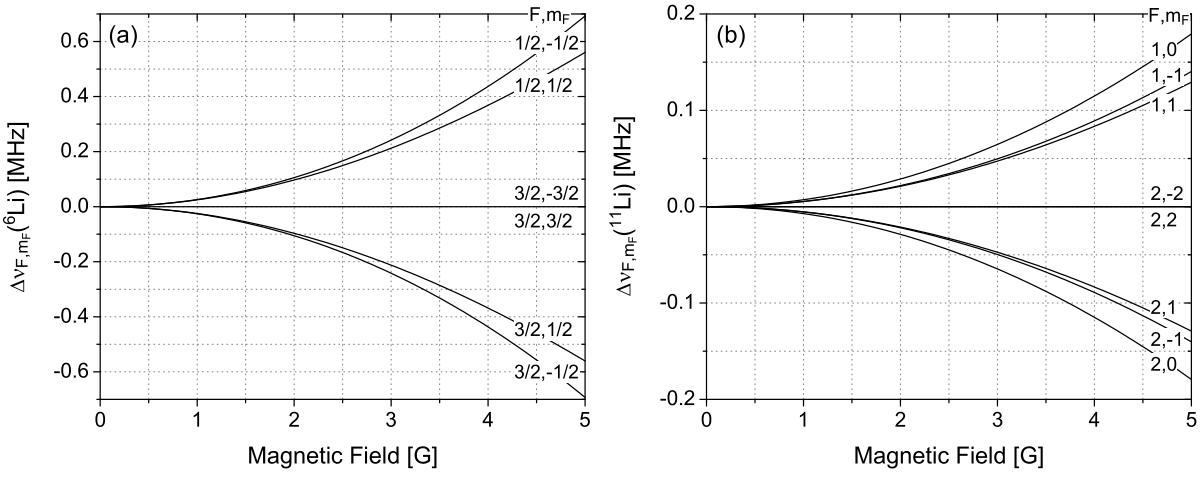

Figure 5.15. (a) Change in the 2s → 3s transition frequency for the different m_F sublevels in (a) ^{6}Li and (b) ^{11}Li as a function of the magnetic field.

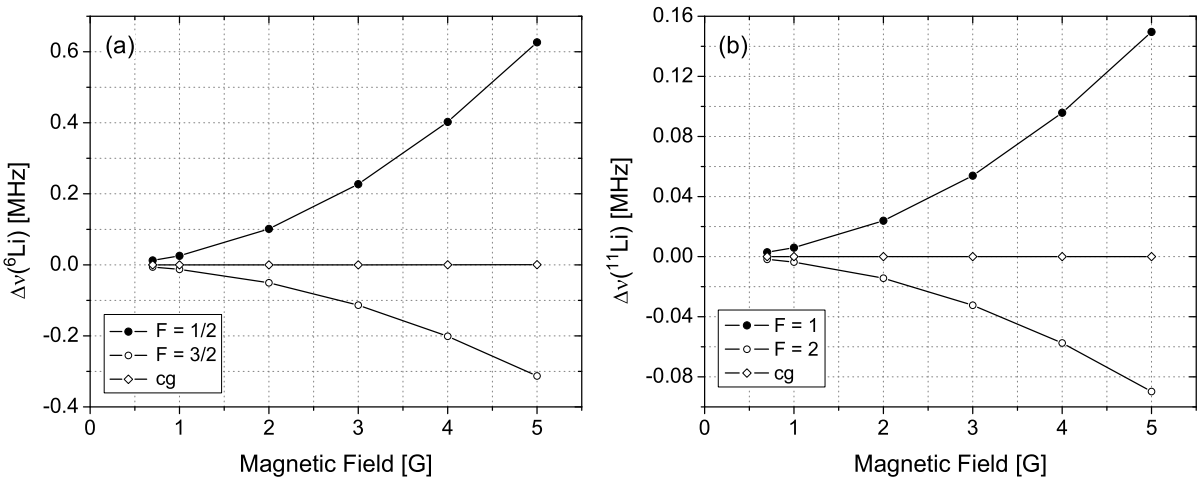

Figure 5.16. Change in the peak center position for (a) ^{6}Li and (b) ^{11}Li as a function of the magnetic field. In both cases the center-of-gravity shows only negligible dependence.

the largest positive deviation is produced by $F = 1/2 \rightarrow F = 1/2$, $m_F = -1/2 \rightarrow m_F = -1/2$, $\Delta\nu_{1/2,-1/2}$.

The magnetic field at the location of the experimental setup at ISAC was measured and was found to be 0.7 G. At this magnetic strength the split lines produced by the Zeeman effect are unresolved. Nevertheless the effect could produce a shift in the hyperfine structure center-of-gravity and therefore in the isotope shift determination. Lorentzian profiles were simulated for each $m_F \rightarrow m_F$ component at some magnetic field strengths. They were added and the resulting profile was fitted again with a Lorenztian profile from which the center could be extracted. These centers are represented by the solid and open circles in Fig. 5.16 for ^{6}Li and ^{11}Li. As can be seen, the centers show a dependence in the magnetic field but the position of the center-of-gravity frequency, represented by the open diamonds for ^{6}Li and ^{11}Li are almost independent of the magnetic field.

Thus, this effect does not introduce a significant uncertainty in the isotope shift determination, at least at magnetic field strengths of less than 5 G.

Finally by adding linearly the statistical and systematic uncertainties the isotope shift between ^{11}Li and ^{6}Li was found to be, $\delta\nu^{11,6} = 36\,555.210(244)$ MHz, where the uncertainty is given at the 95 % confidence level.

5.7 Summary of Isotope Shifts

Table 5.1 summarizes the experimentally determined isotope shifts $\delta\nu^{A,6}$ with uncertainties at 1σ confidence level. In order to calculate the root-mean-square nuclear charge radius, based on the known ^{7}Li charge radius, the values were converted to the isotope

Table 5.1. Experimental values for the isotope shift ($\delta\nu^{A,A'}$) in lithium.

Quantity	^{6}Li	^{7}Li	^{8}Li	^{9}Li	^{11}Li	Remark
$\delta\nu^{A,6}$ [MHz]	0	11 453.984(20)	20 089.765(41)	26 787.262(35)	36 555.210(122)	This work
$\delta\nu^{A,7}$ [MHz]	-11 453.984(20)	0	8 635.781(46)	15 333.279(40)	25 101.226(124)	This work
$\delta\nu^{A,7}$ [MHz]	-11 453.950(130)	0	8 635.790(150)	15 333.140(180)	-	[Ewa05]
$\delta\nu^{A,7}$ [MHz]	-11 453.983(20)	0	8 635.782(44)	15 333.272(39)	25 101.226(124)	Final

shift $\delta\nu^{A,7}$. These are shown in the second row of the table. The third row shows the isotope shifts $\delta\nu^{6,7}$, $\delta\nu^{8,7}$, and $\delta\nu^{9,7}$ as obtained previously by Ewald *et al.* [Ewa04, Ewa05], where the same method was used. These values were combined with those obtained here and the weighted average and respective weighted uncertainties are given in the fourth row of the table. The uncertainty of the isotope shift of ^{6,8,9}Li relative to ^{7}Li was reduced by factors of 3 to 6 compared to the previous measurement. The uncertainty of the isotope shift of ^{11}Li is clearly below 200 kHz and has about the same size as the uncertainty of the theoretically predicted mass shift in Table 2.9.

5.8 Nuclear Charge Radii

Root-mean-square nuclear charge radii were extracted using equation (2.31), with the experimental obtained isotope shifts $\delta\nu^{A,7}$ given in Table 5.1, and the theoretical calculated mass shift $\delta\nu^{A,7}_{\mathrm{MS}}$ given in Table 2.9. The resulting charge radii are listed in Table 5.2 and

Table 5.2. Experimental and theoretical root-mean-square nuclear charge radii in fm for the lithium isotopes. Results of this work are given with two uncertainties. The first includes the uncertainty of the ^{7}Li reference charge radius, the second one does not.

	Method	^{6}Li	^{7}Li	^{8}Li	^{9}Li	^{11}Li	Reference
Experiment	isotope shift	2.517(30){8}	2.390(30)	2.299(32){8}	2.217(35){12}	2.467(37){23}	This work
	isotope shift	2.51(3)	2.39(3)	2.30(4)	2.24(4)	-	[Ewa05]
	e^- scattering	2.55(4)	2.39(3)	-	-	-	[Jag74]
Theory	NCSM$^\square$	2.22	2.23	-	-	-	[Nav03]
	LBSM$^\diamond$	-	2.20	2.10	2.09	2.11	[Nav98]
	GFMC$^\triangle$	2.54	2.40	2.24	2.18	-	[Pie01, Pie02]
	SVMC$^\triangledown$	-	2.42	2.32	2.24	2.54	[Suz02]
	FMD$^\oplus$	2.59	2.44	2.39	2.32	-	[Nef05]
	DCM$^\circ$	2.55	2.41	-	2.42	2.67	[Tom02]

$^\square$no-Core Shell Model, $^\diamond$Large-Basis Shell Model, $^\triangle$Greens-Function Monte-Carlo, $^\triangledown$Stochastic Variational Multi-Cluster, $^\oplus$Fermionic Molecular Dynamics, $^\circ$Dynamic Correlation Model

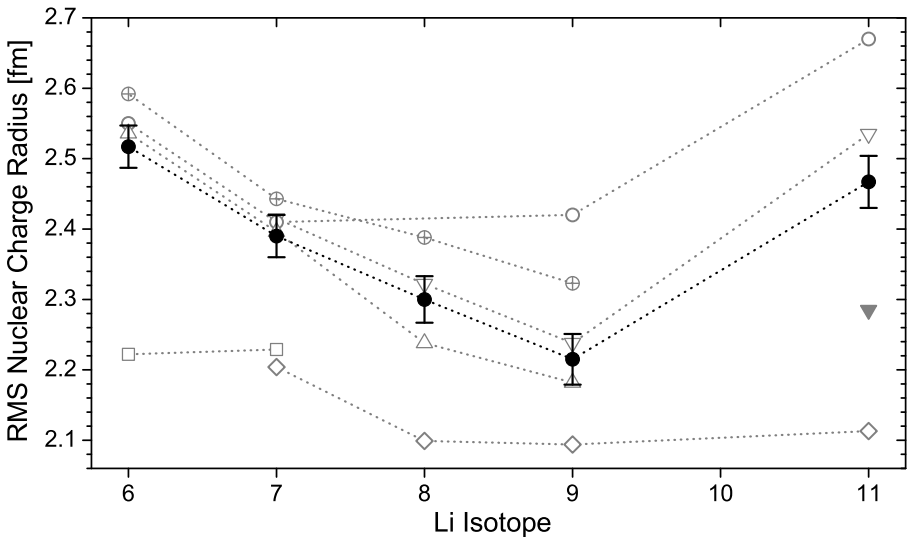

Figure 5.17. Root-mean-square nuclear charge radii of the lithium isotopes: ···●··· this work, ···□··· *ab-initio* no-Core Shell Model, ···◇··· Large-Basis Shell Model, ···△··· Greens-Function Monte-Carlo Model, ···▽··· (▼) Stochastic Variational Multi-Cluster Model, ···⊕··· Fermionic Molecular Dynamics Model, ···○··· Dynamic Correlation Model.

represented by the solid black points in Fig. 5.17. The uncertainty has been calculated using gaussian error propagation. For ^{6,8,9}Li the uncertainty is limited by the 0.03 fm uncertainty of the ^{7}Li reference radius.

Charge radii obtained for ^{6,7,8,9}Li are in excellent agreement with previous measurements using the same method or electron scattering (^{6,7}Li) but with improved precision.

The charge radii decrease continuously from ^{6}Li to ^{9}Li . This can be understood in terms of clustering of the different nuclei. ^{6}Li is known to be strongly clustered into an α-particle and a deuteron. This clusterization is also well observed in different models, like Fermionic Molecular Dynamics and Green-Functions Monte-Carlo models. This cluster-structure "melts" when more neutrons are added and therefore a more compact object results.

The most important result of this thesis is the large increase of the nuclear charge radius from ^{9}Li to ^{11}Li.

Nuclear charge radii predicted by different nuclear models are also given in Table 5.2 and are included in Fig. 5.17. The charge radii of those nuclear models that treat the protons and neutrons as point-like particles, were converted from point-proton root-mean-square radii $\bar{r}_{\mathrm{p}} = \langle {r_{\mathrm{p}}}^2 \rangle^{1/2}$ into root-mean-square nuclear charge radii $\bar{r}_{\mathrm{c}} = \langle {r_{\mathrm{c}}}^2 \rangle^{1/2}$ by folding in the proton mean-square charge radius [Sic03], $\langle {R_{\mathrm{p}}}^2 \rangle = 0.801(32)$ fm^2, and the

neutron mean-square charge radius [Kop97], $\langle {R_n}^2 \rangle = -0.117(4)$ fm^2, according to [Fri97]

$$\langle {r_c}^2 \rangle = \langle {r_p}^2 \rangle + \langle {R_p}^2 \rangle + \frac{N}{Z} \langle {R_n}^2 \rangle + \frac{3\hbar^2}{4{M_p}^2 c^2} \ . \tag{5.10}$$

The last term, $3\hbar^2/4{M_p}^2c^2 \sim 0.033$ fm^2, where M_p is the mass of the proton, is the Darwin-Foldy correction [Fri97] which takes into account the "Zitterbewegung" of the proton.

As shown, most of the models predict quite well the change in the charge radius from ^{6}Li to ^{9}Li but predictions for ^{11}Li spread over a large range. The charge radius of ^{11}Li is therefore a very good benchmark to test the nuclear models.

The No-Core Shell Model (NCSM) [Nav03] and the Large-Basis Shell Model (LBSM) [Nav98] are essentially the same models. In both cases calculations have been performed using realistic NN potentials. While earlier calculations for ^{7,8,9,11}Li treated the three-body interactions as an effective phenomenological potential [Nav98], the model has recently been revised for ^{6,7}Li to include microscopic three-body potentials [Nav03]. As can be seen in Fig. 5.17, neither the absolute charge radii, nor the trend along the isotopic chain is in agreement with the experimental results. The model predicts the ^{9}Li and ^{11}Li charge radii to be of similar size.

Greens-Function Monte Carlo Calculations are in good agreement with the experimental results. The general trend from ^{6}Li to ^{9}Li is reproduced but, as explained in Section 2.2.2, the method still fails to model the nucleus of ^{11}Li and can therefore not predict the charge radius.

Fermionic Molecular Dynamic Model [Nef05] values almost agree with the experimental results for ^{6,7,8,9}Li, but so far the model can not deliver a charge radius for ^{11}Li, because it does not get the right binding energy for this nucleus.

The Dynamic Correlation Model [Tom02] values for ^{6,7}Li agree well with the measurements but the model clearly overestimates the values for ^{9,11}Li. However, the upward trend from ^{9}Li to ^{11}Li is reproduced.

Values from the Stochastic Variational Multi-Cluster Model show the best agreement with the experimental results for all isotopes. The ^{11}Li value is almost within the experimental uncertainty. As already discussed in Section 2.2.3, calculations for ^{11}Li were performed both with and without polarization of the ^{9}Li core by the halo neutrons. By including these intrinsic excitations, a value of $\bar{r}_c(^{11}\text{Li}) = 2.52$ fm is found to be in good agreement with the experiment, while neglecting them results in a much smaller nuclear charge radius $\bar{r}_c(^{11}\text{Li}) = 2.28$ fm represented in Fig. 5.17 by the solid inverted triangle. Within this framework, neutron correlations alone cannot reproduce the large change in

the nuclear charge radius between ^{9}Li and ^{11}Li observed in the experiment. The calculations rather indicate that the ^{9}Li core is indeed perturbed by the halo neutrons and that this perturbation accounts for most of the change in the nuclear charge radius in ^{11}Li.

While these models provide a microscopic description of the nuclei, early models for ^{11}Li treated the nucleus as a three-body system, neglecting core polarization. Here, a change in the nuclear charge radius must be attributed exclusively to correlations of the two halo neutrons. For example, the center of the core is different from the center-of-mass of the system if the two neutrons spend most of their time on the same side of the core. Thus, the average charge distribution is diffused. Forssén *et al.* have constructed such model wave function of ^{11}Li to obtain an analytical model for electromagnetic dissociation of halo nuclei [For02]. There, the root-mean-square ^{11}Li nuclear matter radius of 3.55 fm was adjusted to be in good agreement with experiment [Ege02], and a distance $R_{\mathrm{C-CM}}$ between the core (C) and the center-of-mass (CM) ranging from 0.8 fm to 1.08 fm was predicted. Using the measured charge radius of ^{9}Li, the simple approximation $r_{\mathrm{c}}(^{11}\mathrm{Li}) = \sqrt{[R_{\mathrm{C-CM}}]^2 + [r_{\mathrm{c}}(^{9}\mathrm{Li})]^2} = 2.40(6)$ fm is in good agreement with the experiment. However, these calculations are inconclusive regarding structural details because there is insufficient information available on the binary neutron-^{9}Li (core) channel. Moreover, these models start with the ^{9}Li core and cannot make predictions about other nuclei in the lithium isotope chain as a consistency check.

6 Summary and Outlook

The nuclear charge radius of the halo nucleus ^{11}Li has been determined for the first time via measurements of the isotope shift in the $2s\,^2S_{1/2} \rightarrow 3s\,^2S_{1/2}$ atomic transition of lithium. This is the result of combined experimental and theoretical efforts. On the experimental side, a novel on-line laser and mass spectroscopic technique was developed at GSI Darmstadt [Ewa04, Ewa05] that is able to overcome the low abundance and short half-life of the radioactive lithium isotopes. It is based on high-resolution laser spectroscopy on an atomic beam of lithium, where the $2s\,^2S_{1/2} \rightarrow 3s\,^2S_{1/2}$ Doppler-free two-photon transition is followed by resonance ionization and ion detection with a quadrupole mass spectrometer. The technique is accurate enough to measure the isotope shift with a relative accuracy better than 10^{-5} and provides an overall detection efficiency $> 10^{-4}$.

On the theoretical side, the quantum mechanical three-electron problem has been solved to high accuracy including relativistic and quantum electrodynamic effects [Yan00, Dra05].

To measure the ^{7}Li$-^{11}$Li isotope shift, the experimental setup was moved to TRIUMF, Vancouver BC, Canada, where a ^{11}Li ion yield of $\sim$ 35 000 ions/s was produced by an ISOL technique at the ISAC facility and delivered to the experiment for about six days of experimental run. The productions for the other radioactive lithium isotopes were much higher ($> 10^8$), the $^7\mathrm{Li} - {}^{\mathrm{A}}$Li isotope shift measurements for these isotopes could be improved considerably, and the uncertainty was reduced by a factor of three to six. This was mainly reached by a careful investigation and removal of systematic effects.

The measured isotope shift between ^{7}Li and ^{11}Li is $\delta\nu^{11,7} = 25\,101.226(124)$ MHz which, combined with the theoreticaly determined mass shift of $\delta\nu^{11,7}_{\mathrm{MS}} = 25\,101.812(121)$ MHz, results in root-mean-square nuclear charge radius for ^{11}Li of $\bar{r}_{\mathrm{c}}(^{11}\mathrm{Li}) = 2.467(37)$ fm.

While the nuclear charge radii decrease continuously from ^{6}Li to ^{9}Li, a strong increase for ^{11}Li is observed. The change in the charge radius between ^{9}Li and ^{11}Li is $\sim$ 12 %.

The results have been compared with theoretical predictions of different nuclear models which are able to solve the many-body Schödinger equation for light nuclei including realistic two- and three-nucleon potentials. Best agreement is found for the Stochastic Variational Multi-Cluster model [Suz02]. Here, the increase in charge radius between ^{9}Li and ^{11}Li is a combination of halo neutron correlation and intrinsic core excitation.

The experimental setup has now been moved back again to GSI, Darmstadt. A final off-line measurement is planned to determine the absolute frequency of the $2s\,^2S_{1/2} \rightarrow 3s\,^2S_{1/2}$ two-photon transition in ^{7}Li with an accuracy of better than 10^{-11}. Improved atomic calculations of this observable are performed in parallel. The biggest challenge is here to determine the QED contribution on the order of α^4. Once this has been achieved it is possible to extract the absolute charge radius of ^{7}Li, and therefore for all lithium isotopes, without referring to an electron scattering result.

Laser spectroscopic measurements of isotope shifts in combination with accurate theoretical mass shift calculations have allowed the determination of charge radii of the lightest short-lived isotopes. With ^{6}He and ^{11}Li, two systems of two-neutron halos have been investigated. Further experiments at ANL are planned to determine the charge radius of the four-neutron halo nucleus ^{8}He, while at GSI and the University of Mainz a project has been initiated to determine the charge radius of the one-neutron halo nucleus ^{11}Be by laser spectroscopy of Be^+ ions in a Paul Trap.

A Appendix

The relationship between the basis sets $\{|F, m_F\rangle\}$ and $\{|m_I, m_J\rangle\}$ is given by the Clebsh-Gordon coefficients and leads, for example for an s-electron in ^{6}Li, to the following expressions:

$$\begin{aligned}
|F = 3/2, m_F = 3/2\rangle &= |m_I = 1, m_J = 1/2\rangle \ , \\
|F = 3/2, m_F = 1/2\rangle &= \tfrac{\sqrt{3}}{3}\,|m_I = 1, m_J = -1/2\rangle + \tfrac{\sqrt{6}}{3}\,|m_I = 0, m_J = 1/2\rangle \ , \\
|F = 3/2, m_F = -1/2\rangle &= \tfrac{\sqrt{3}}{3}\,|m_I = -1, m_J = 1/2\rangle + \tfrac{\sqrt{6}}{3}\,|m_I = 0, m_J = -1/2\rangle \ , \\
|F = 3/2, m_F = -3/2\rangle &= |m_I = -1, m_J = -1/2\rangle \ , \\
|F = 1/2, m_F = 1/2\rangle &= \tfrac{\sqrt{6}}{3}\,|m_I = 1, m_J = -1/2\rangle - \tfrac{\sqrt{3}}{3}\,|m_I = 0, m_J = 1/2\rangle \ , \\
|F = 1/2, m_F = -1/2\rangle &= -\tfrac{\sqrt{6}}{3}\,|m_I = -1, m_J = 1/2\rangle + \tfrac{\sqrt{3}}{3}\,|m_I = 0, m_J = -1/2\rangle \ .
\end{aligned} \tag{A.1}$$

Then the matrix $\mathcal{H}$ for the Hamiltonian (2.40) in the basis set $\{|F, m_F\rangle\}$ can be written as:

	$\lvert 3/2, 3/2\rangle$	$\lvert 3/2, -3/2\rangle$	$\lvert 3/2, 1/2\rangle$	$\lvert 1/2, 1/2\rangle$	$\lvert 3/2, -1/2\rangle$	$\lvert 1/2, -1/2\rangle$
$\langle 3/2, 3/2\rvert$	$\frac{\mathbb{A}}{2} + c_1$	0	0	0	0	0
$\langle 3/2, -3/2\rvert$	0	$\frac{\mathbb{A}}{2} - c_1$	0	0	0	0
$\langle 3/2, 1/2\rvert$	0	0	$\frac{\mathbb{A}}{2} + \frac{c_1}{3}$	c_2	0	0
$\langle 1/2, 1/2\rvert$	0	0	c_2	$-\mathbb{A} + c_3$	0	0
$\langle 3/2, -1/2\rvert$	0	0	0	0	$\frac{\mathbb{A}}{2} - \frac{c_1}{3}$	c_2
$\langle 1/2, -1/2\rvert$	0	0	0	0	c_2	$-\mathbb{A} - c_3$

(A.2)

With, $c_1 = \left(\frac{1}{2} g_J \mu_\mathrm{B} + g_I \mu_\mathrm{N}\right) B_\mathrm{ext}$, $c_2 = \frac{\sqrt{2}}{3}\left(-g_J \mu_\mathrm{B} + g_I \mu_\mathrm{N}\right) B_\mathrm{ext}$, and $c_3 = \frac{1}{3}\left(-\frac{1}{2} g_J \mu_\mathrm{B} + 2 g_I \mu_\mathrm{N}\right) B_\mathrm{ext}$. The energy eigenvalues of (A.2) can be found by solving the Schrödinger equation,

$$\mathcal{H}|\psi\rangle = E|\psi\rangle, \tag{A.3}$$

which can be expressed as

$$\left(\mathcal{H} - E\mathcal{I}\right)|\psi\rangle = \mathbf{0}, \tag{A.4}$$

where $\mathcal{I}$ is the identity matrix. Then, assuming that the eigenstates $|\psi\rangle \neq 0$, (A.4) can be satisfied if the matrix $(\mathcal{H} - E\mathcal{I})$ is singular, which implies that its determinant is zero.

$$\begin{vmatrix} \frac{\mathbb{A}}{2} + c_1 - E & 0 & 0 & 0 & 0 & 0 \\ 0 & \frac{\mathbb{A}}{2} - c_1 - E & 0 & 0 & 0 & 0 \\ 0 & 0 & \frac{\mathbb{A}}{2} + \frac{c_1}{3} - E & c_2 & 0 & 0 \\ 0 & 0 & c_2 & -\mathbb{A} + c_3 - E & 0 & 0 \\ 0 & 0 & 0 & 0 & \frac{\mathbb{A}}{2} - \frac{c_1}{3} - E & c_2 \\ 0 & 0 & 0 & 0 & c_2 & -\mathbb{A} - c_3 - E \end{vmatrix} = 0. \quad \text{(A.5)}$$

The energy eigenvalues are obtained by solving:

$$\frac{\mathbb{A}}{2} + c_1 - E = 0 \ , \quad \text{(A.6)}$$

$$\frac{\mathbb{A}}{2} - c_1 - E = 0 \ , \quad \text{(A.7)}$$

$$\left(\frac{\mathbb{A}}{2} + \frac{c_1}{3} - E\right)(-\mathbb{A} + c_3 - E) - {c_2}^2 = 0 \ , \quad \text{(A.8)}$$

$$\left(\frac{\mathbb{A}}{2} - \frac{c_1}{3} - E\right)(-\mathbb{A} - c_3 - E) - {c_2}^2 = 0 \ . \quad \text{(A.9)}$$

The solutions, with $g_F = g_J - g_I(\mu_{\rm N}/\mu_{\rm B})$, are

$$E_1 = \frac{\mathbb{A}}{2} + \left(\frac{g_J\mu_{\rm B}}{2} - g_I\mu_{\rm N}\right)B_{\rm ext} \ , \quad \text{(A.10)}$$

$$E_2 = -\frac{\mathbb{A}}{4} + \frac{g_I\mu_{\rm N}B_{\rm ext}}{2} + \frac{1}{2}\sqrt{\left(\frac{3\mathbb{A}}{2} + \frac{g_F\mu_{\rm B}B_{\rm ext}}{3}\right)^2 + \frac{8}{9}\left(g_F\mu_{\rm B}B_{\rm ext}\right)^2} \ , \quad \text{(A.11)}$$

$$E_3 = -\frac{\mathbb{A}}{4} - \frac{g_I\mu_{\rm N}B_{\rm ext}}{2} + \frac{1}{2}\sqrt{\left(\frac{3\mathbb{A}}{2} - \frac{g_F\mu_{\rm B}B_{\rm ext}}{3}\right)^2 + \frac{8}{9}\left(g_F\mu_{\rm B}B_{\rm ext}\right)^2} \ , \quad \text{(A.12)}$$

$$E_4 = \frac{\mathbb{A}}{2} - \left(\frac{g_J\mu_{\rm B}}{2} - g_I\mu_{\rm N}\right)B_{\rm ext} \ , \quad \text{(A.13)}$$

$$E_5 = -\frac{\mathbb{A}}{4} + \frac{g_I\mu_{\rm N}B_{\rm ext}}{2} - \frac{1}{2}\sqrt{\left(\frac{3\mathbb{A}}{2} + \frac{g_F\mu_{\rm B}B_{\rm ext}}{3}\right)^2 + \frac{8}{9}\left(g_F\mu_{\rm B}B_{\rm ext}\right)^2} \ , \quad \text{(A.14)}$$

$$E_6 = -\frac{\mathbb{A}}{4} - \frac{g_I\mu_{\rm N}B_{\rm ext}}{2} - \frac{1}{2}\sqrt{\left(\frac{3\mathbb{A}}{2} - \frac{g_F\mu_{\rm B}B_{\rm ext}}{3}\right)^2 + \frac{8}{9}\left(g_F\mu_{\rm B}B_{\rm ext}\right)^2} \ . \quad \text{(A.15)}$$

Bibliography

[Arn87] E. Arnold, J. Bonn, R. Gegenwart, W. Neu, R. Neugart, E. W. Otten, G. Ulm, K. Wendt, and ISOLDE Collaboration: *Nuclear Spin and Magnetic Moment of ^{11}Li*, Physics Letters B, **197**, 311-314, (1987).

[Arn94] E. Arnold, J. Bonn, A. Klein, P. Lievens, R. Neugart, M. Neuroth, E. W. Otten, H. Reich, and W. Widdra: *The quadrupole moment of the neutron-halo nucleus ^{11}Li*, Zeitschrift für Physik A, **349**, 337-338, (1994).

[Aud97] G. Audi, O. Bersillon, J. Blachot, and A. H. Wapstra: *The NUBASE evaluation of nuclear and decay properties*, Nuclear Physics A, **624**, 1-124, (1997).

[Aud03] G. Audi, A. H. Wapstra, and C. Thibault: *The AME2003 Atomic Mass Evaluation (II). Tables, graphs and references*, Nuclear Physics A, **729**, 337-676 (2003).

[Bac05] C. Bachelet, G. Audi, C. Gaulard, C. Guénaut, F. Herfurth, D. Lunney, M. De Saint Simon, and C. Thibault: *Mass measurement of short-lived halo nuclides*, European Physical Journal A, **Online First**, http://dx.doi.org/10.1140/epjad/i2005-06-005-5, (2005).

[Bec74] A. Beckmann, K. D. Böklen, and D. Elke: *Precision measurements of the nuclear magnetic dipole moments of ^{6}Li, ^{7}Li, ^{23}Na, ^{41}K*, Zeitschrift für Physik, **270**, 173-186, (1974).

[Bla92] B. Blank, J.-J. Gaimard, H. Geissel, K.-H. Schmidt, K. Stelzer, K. Sümmerer, D. Bazin, R. Del Moral, J. P. Dufour, A. Fleury, F. Hubert, H.-G. Clerc, and M. Steiner: *Charge-changing cross sections of the neutron-rich isotopes 8,9,11Li*, Zeitschrift fr Physik A, **343**, 375-379, (1992).

[Bla98] K. Blaum, C. Geppert, P. Müller, W. Nörtershäuser, E. W. Otten, A. Schmitt, N. Trautmann, K. Wendt, and B. A. Bushaw: *Properties and performance of a quadrupole mass filter used for resonance ionization mass spectrometry*, International Journal of Mass Spectrometry, **181**, 67-87, (1998).

[Bla00] K. Blaum, C. Geppert, P. Müller, W. Nörtershäuser, K. Wendt, and B. A. Bushaw: *Peak shape for a quadrupole mass spectrometer: comparison of com-*

puter simulation and experiment, International Journal of Mass Spectrometry, **202**, 81-89, (2000).

[Bon84] K. D. Bonin, and T. J. McIlrath: *Two-photon electric-dipole selection rules*, Journal of the Optical Sociaty of America A, **1**, 52-55, (1984).

[Bri99] P. Bricault, P.W. Schmor, G. Stanford, C. Mark, M. Dombsky, M. Gallop, L. Moritz, and L. Udy: *Proc. 15th International Conference on Cyclotrons and their Applications 1998, Caen, France*, Inst. of Physics Publishing, 347 (1999).

[Bus87] B. A. Bushaw, B. D. Cannon, G. K. Gerke, and T. J. Whitaker: *High Efficiency, High Abundance Sensitivity RIMS by Double-Resonance Excitation with cw Lasers*, Editors: G.S. Hurst, C. Grey Morgan, Proceedings of the 3rd. International Symposium RIS Inst. Phys. Conf. Ser., Vol. 84, 103-108, (1987).

[Bus00] B. A. Bushaw, and W. Nörtershäuser: *Resonance ionization spectroscopy of stable strontium isotopes and 90Sr via 5s2 1S0 - 5s5p 1P1 - 5s5d 1D2 - 5s11f 1F3 - Sr+*, European Physical Journal D, **55**, 1679-1692, (2000).

[Car98] J. Carlson, and R. Schiavilla: *Structure and Dynamics of Few-Nucleon Systems*, Rev. Mod. Phys. **70**, 743-481 (1998).

[Coo01] S.A. Coon, and H.K. Han: *Reworking the Tucson-Melbourne three-nucleon potential*, Few Body Systems **30**, 131-141 (2001).

[Dem88] W. Demtröder: *Laser Spectroscopy*, Springer-Verlag, Berlin (1988).

[Dom00] M. Dombsky, D. Bishop, P. Bricault, D. Dale, A. Hurst, K. Jayamanna, R. Keitel, M. Olivo, P. Schmor, and G. Stanford: *Commissioning and initial operation of a radioactive beam ion source at ISAC*, *Review of Scientific Instruments* **71**, 978-980 (2000).

[Dra05] G. W. F. Drake, W. Nörtershäuser, and Z.-C. Yan: *Isotopes Shifts and Nuclear Radius Measurements for Helium and Lithium*, Canadian Journal of Physics **82**, 835-845 (2004).

[Dre83] R. W. P. Drever, J. L. Hall, F. V. Kowalski, J. Hough, G. M. Ford, A. J. Munley, and H. Ward: *Laser Phase and Frequency Stabilisation Using an Optical Resonator*, Applied Physics B, **31**, 97-105, (1983).

[Ege02] P. Egelhof, G. D. Alkhazov, M. N. Andronenko, A. Bauchet, A. V. Dobrovolsky, S. Fritz, G. E. Gavrilov, H. Geissel, C. Gross, A. V. Khanzadeev, G. A. Korolev, G. Kraus, A. A. Lobodenko, G. Münzenberg, M. Mutterer, S. R. Neumaier, T. Schäfer, C. Scheidenberger, D. M. Seliverstov, N. A. Timofeev, A. A. Vorobyov, and V. I. Yatsoura: *Nuclear-matter distributions of halo nuclei from elastic proton scattering in inverse kinematics*, European Physical Journal A, **15**, 27-33, (2002).

[Ewa04] G. Ewald, W. Nörtershäuser, A. Dax, S. Götte, R. Kirchner, H.-J. Kluge, T. Kühl, R. Sánchez, A. Wojtaszek, B. A. Bushaw, G. W. F. Drake, Z.-C. Yan, and C. Zimmermann: *Nuclear Charge Radii of ^{8,9}Li Determined by Laser Spectroscopy*, Physical Review Letters, **93**, 113002, (2004).

[Ewa05] G. Ewald: *Messung der Ladungsradien der radioaktiven Lithium-Isotope ^{8}Li und ^{9}Li*, Dissertation zur Erlangung der Doktorwürde, Naturwissenschaftlich-Mathematischen Gesamtfakultät, Ruprecht-Karls-Universität Heidelberg, (2005).

[Fri97] J. L. Friar, J. Martorell, and D. W. L. Sprung: *Nuclear sizes and the isotope shift*, Physical Review A, **56**, 4579-4586, (1997).

[For02] C. Forssén, V. D. Efros, and M. V. Zhukov: *Analytical E1 strength functions of two-neutron halo nuclei: ^{11}Li and ^{14}Be*, Nuclear Physics A, **706**, 48-60, (2002).

[Gei02] R. W. Geithner: *Nuclear Moments and Differences in Mean-Square Charge-Radii of Short-Lived Neon Isotopes by Collinear Laser Spectroscopy*, PhD Thesis, Johannes Gutenberg-Universität, Mainz, (2002).

[Han87] P. G. Hansen, and B. Jonson: *The Neutron Halo of Extremely Neutron-Rich Nuclei*, Europhysics Letters, **4**, 409-414, (1987).

[Hec87] E. Hecht: *Optics*, Addison-Wesley Publishing Company, (1987).

[Jag74] C. W. de Jager, H. de Vries and C. de Vries: *Nuclear Charge- and Magnetization-Density Distribution Parameters from Elastic Electron Scattering*, Atomic Data and Nuclear Data Tables, **14**, 479-508, (1974).

[Kob88] T. Kobayashi, O. Yamakawa, K. Omata, K. Sugimoto, T. Shimoda, N. Takahashi, and I. Tanihata: *Proyectil fragmentation of the extremely neutron-rich nucleus ^{11}Li at 0.79 GeV/nucleon*, Physical Review Letters **60**, 2599-2602 (1988).

[Kop97] S. Kopecky, J. A. Harvey, N. W. Hill, M. Krenn, M. Pernicka, P. Riehs, and S. Steiner: *Neutron charge radius determined from the energy dependence of the neutron transmission of liquid ^{208}Pb and ^{209}Bi*, Physical Review C, **56**, 2229-2237, (1997).

[Lin04] M. Lindroos: *Review of Isol-Type Radioactive Beam Facilities*, Proceedings of EPAC, Lucerne, Switzerland, 45-49, (2004).

[Mac96] R. Machleidt, F. Sammarruca, and Y. Song: *Nonlocal nature of the nuclear force and its impact on nuclear structure*, Physical Review C **53**, 1483-1487 (1996).

[May85] T. Mayer-Kuckuk: *Atomphysik*, B.G. Teubner Verlag, Stuttgart (1977).

[Nav98] P. Navrátil, and B. R. Barrett: *Large-basis shell-model calculations for p-shell nuclei*, Physical Review C, **57**, 3119-3128, (1998).

[Nav03] P. Navrátil, and W. E. Ormand: *Ab initio shell model with a genuine three-nucleon force for the p-shell nuclei*, Physical Review C, **68**, 034305, (2003).

[Nef05] T. Neff, H. Feldmeier, and R. Roth: *From the NN interaction to nuclear structure and reactions*, Proc. 21st Winter Workshop on Nuclear Dynamics, (2005).

[Neu73] R. Neugart: *Spin Exchange Polarization and Measurement of the Hyperfine Splitting of Short-Lived ^{8}Li*, Zeitschrift fr Physik, **261**, 237-248, (1973).

[Noe03] W. Nörtershäuser, A. Dax, G. Ewald, I. Katayama, R. Kirchner, H.-J. Kluge, T. Kühl, R. Sanchez, I. Tanihata, M. Tomaselli, H. Wang, and C. Zimmermann: *A setup for high-resolution isotope shift measurements on unstable lithium isotopes*, Nuclear Instruments and Methods in Physics Research B, **204**, 644-648, (2003).

[Ott87] W. E. Otten: *Nuclear Radii and Moments of Unstable Isotopes*, Treatise of Heavy-Ion Physics, Vol. 8, Plenum Press, New York, (1987).

[Pac96] K. Pachucki, D. Leibfried, M. Weitz, A. Huber, W. König, and T. W. Hänsch: *Theory of the energy levels and precise two-photon spectroscopy of atomic hydrogen and deuterium*, Journal of Physics B, **29**, 177-196, (1996).

[Pau53] W. Paul, and H. Steinwedel: *Ein neues Massenspektrometer ohne Magnetfeld*, Z. Naturforschung, **8a**, 448-451 (1953).

[Pie01] S. C. Pieper, V. R. Pandharipande, R. B. Wiringa, and J. Carlson: *Realistic Models of Pion- Exchange Three-Nucleon Interactions*, Physical Review C **64**, 014001 (2001).

[Pie02] S. C. Pieper, K. Varga, and R. B. Wiringa: *Quantum Monte Carlo calculations of A = 9,10 nuclei*, Physical Review C, **66**, 044310, (2002).

[Pie05] S. C. Pieper: *Personal communication.*

[Pos66] A. M. Poskanzer, S. W. Cosper, and E. K. Hyde: *New isotopes: ^{11}Li, ^{14}B and ^{15}B*, Physical Review Letters **17**, 1271-1274, (1966).

[Pud95] B. S. Pudliner, V. R. Pandharipande, J. Carlson, and R. B. Wiringa: *Quantum Monte Carlo Calculations of A $\leq$ 6 Nuclei*, Physical Review Letters **74**, 43964399 (1995).

[Rad95] L. J. Radziemski, R. E. Jr., and J. W. Brault: *Fourier-transform-spectroscopy measurements in the spectra of neutral lithium, ^6Li I and ^7Li I (LI I)*, Physical Review A, **52**, 4462-4470, (1995).

[Rag89] P. Raghavan: *Table of Nuclear Moments*, Atomic Data and Nuclear Data Tables, **42**, 189-291, (1989).

[Rus03] P. Russel: *Photonic Crystal Fibers*, Science, **299**, 358-362, (2003).

[Sch00] F. Schmitt, A. Dax, R. Kirchner, H.-J. Kluge, T. Kühl, I. Tanihata, M. Wakasugi, H. Wang, and C. Zimmermann: *Towards the determination of the charge radius of ^{11}Li by laser spectroscopy*, Hyperfine Interactions, **127**, 111-115, (2000).

[Sic03] I. Sick: *On the rms-radius of the proton*, Physics Letters B, **576**, 62-67, (2003).

[Sob72] I. I. Sobelman: *Introduction to the Theory of Atomic Spectra*, Pergamon Press, Oxford (1972)

[Sto94] V. G. J. Stoks, R. A. M. Klomp, C. P. F. Terheggen, and J. J. de Swart: *Construction of High-Quality NN Potential Models*, Physical Review **C** 49, 29502962 (1994).

[Sto05] N. J. Stone: *Table of nuclear magnetic dipole and electric quadrupole moments*, Atomic Data and Nuclear Data Tables, **90**, 75-176, (2005).

[Sun84] D. Sundholm, P. Pyykko, L. Laaksonen, and A. J. Sadlej: *Nuclear quadrupole moment of lithium from combined fully numerical and discrete basis-set calculations on LiH*, Chemical Physics Letters, **112**, 1-9, (1984).

[Sue67] L. R. Suelzle, M. R. Yearian, and H. Crannell: *Elastic Electron Scattering from ^{6}Li and ^{7}Li*, Physical Review, **132**, 9921004, (1967).

[Suz02] Y. Suzuki, R. G. Lovas, and K. Varga: *Study of light exotic nuclei with a Stochastic variational method - Application to lithium isotopes*, Progress of Theoretical Physics Supplement, **146**, 413-421, (2002).

[Tan85] I. Tanihata, H. Hamagaki, O. Hashimoto, Y. Shida, N. Yoshikawa, K. Sugimoto, O. Yamakawa, T. Kobayashi, and N. Takahashi: *Measurements of interaction cross sections and nuclear radii in the light p-shell region*, Physical Review Letters, **55**, 2676-2679, (1985).

[Tan88] I. Tanihata, T. Kobayashi, O. Yamakawa, S. Shimoura, K. Ekuni, K. Sugimoto, N. Takahashi, T. Shimoda, and H. Sato: *Measurements of interaction cross sections using isotope beams of Be and B and isospin dependence of the nuclear radii*, Physics Letters B, **206**, 592-596, (1988).

[Tan96] I. Tanihata: *Nuclear Structure Studies from Reaction Induced by Radioactive Nuclear Beams*, Progress in Particle and Nuclear Physics, **35**, 505-573, (1995).

[Tom02] M. Tomaselli, T. Kühl, W. Nörtershäuser, G. Ewald, R. Sanchez, S. Fritzsche, and S. G. Karshenboim: *Systematic model calculations of the hyperfine structure in light and heavy ions*, Canadian Journal of Physics, **80**, 1347-1354, (2002).

[Thi75] C. Thibault, R. Klapisch, C. Rigaud, A. M. Poskanzer, R. Prieels, L. Lessard, and W. Reisdorf: *Direct Measurements of the Masses of ^{11}Li and $^{26\text{-}32}Na$ with an On-Line Mass Spectrometer*, **12**, 644-657, (1975).

[Var95] K. Varga, and Y. Suzuki: *Precise solution of few-body problems with the stochastic variational method on a correlated Gaussian basis*, Physical Review C, **52**, 2885-2905, (1995).

[Voe91] H.-G. Voelk, and D. Fick: *The electric moments of ^{7}Li from coulomb scattering*, Nuclear Physics A, **530**, 475-489, (1991).

[Wan04] L.-B. Wang, P. Mueller, K. Bailey, G. W. F. Drake, J. P. Greene, D. Henderson, R. J. Holt, R. V. F. Janssens, C. L. Jiang, Z.-T. Lu, T. P. O'Connor, R. C. Pardo, K. E. Rehm, J. P. Schiffer, and X. D. Tang: *Laser Spectroscopic Determination of the ^6He Nuclear Charge Radius*, Physical Review Letters, **93**, 142501, (2004).

[Wen99] K. Wendt, K. Blaum, B. A. Bushaw, C. Grüning, R. Horn, G. Huber, J. V. Kratz, P. Kunz, P. Müller, W. Nörtershäuser, M. Nunnemann, G. Passler, A. Schmitt, N. Trautmann, and A. Waldek: *Recent developments in and applications of resonance ionization mass spectrometry*, Fresenius Journal of Analytical Chemistry, **364**, 471-477, (1999).

[Wha64] L. Wharton, L. P. Gold, and W. Klemperer: *Quadrupole moment of ^6Li*, Physical Review, **133**, B270-B272, (1964).

[Wir95] R. B. Wiringa, V. G. J. Stoks, and R. Schiavilla: *Accurate nucleon-nucleon potential with charge-independence breaking*, Physical Review C, **51**, 38-51, (1995).

[Wou88] J. M. Wouters, R. H. Kraus, Jr., D. J. Vieira, G. W. Butler, and K. E. G. Löbner: *Direct Mass Measurements of the Neutron-Rich Light Isotopes of Lithium Through Fluorine*, Zeitschrift fr Physik A, **331**, 229-233, (1988).

[Yan00] Z.-C. Yan, and G. W. F. Drake: *Lithium isotope shifts as a measure of nuclear size*, Physical Review A, **61**, 022504, (2000).

[Yan03] Z.-C. Yan and G. W. F. Drake: *Bethe Logarithm and QED Shift for Lithium*, Physical Review Letters, **91**, 113004, (2003).

[You93] B. M. Young, W. Benenson, M. Fauerbach, J. H. Kelley, R. Pfaff, M. Steiner, J. S. Winfield, T. Kubo, M. Hellström, N. A. Orr, J. Stetson, J. A. Winger, and S. J. Yennello: *Mass of ^{11}Li from the $^{14}C(^{11}B,^{11}Li)^{14}O$ Reaction*, Physical Review Letters, **71**, 4124-4126, (1993).